Doctoral Dissertation

DYNAMICS OF LARGE-SCALE INTERNAL WAVES IN SHIOZU BAY, LAKE BIWA

September 2013

Graduate School of Marine Science and Technology
Tokyo University of Marine Science and Technology
Doctoral Course of Applied Marine Environmental Studies

Guillaume Alain Robert AUGER

Doctoral Dissertation

DYNAMICS OF LARGE-SCALE INTERNAL WAVES IN SHIOZU BAY, LAKE BIWA

September 2013

Graduate School of Marine Science and Technology
Tokyo University of Marine Science and Technology
Doctoral Course of Applied Marine Environmental Studies

Guillaume Alain Robert AUGER

Abstract

Internal waves in Lake Biwa are ubiquitous features generated during summer time, when the surface temperature is much higher than the internal temperature. This layer with a high temperature gradient makes the metalimnion (or thermocline); which acts as a waveguide for the internal waves. These internal waves are generated by periodic or sudden wind forcing (breezes or typhoons, for instance) and redistribute the stored energy in the lake to turbulence at various scales, influencing the mixing intensity and the distribution of pollutant or nutrients (Saggio & Imberger, 1998). So far the consensus is the downward cascade of energy from large scale to turbulence: low frequency to high frequency internal waves then breaking. However a recent study suggests that the energy redistribution is more complex than previously thought and can occur directly from low frequency to turbulence. Because of this result and the impact on mixing and ultimately on nutrient distribution, the linkage between large-scale internal waves and turbulence intensity needs more study.

This thesis first deals with observation data in Lake Biwa, Shiga Prefecture, more precisely at the mouth of Shiozu Bay. The first objective was reached through a microstructure profiler (TurboMAP) operation carried out over the span of 48 hours inside the bay, and by using ADCPs (Acoustic Doppler Current Profiler), which measured the flow speed and direction at the mouth of the bay for 7 days. The current data where then analyzed in the frequency space and a modal analysis was performed on the TurboMAP data; upon analysis the results showed the presence of a two Kelvin waves, one with a period of 45 hours being a vertical mode 1 and horizontal mode 1, and the other wave being a vertical mode 1 and horizontal mode 2 with a period of approximately 23 hours. In

addition, current associated to the internal V1H1 Kelvin wave shows the wave entering the bay, but does not exhibit clues of being reflected back.

After confirming the presence of low-frequency internal waves within the bay, the first part of my research highlighted the presence of enhanced turbulence and mixing offshore below the metalimnion (ε: 10^{-7} W kg^{-1}), which was previously thought to be turbulence-free (10^{-10} W kg^{-1}). Furthermore the enhanced mixing event was linked to the low frequency waves induced current being in phase, inducing velocity shear but not strong enough to bring down the Richardson number below the shear instability threshold of one fourth. Contraction and separation of isotherm within the hypolimnion may be a link to the cause. Moreover such currents synchronization provoked sediment resuspension up to 10 meters above the bottom in enhancing bottom stress. In this section, my research shows evidence of direct energy redistribution from low frequency internal wave field to turbulence.

The second objective of this thesis is the study of low-frequency internal wave dynamic within Shiozu Bay. For this purpose the numerical simulator SUNTANS was used. SUNTANS (Stanford Unstructured Non- hydrostatic Terrain Following Adaptive Navier-stockes Simulator) is developed by Fringer *et al.* (2006). The main features of this numerical simulator are the triangle-shaped cells (unstructured) and the non-hydrostatic component of the pressure field that is already implemented.

To generate the initial conditions a nesting method was applied. To start, a simulation was run with a coarse resolution grid from winter time to summer time. Based on five meteorological stations scattered around Lake Biwa, boundary conditions (wind forcing and heat fluxes) were implemented to generate the temperature and wind field until a specific typhoon period. Then in using data from the coarse resolution to a finer grid, for a simulation starting at the end of July 2001, simulated data were compared against observed data to assess the consistency of simulated data. The simulation reproduced the observed low-frequency

internal wave field with similar frequencies.

Based on the analysis of potential energy and dissipated energy time series, this research shows that the low-frequency internal waves that enters Shiozu Bay does not either completely dissipate or break. Moreover isotherm elevation associated to the internal V1H1 Kelvin wave frequency highlights the cyclonic rotation pattern, which is characteristic of the Kelvin wave, within the bay. This result shows that the part of the Kelvin wave entering the bay goes in and out.

Moreover the dynamic of the internal wave field within the bay displays an interesting dynamic at the narrowing of the bay. Because of the contraction below the metalimnion the flow was virtually controlled, locally speeding up the flow and generating isotherms deepening. These two processes generated turbulence by shear and shear, according to the Mellor-Yamada 2.5 turbulence model ε reached 10^{-6} W kg^{-1}. Additionally the occurrence of these enhanced turbulent events appears to depend on the amount of energy detained by the low frequency internal wave field and to occur downstream the contraction of the hypolimnetic flow.

Thanks to the combination of numerical simulation and observed data, this research exhibits the processes involved in the enhanced shear inside Shiozu Bay, as well as the enhanced turbulence, and the need of the strong diel wind. Intense turbulent events occurred at the bay contraction when the flow appeared to be virtually controlled by the topography. Such control of the fluid would deepen isotherm and accelerate the flow downstream the contraction.

The findings of this research emphasize the direct role of the low frequency internal wave field in energy redistribution, and explain features that were observed during the campaign (isotherms behavior within the hypolimnion), and give a scenario. Moreover, this thesis shows that the interaction of the low frequency internal wave field with bay constriction below the metalimnion may play a role in vertical fluxes from bottom to interface.

A man cannot dispel his fear about the most important matters if he does not know what is the nature of the universe but suspects the truth of some mythical story. So that without natural science it is not possible to attain our pleasures unalloyed.

Epicurus (341-270 BCE)

Acknowledgements

I would like to thank and express my sincerest gratitude to my advisor Prof Hidekatsu Yamazaki who guided me throughout my PhD, and provided invaluable support.

I want to aknowledge Prof Takeyoshi Nagai, Prof Michio Kumagai and Dr Chunmeng Jiao for their constructive comments on my first publication.

I am grateful to Hikaru Honma, Eiji Masunaga, Herminio Neto and the other members of the Ocean Ecosystem Dynamics Laboratory for their supports and constructive discussions.

The personal effort of Jeremy Bricker, Rusty Holleman and Edward Gross in explaning how to use SUNTANS is highly appreciated.

Also I am very greatful toward Lynn Allmon for editing the english of this thesis, as well as Prof Yujiro Kitade, Prof Hisayuki Arakawa and Prof Jiro Yoshida for their comments on the early version of the manuscript.

I want to thank to Mathias Girault, Hiro Iimura for their friendship.

A very special thank to Yumi Chou for her love, support, cooperation and enormous patience even during very hard times.

Finaly I want to thank my parents and my brother for their efforts to encourage me even though they are thousands of kilometers away.

This work was financially supported by the Ministry of Education, Culture, Sports, Science and Technology of Japan

Contents

List of Figures

Chapter 1

Introduction

1.1 Motivation

Lakes are inland water bodies that play a significant role in the global carbon budget and that release climatically-active gases to the atmosphere (Cole *et al.*, 2007). Such enclosed medium are sensitive to meteorological forces such as heat fluxes and wind stress, so it is necessary to understand the effects they have on lakes' dynamics and ecosystems. Heat fluxes modify the temperature distribution over time and generate the stratification of the water the during summer in temperate areas. Water columns are said to be stratified when the surface temperature differs greatly from the internal water temperature. Heat fluxes may generate motion in the water if there is a horizontal gradient of temperature (Monismith *et al.*, 1990; Okely & Imberger, 2007). However, wind forcing represents the major source of energy and momentum in lakes and affects lakes at various scales. But the understanding of the involved processes and their impact remains incomplete. Moreover, in a context of global warming and climate change, studies addressed the occurence of tropical cyclones. For example, Knutson *et al.* (2010) suggests that strong typhoons will occur more frequently because of climate change. This statement strengthens the need to understand how wind stress affects lakes.

Wind stress on the surface layer provokes significant mixing, leading to a mixed layer and a possible weakening of stratification. During the stratified period, a high vertical temperature gradient region (metalimnion hereinafter) acts as a barrier between the surface layer

(epilimnion) and the layer underneath the metalimnion (hypolimnion). Therefore, the hypolimnion is often considered to be isolated from meteorological forcing during summer. However, strong wind events such as typhoons are energetic enough to tilt the metalimnion from its equilibrium, changing the "barrier" elevation in the water column. After the wind ceases blowing, the metalimnion oscillates at periods depending on the lake's size, and redistributes to various scales the energy received from the wind until the metalimnion reaches its state of equilibrium. These oscillations of the metalimnion are what we call internal waves (Mortimer CH, 1952). Figure 1.1 is a schematic of the generation of internal waves.

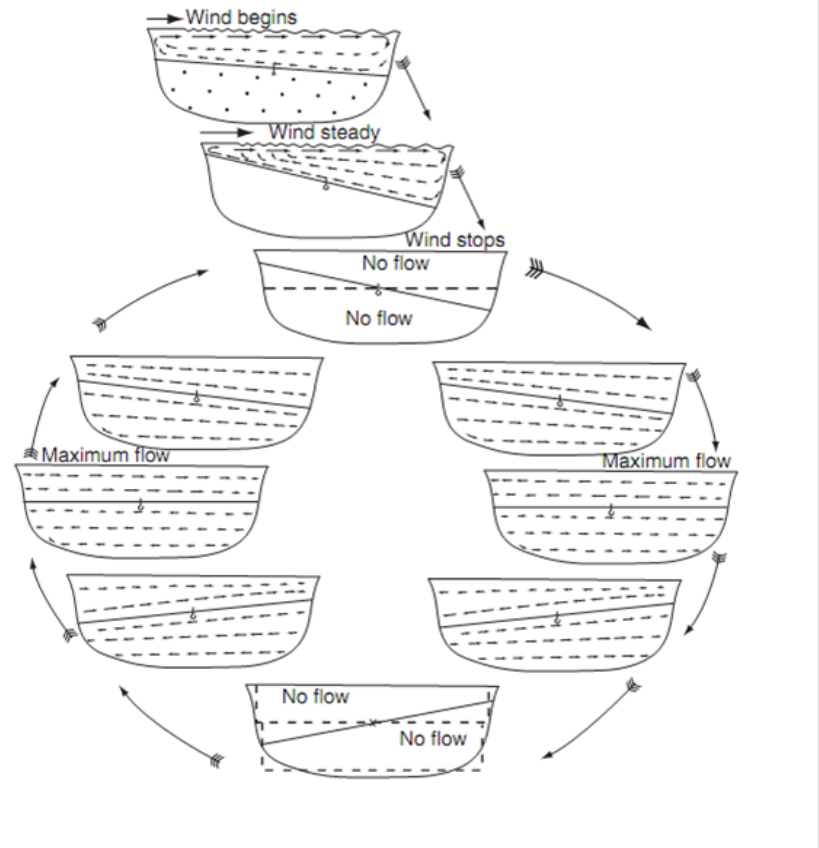

Figure 1.1: Internal wave generation - How the internal waves are generated in a stratified lake, after Boegman 2009 adapted from Mortimer CH 1952

Saggio & Imberger (1998) and MacIntyre *et al.* (1999) have provoked a renewal of interest about internal waves in lake by discovering the contribution of an internal wave field to turbulence enhancement. This redistribution of energy from internal waves to small scales may occur anywhere in the lake such as on rough topography (MacIntyre *et al.*, 1999) or near the benthic boundary layer (Wüest *et al.*, 1996). Each event generates enhanced turbulence within the water column and increases diapycnal mixing (mixing between two layers

of different density; in stratified case diapycnal mixng is considered to be vertical). Several studies have been carried out to understand the link between the internal wave field and turbulence activity (Lorke, 2007; MacIntyre *et al.*, 2009a). This relationship has been called "energy flux path" (Imberger, 1998). Understanding this relationship will clarify what type for wave is responsible of this energy redistribution and where this redistribution occurs.

In lakes, internal waves can be categorized into three length scale: basin-scale internal waves, free gravity waves and non-linear waves (Wüest & Lorke, 2003). Figure 1.2 shows the power spectrum of internal waves before and after a typhoon during the BITEX experiment in Lake Biwa in 1993. After the typhoon had exited the natural modes of the lake, consistent peaks appear in the spectra after the typhoon, whereas before the typhoon they were absent. In looking at the buoyancy frequency range ($10^{-3} \sim 10^{-2}$ Hz), the power increased 100-fold after the typhoon passage, suggesting intense activity in this range in the metalimnion region.

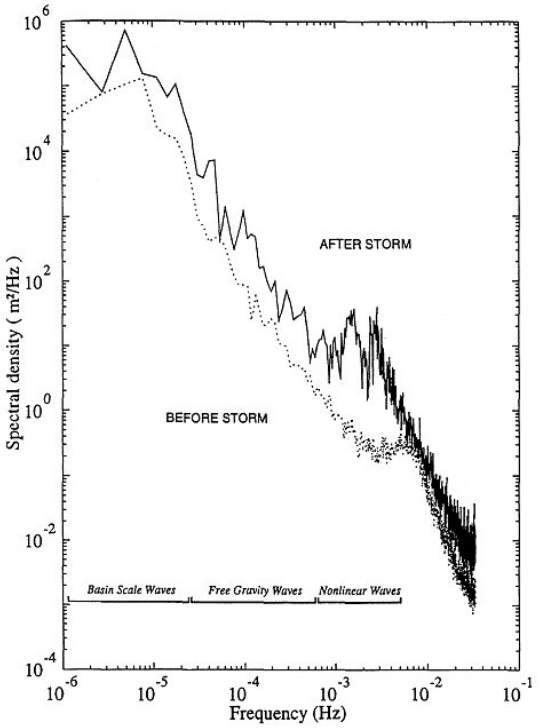

Figure 1.2: Spectra of isotherm elevation before and after typhoon in Lake Biwa - Spectra of isotherm displacements in Lake Biwa, estimated from 10 days long data before (*dotted line*) and after (*solid line*) the passage of a typhoon. After Wüest & Lorke (2003) reproduced from Saggio & Imberger (1998)

The significant role of turbulence and mixing in the ocean has been highlighted by the one order discrepancy between estimated global vertical diffusivity (Munk, 1966; Munk &

Wunsch, 1998) and observed vertical diffusivity within the ocean interior. This statement underlines the important role of shallow area and rough topography for dissipating the energy stored within the ocean. Moreover Lewis *et al.* (1986) have emphasized that turbulent fluxes of nutrient through the metalimnion play a significant role in supporting new production in the upper water column. Internal waves are features that propagate through the metalimnion and may ultimately break in shallow areas. Therefore it would make them a good candidates as a cause of the total energy dissipation. MacIntyre & Jellison (2001) documented turbulence at the top part of the metalimnion while internal waves were propagating. Intermittently, this turbulent region generated vertical transport of nutrient through the metalimnion, and this flux was sufficient enough to counteract the nutrient limitation and support a modest growth of phytoplankton in the surface layer. Also Yamazaki *et al.* (2010) show the impact of physical processes on biochemical materials in the water column in documenting a quiescient layer (weak turbulence) with high abundance of bio-chemical material surrounded by high turbulence layers.

Because of the correlation between turbulent mixing in the water column and internal waves, understanding how the internal wave field redistributes the energy to turbulent scale will lead us to knowledge about when and where turbulent mixing occurs and ultimately the impact of these ubiquitous features on the biochemical material concentration in the lake.

1.2 Background

Experiments were carried out to address what type of wave provokes enhanced turbulence and mixing at the boundaries. In using the data obtained from a thermistor chain Saggio & Imberger (1998) show that after a typhoon the potential energy of low-frequency internal waves increased 10-fold whereas moderate-to-high frequency internal waves energy increased 100-fold. They noticed a two-day modulation of the latter's energy as well as a delay of one day in the increase of energy. Therefore they inferred that there was a transfer of energy from basin-scale internal waves to high-frequency internal waves. Saggio & Imberger (1998) estimated how many days it would take for the internal wave field to dissipate the kinetic energy due to turbulence in the lake interior making use of the results presented in

Etemad & Imberger (1998). The discrepancy between their estimation (about 100 days) and the observed time of total dissipation (a few days) highlights the dominance of boundary region in the dissipation of the wave field . They hypothesized a breaking of the high-frequency internal waves at the boundaries, hence loosing their energy through mixing.

Later, Boegman *et al.* (2005a) and Boegman *et al.* (2005b)'s laboratory experiment corroborated the role of high-frequency internal waves for the loss of energy on boundaries. Lorke (2007) also concluded that enhanced turbulence is due to high-frequency internal waves at boundaries in a field experiment in Lake Constance. Lorke (2007) reached this conclusion, because basin-scale periods were not observed in the velocity spectrum measured at the experiment location (boundary), whereas they were visible in the main basin. Therefore he infers a transfer of energy from basin-scale internal waves to high-frequency internal waves and then to mixing at the boundaries.

When comparing vertical diffusivity estimated from a tracer experiment and basin-averaged values from microstructure deployments during an internal wave event, a discrepancy between these results appears and thus underlines the complexity of the occurence of mixing (Wüest *et al.*, 2000). Goudsmit *et al.* (1997) noted that when the tracer reached the bottom, the diffusivity increased significantly in comparison with the lake interior, leading to the statement of a dominant role of the boundaries mixing process. In their review of turbulence in lakes, Wüest & Lorke (2003) concluded, based on several microstructure experiment results, that the transfer of energy from basin-scale motion to turbulence takes place mainly in the bottom boundary layer, supporting the assumption of breaking high-frequency internal waves as a source of energy transfer where the metalimnion reaches the bottom. They also concluded that the water column can be divided into three layers: a turbulent surface layer and, to a lesser extent but still significant, a turbulent bottom boundary layer (Figure 1.3). Several studies revealed that the third layer, hypolimnion, is considered as turbulence-free offshore and that the turbulent mixing is at the order of molecular level 10^{-7} m^2 s^{-1} (Münnich *et al.*, 1992; Wüest *et al.*, 2000).

Using a modal analysis, Shimizu & Imberger (2008) noted that the damping of internal waves is primarly caused by bottom friction. Later, Boegman (2009) estimated that 90% of seiche energy is dissipated within the boundaries of small to medium sized lakes. Seventy

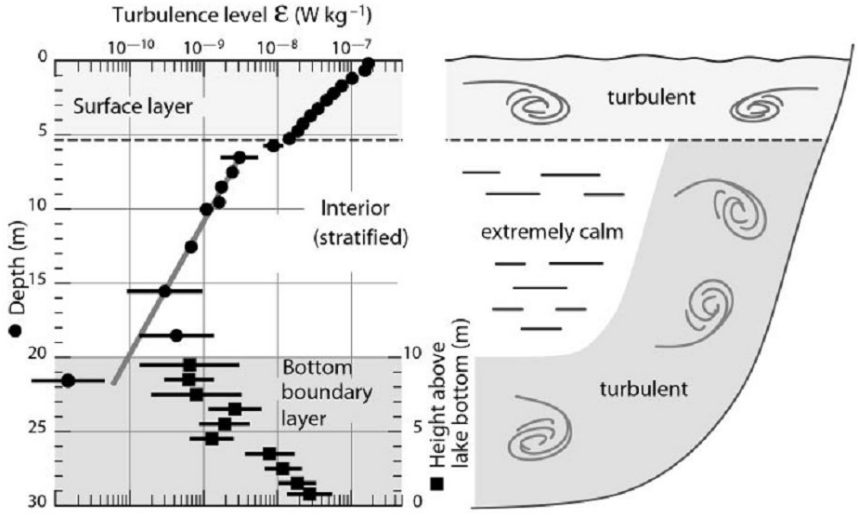

Figure 1.3: A three-layer system and related turbulence activity - This figure represents how turbulence activity is usualy seen in the water column, with two high turbulence layers, surface and bottom boundary layer, and an almost turbulent-free layer the lake interior offshore, from Wüest & Lorke (2003).

five percents of energy is dissipated due to bottom friction, and 25% by high-frequency wave breaking and the remaining 10% is dissipated intermittently within the interior. Figure 1.4 represents the energy flux path presented by Boegman (2009). However such decomposition of energy redistribution is not known for large lakes. A possible explaination of this great dissipation at the boundaries is the fact that currents, mainly generated by basin-scale internal waves, may weaken as the water gets closer to the bottom, because of the effect of bottom friction, and generates horizontal velocity gradient (velocity shear) and turbulence. Lorke *et al.* (2002) showed agreement between observed velocity profiles and the Law of the Wall (LOW hereinafter), which is a logarithmic scale, where

$$u(h) = \frac{u_*}{\kappa} \ln \frac{h}{z_0} \tag{1.1}$$

h being the distance from the bottom, z_0 the roughness length, u_* the friction velocity and κ the von-Karman constant. This equation leads to the turbulence activity, or turbulent kinetic energy dissipation rate,

$$\varepsilon = \frac{u_*^3}{\kappa h} \tag{1.2}$$

as a function of distance from sediment. This equation predicts the increase of ε toward the bottom boundary.

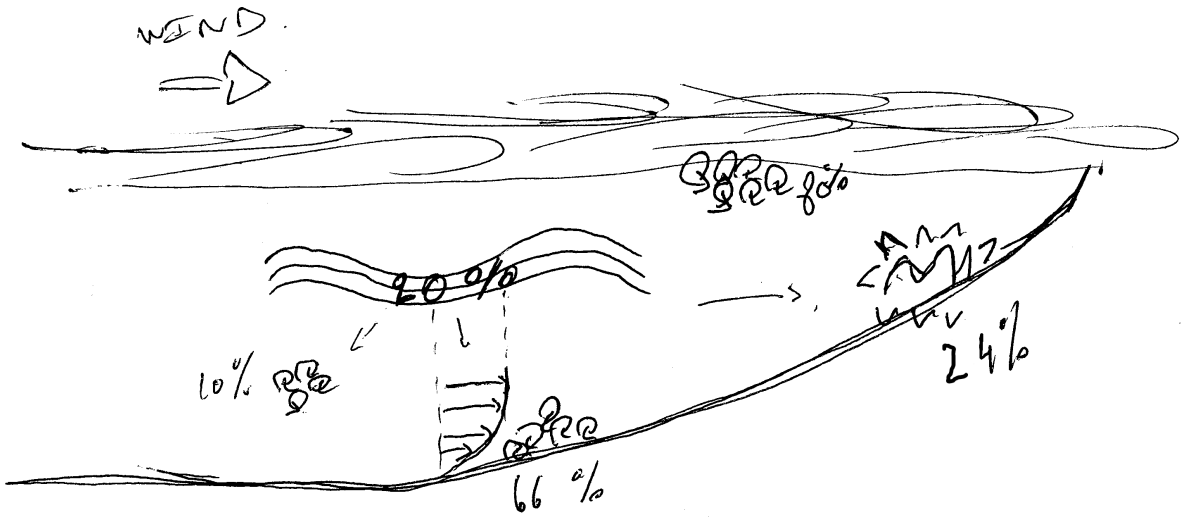

Figure 1.4: Energy redistribution so far - A schematic of the energy redistribution from wind energy to turbulence reviewed by Boegman (2009)

Most of the campaigns aimed at estimating the turbulence enhancement during internal wave propagation were either sparse over a long period of time (Etemad & Imberger, 1998; MacIntyre *et al.*, 2009a) or focusing on a specific layer (Lorke, 2007). Etemad & Imberger (1998)'s experiment provided 14 microstructure profiles spread out over 18 days and 5 different locations. These profiles displayed strong stratification ($N^2 > 10^{-3}$ s^{-2}), which is a necessary condition for the presence of internal waves. Therefore, it is likely they may have missed other interesting processes involving low- and high-frequency internal waves.

Lorke (2007) moored a thermistor chain with a downward-looking ADCP and mounted an ADV on the bottom. The mooring system provided a 4 month long dataset of the layer from the bottom up to 1.7 meters above the bottom where the thermocline reached the bottom boundary. Even though this configuration measured the layer for a long time, the authors could not obtain a picture of turbulence intensity distribution in the whole water column during the sampling period.

However, a recent study carried out by MacIntyre *et al.* (2009a), who used the same method as Saggio & Imberger (1998), suggests that low-frequency internal waves can play a dominant role in the energy dissipation. Also, MacIntyre *et al.* (2009b) documented strong 2-day averaged turbulent diapycnal diffusivity ($K_z \sim 10^{-5}$m^{2}s^{-1}) in the hypolimnion likely generated by internal waves. Unfortunately, they did not show direct evidences of direct

energy transfer from low frequency waves to turbulence. The conclusions of these two studies lead to no clear consensus on energy redistribution. Therefore, it is still unknown if low-frequency internal waves may redistribute the energy toward turbulence without going through the energy cascade proposed by Saggio & Imberger (1998).

1.3 Layout of the thesis

The objective of this thesis is to provide a better picture of the "energy flux path" initiated by Imberger (1998), since it seems incomplete in current literatures. I intend to reach this goal by studying the turbulence activity in Lake Biwa (Japan) while an internal wave field propagates and assess the impact on the bay. This study consists of both a field study and numerical simulation.

After the introduction, the thesis presents some fundamental knowledge on internal waves in Chapter 2, such as the types of waves and how they are categorized. In Chapter 3, I present the results of a field experiment which was done using a series of ADCPs, the microstructure profiler named TurboMAP (JFE Advantec, Japan) and a fine scale probe (F-probe) provided by LBERI. The experiment was conducted in August 2001 inside Shiozu Bay, which is a side bay in Lake Biwa (Japan). The experiment period was one week after the passage of a typhoon close to Japanese shores. In this chapter I estimate the turbulence activity in the water column at a fixed point inside the bay and I identify the basin-scale internal wave field from the ADCP data.

In Chapter 4, I make use of a numerical model, SUNTANS (Stanford Unstructured Non-hydrostatic Terrain-following Adaptive Navier-Stockes Simulator), to understand the fate of the low-frequency internal wave field within Shiozu Bay. After explaining why I used this numerical model, I introduce a method to set up the initial conditions for the typhoon event using heat fluxes and wind stress. Then I compare simulated and observed data to assess the consistency of the results. Finally, I will use this dataset to explain the dynamics inside Shiozu Bay and provide insight into the process that may have generated the turbulence event.

Lastly, major conclusions obtained from the previous sections, limitations of this thesis

and recommendations for future work are presented in Chapter 5.

Chapter 2

Theory on basin-scale internal waves in lakes

2.1 Response of the lake

Lakes come in various shapes and sizes. In literature, they are often categorized based on their size: small, medium or large. Depending on the size of the lake, the response to a same level of wind is different. In order to assess the response, the Wedderburn number is sometimes computed. This non-dimensional parameter represents the ratio between the gravity restoring force and the wind forcing. Suppose a simple two-layer system, the Wedderburn number can be defined as follows: :

$$W = \frac{g' h_1^2}{L u_*^2} \tag{2.1}$$

where $g' = \frac{\delta\rho}{\rho}$ is the reduced gravity accross the base of the surface layer, h_1 the thickness of the surface layer, L a characteristic length of the lake, u_* the friction velocity due to wind. For a situation where $W << 1$, the wind forcing is stronger than the gravity restauring force, leading to a tilting of the metalimnion. In assuming the same stratification and the same wind forcing for lakes, we can notice that W will decrease as L increases. This relationship highlights the role of the size of the lake on the tilting of the metalimnion as a response of the wind forcing, which can be explained by the integrated work done by the wind on the lake

Table 2.1: Period of the main internal wave encountered in three lakes, at different point in time

Lake	L (km)	Period	Source
Biwa / Japan (summer)	50	45.5 hrs	Kanari (1975)
Biwa / Japan (autumn)	50	53 hrs	Kanari (1975)
Kinneret / Israel (summer)	20	22 hrs	Shimizu & Imberger (2010)
Kinneret / Israel (spring)	20	44 hrs	Shimizu & Imberger (2010)
Constanz / Germany (autumn)	40	90 hrs	Appt *et al.* (2004)

surface, seen as fecth. A large lake would mean a wide surface for the wind to cover, so the impact of an identical wind event would be significant in a large lake surface in comparison with a small lake surface.

Since tilted metalimnion is the origin of the internal wave field, a comparison of the main internal wave encountered in lakes at different size, found in the literature, will underline the discrepancy that may exist between the lakes.

Table 2.1 presents the fact that each lake's response to wind forcing is different, especially the period of the internal waves. Moreover we note that vertical and horizontal modes are used in the description of internal waves. Even though periods are different among the lakes, vertical and horizontal modes are useful features of the internal wave field. Vertical mode one and two are the most encountered in lakes. Vertical mode one waves are encountered when the uppper and bottom part of the metalimnion are synchronously tilted, whereas vertical mode two appears when the upper and bottom part are tilted out-of-sync.

As mentioned previously, internal waves exhibit several vertical modes. These modes modify the distribution of current velocity in the water column, as well as the location of isotherms. An analytical expression of the current velocity profile depending on the vertical mode can be computed by assuming the case of internal seiche, taking the equations following the main horizontal axis, parallel to the direction of propagation of the wave:
Conservation of density

$$\frac{\partial \rho}{\partial t} + u\frac{\partial \rho}{\partial x} + w\frac{\partial \rho}{\partial z} = 0 \tag{2.2}$$

X-momentum equation (without rotation)

$$\rho\frac{\partial u}{\partial t} + \rho u\frac{\partial u}{\partial x} + \rho w\frac{\partial u}{\partial z} = -\frac{\partial P}{\partial x} \tag{2.3}$$

z-momentum equation

$$\rho\frac{\partial w}{\partial t}+\rho u\frac{\partial w}{\partial x}+\rho w\frac{\partial w}{\partial z}=-\frac{\partial P}{\partial z}-\rho g \tag{2.4}$$

Where ρ is the density of the water, $\mathbf{U}=(u,w)$ is the velocity vector, g the acceleration of gravity and P the water pressure. In neglecting the density gradient (Boussinesq approximation) we obtain this differential equation

$$\psi_{zz}+\frac{N^2}{c^2}\psi=0 \tag{2.5}$$

where N is the buoyancy frequency, $c=\frac{NH}{n\pi}$ $n=1,2\ldots$ is the phase speed of the wave and ψ is the stream function such as

$$u=\frac{\partial\psi}{\partial z}\quad,\quad w=\frac{\partial\psi}{\partial x} \tag{2.6}$$

In Figure 2.1 I show the horizontal and vertical velocity profile depending on the vertical mode of the wave (mode 1, 2 and 3 are shown). Both velocities were normalized by the maximum velocity. We notice that the values of the velocity vary depending on the vertical mode, as well as the pattern. We notice that vertical mode 1 (V1 hereinafter) waves possess the highest velocity field with opposite sign at the surface layer compared to the bottom layer. V2 waves generate current mainly in the metalimnion region (above and below the metalimnion the velocities are small). Also the results from Figure 2.1 suggest that the kinetic energy is mainly generated by the V1 internal waves, since currents associated with these waves are dominant.

Horizontal modes correspond to how many nodes the internal wave has, the node being the location where the wave is constantly at an equilibirum state. Basin-scale waves are considered as linear waves since the set of linear equations represent their behavior well. In assuming only one horizontal component along the direction of propagation of the wave, the following linearized equation is obtained (Gill, 1982):

$$\frac{\partial^2\eta}{\partial t^2}+C_0^2\frac{\partial^2\eta}{\partial x^2}=0 \tag{2.7}$$

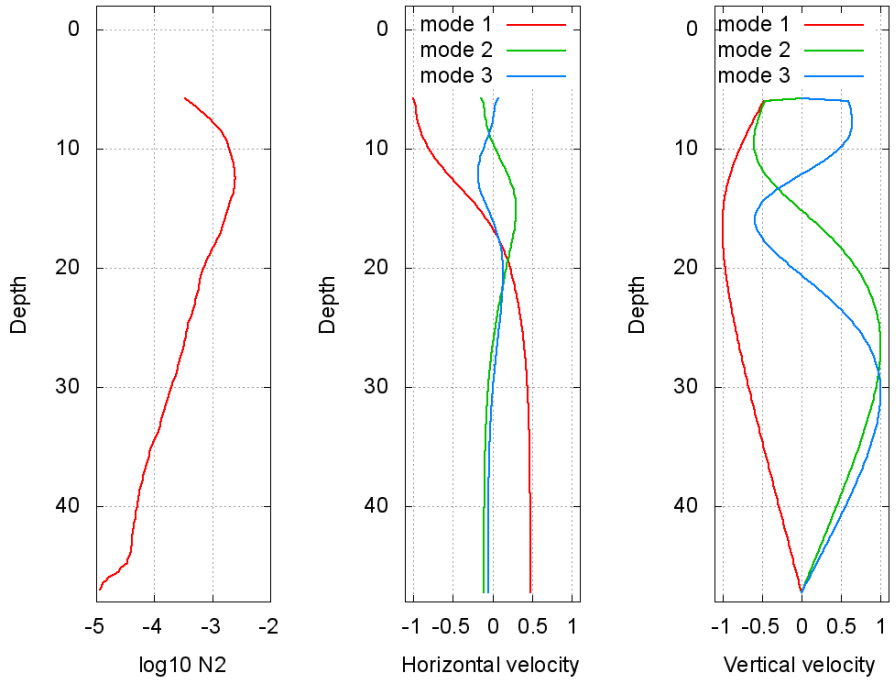

Figure 2.1: Vertical modes - Horizontal and vertical velocities computed from eq. 2.5 based on a profile of 2-day averaged squared buoyancy frequency from a campaign in Lake Biwa in August 2001 (left panel). Central panel shows profiles of horizontal velocity associated with the first three vertical modes. Right panel pictures profiles of vertical velocity associated with the first three vertical modes.

Where η is the interface elevation, $C_0 = (g'h_1h_2/(h_1+h_2))^{1/2}$ is the velocity of the main internal wave in a two-layer system, h_1 and h_2 are the thickness of layers 1 and 2, and g' the reduced gravity. In assuming further a medium as a rectangle of length L, the solution of 2.7 is expressed as follows :

$$\eta_n(x,t) = -\frac{8\eta_0}{(n\pi)^2}\cos(C_0\frac{n\pi}{L}t)\cos(\frac{n\pi}{L}x) \tag{2.8}$$

Equation 2.8 represents the analytical expression of the internal wave phase elevation as a function of distance x, time t and the horizontal mode of the wave n. The higher we go to the horizontal mode, the equation displays the diminution of the wave amplitude, therefore reducing the internal wave's role in the potential energy. According to Boegman (2009) 98% of the potential energy is detained by the first horizontal mode. Figure 2.2 represents the first three horizontal modes, illustrating the decrease of the internal wave amplitudes and the nodes.

As seen earlier horizontal mode 1 internal waves are considered to possess 98% (Boeg-

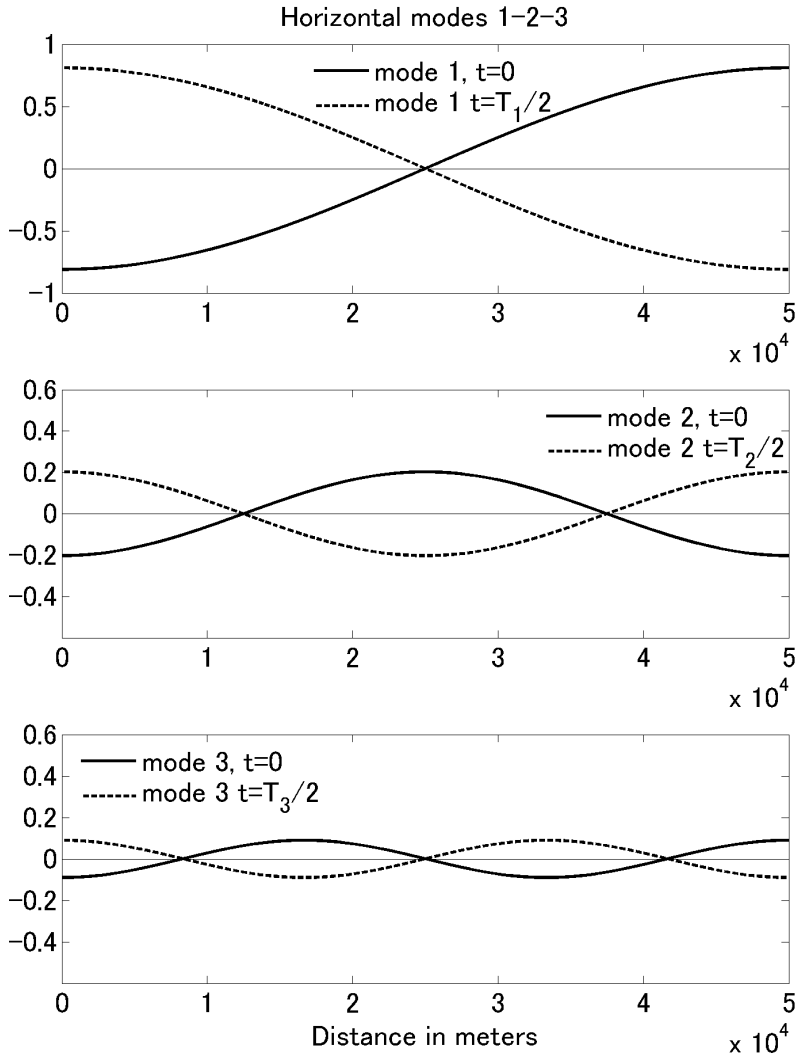

Figure 2.2: Horizontal modes - Elevation of an isotherm at t=0 and t=T_n/2 with $n = 1 \ldots 3$ associated to the first three horizontal modes

man, 2009) of the potential energy of the internal wave field, and the first vertical mode 1 waves plays a significant role in the kinetic energy generation. Therefore, I can infer that the total energy field of the internal wave field is mainly detained by the basin scale internal wave horizontal and vertical mode 1. This statement strengthens the need to conduct research on he energy flux path by the basin-scale internal waves.

2.2 Period of internal waves

Table 2.1 describes that the period of internal waves is a function of the lake size as well as the time of the year. These variations make clear the dependency of internal wave period on the lake size and the stratification of the lake. The period of the waves depending on the vertical and horizontal mode can be computed by assuming the water column can be separated into several layers of constant density in a rectangular lake (Münnich *et al.*, 1992):

$$T_{n,m} = \frac{2L}{m\sqrt{g\lambda_n}} \tag{2.9}$$

where L is the characteristic length of the lake of l layers, n and m are the vertical and horizontal mode, respectively and λ_n is obtained from the following equation:

$$\det\left(\mathbf{A} - \lambda\mathbf{I}\right) = \mathbf{0} \tag{2.10}$$

where $\mathbf{I}$ is the identity matrix (the diagonal is filled with 1, whereas the rest is filled with 0), and $\mathbf{A}$ is written as:

$$a_{jk} = \begin{cases} H_k & \text{for } j \leq k \\ \frac{\rho_k}{\rho_j} H_k & \text{for } j > k \end{cases} \tag{2.11}$$

with $i, j = 1, \ldots, l$, where ρ_i is the density of layer number i. The equations underline the influence of the stratification with the presence of the density gradient as well as the size of the lake. However the method to compute the period of an internal wave, based on the lake's size and the stratification, depends on what mode we want to focus on. For instance, if we focus on a vertical mode 2 wave, we need to split the water column into at least three layers.

Thanks to profiles of temperature, we can identify internal wave modes based on the

equations presented earlier. By looking at the pattern of the horizontal velocity current profile associated to the wave, for instance, the vertical mode of the encountered wave can be extracted. If enough thermistor chains are spread throughout the lake, the horizontal mode of the wave can be clearly identified. Because the period of an internal wave depends on the horizontal and vertical modes of the wave, one still can have an idea about the internal waves' modes, with temperature profiles at one single location.

2.3 Large lakes and Earth's rotation

As mentioned at the beginning of this chapter, lakes differ in size and shape. Although the dynamics may be similar, another effect has to be accounted for when one deals with large lakes: Earth's rotation or Coriolis effect. Earth's rotation starts to affect the dynamic of the internal gravity waves when the size of the lake is comparable to the Rossby radius of deformation (R_R), such as:

$$R_R = \frac{C_0}{f} \tag{2.12}$$

where $f = \frac{2}{24*3600} sin(\phi)2\pi$ is the inertial frequency in rad s^{-1}, $C_0 = \sqrt{g\lambda_0}$ the phase speed of the first baroclinic mode wave of the lake, and λ_0 is computed from equation 2.10. In a temperate climate $R_R \sim 5$ km, which implies that a lake with a characteristic length larger than 5 km, the basin-scale internal waves will be affected by the rotation of the earth. The Coriolis force will force the basin-scale internal waves to rotate cyclonically (counter-clockwise in Northern hemisphere) or anti-cyclonicaly (clockwise in the Northern Hemisphere). These waves are respectively called Kelvin wave and Poincaré wave.

Internal Kelvin waves are gravity waves that balance the Earth's Coriolis force against a topographic boundary, i.e., coastline. Therefore currents associated with this type of wave are parallel to the direction of propagation (current perpendicular to the boundary are non-existent). Moreover, they always propagate with the shore on the right side of the propagation direction in the Northern hemisphere (the shore is on the left side in the Southern hemisphere). And their rotation pattern is counter-clockwise in the Northern hemisphere (cyclonic hereinafter). The analytical expression of the interface elevation caused by the

Kelvin wave can be computed from the linearized equations.

$$\frac{\partial u}{\partial t} - fv = -C_0^2 \frac{\partial \eta}{\partial x} \tag{2.13}$$

$$\frac{\partial v}{\partial t} + fu = -C_0^2 \frac{\partial \eta}{\partial y} \tag{2.14}$$

$$\frac{\partial \eta}{\partial t} + \frac{\partial u}{\partial x} + \frac{\partial v}{\partial y} = 0 \tag{2.15}$$

Assume the elevation η can be expressed as the sum of a geostrophic component (η_g) and a nongeostrophic component (η_{ng}). In addition, assume that the geostrophic balance dominates on the longitudinal axis (x-axis) and that the nongeostrophic motion excels on the latitudinal axis (y-axis) in a rectangular lake of width B km and L km in length:

$$\begin{aligned} -fv &= -C_0^2 \tfrac{\partial \eta_g}{\partial x}, \\ \tfrac{\partial v}{\partial t} &= -C_0^2 \tfrac{\partial \eta_{ng}}{\partial y}, \\ \tfrac{\partial \eta}{\partial t} = \tfrac{\partial \eta_g}{\partial t} + \tfrac{\partial \eta_{ng}}{\partial t} &= -\left(\tfrac{\partial u}{\partial x} + \tfrac{\partial v}{\partial y}\right) \end{aligned} \tag{2.16}$$

By using the following boundary conditions:

$$\begin{aligned} u|_{x=0} &= u|_{x=B} = 0, \\ v|_{y=0} &= v|_{y=L} = 0, \\ \eta_g|_{x=B/2} &= 0, \\ \eta|_{y=0,t=0} &= \eta_0 \end{aligned} \tag{2.17}$$

a solution for the elevation is extracted and it is expressed as follows(Kanari, 1975):

$$\eta(x,y,t) = \frac{f\eta_0}{C_0}(x - \frac{B}{2})\sin(n\pi\frac{y}{L})\sin(2n\pi\frac{t}{T}) + \eta_0\cos(n\pi\frac{y}{L})\cos(2n\pi\frac{t}{T}) \tag{2.18}$$

where C_0 is the phase speed, and η_0 a coefficient representing the initial amplitude. In equation 2.18, we notice the presence of the Rossby radius of deformation inversed ($\frac{1}{R_R} = \frac{f}{C_0}$) in the right side of the equation. Morever this term stands for the amplitude of the Kelvin wave in the perpandicular plan to a shoreline on the y-axis, and it shows a decrease of the wave amplitude away from the coast to the center of the lake. These two statements

emphasize the need of a large lake to be able to observe internal Kelvin waves in a lake. If we take small lakes, such as $B_{lake} << R_R$ the component of the wave's elevation on the x-axis will be negligible, leading to an internal standing wave.

The dispersion relationship associated with the Poincaré wave is expressed as follows (Gill, 1982):

$$c^2 = \frac{\omega^2 - f^2}{k^2 + l^2} \tag{2.19}$$

where k and l are the horizontal wavenumbers of the wave, f the inertial frequency and ω the wave's frequency. This equation reveals some information on the frequency of the wave. According to this formula, $(\omega^2 - f^2) > 0$ implies that the frequency of the Poincaré wave is always larger to the inertial frequency.

Internal Kelvin wave and Poincaré wave do not differ only by their frequency, but also by their rotation pattern and the velocity field associated with them. Internal Kelvin waves are known to propagate cyclonically whereas internal Poincaré waves propagate anti-cyclonically. Internal Kelvin waves are boundary-trapped waves and generate a velocity field that is maximum at the boundaries and parallel to the shoreline with no velocity at the center of the lake. However Poincaré waves exhibits a flow field that is maximum at the center of the lake, and zero velocity at the boundaries.

Energy repartition In the paragraph about the vertical and horizontal modes, it has been mentionned that the potential and kinetic energy are dominated by the basin-scale internal waves. However the ratio of these energies has not been dealt with. In small-to -medium size lakes, basin-scale internal waves are considered as linear waves since a linear equation reproduces their dynamics well. For linear waves the partition of potential and kinetic energy is equal, i.e. if we compute the ratio of the potential energy to kinetic energy we would obtain unity.

However, when introducing the earth's rotation in the computation, the ratio changes. Gill (1982) computed the ratio for linear progressive waves in a lateraly unbounded, rotating system where the wavelength of the waves is much smaller than the basin scale. He

concluded that the ratio is expressed as:

$$\frac{PE}{KE} = \frac{w^2 - f^2}{w^2 + f^2} \tag{2.20}$$

w being the angular frequency of the wave motion and f the inertial frequency. Internal waves with a frequency close to the inertial frequency possess a higher kinetic energy than potential energy, whereas when the frequency is higher, the ratio reaches unity. However low-frequency internal waves in large lakes are affected by the Earth's rotation (Kelvin and Poincaré waves) with frequencies smaller or similar than the inertial frequency and wavelength being of the same order as the basin size. Moreover the ratio expressed by Gill (1982) does not hold in the low-frequency internal waves in a lake. Antenucci & Imberger (2001) adressed this issue and concluded that, in the case of low frequency internal waves in a lake, the ratio is greater than unity for low horizontal modes and substantially less than unity for higher horizontal modes.

Chapter 3

Hypolimnetic turbulence generation associated with superposition of large-scale internal waves in a strongly stratified lake: Lake Biwa, Japan

3.1 Location and instruments

3.1.1 Location

In order to understand how the large scale internal wave field can be directly linked to enhancement of turbulent events, I started my research with data from a field experiment carried out during the last week of August 2001 in Lake Biwa, located in Shiga prefecture in Japan. As we can see in Figure 3.1, Lake Biwa belongs to the category of large lakes because the characteristic length of Lake Biwa is much larger than the Rossby radius of deformation, commonly encountered in the temperate regions ~ 5 km (dimension of the lake in table 3.1), which makes internal Kelvin and Poincaré waves more likely to be observed in Lake Biwa. Previous studies in Lake Biwa, for instance Shimizu *et al.* (2007) and Saggio & Imberger (1998), observed such waves. Moreover we notice that Lake Biwa possesses two side-basins, called the Southern Basin and Shiozu Bay (north part of the lake). For the purpose of the

study, namely of large-scale internal waves, the Southern Basin can be disregarded since it is too shallow (averaged depth is about 4 m) to allow internal waves to enter the basin during summer time. Therefore the experiment was undertaken in Shiozu Bay. Documentation of Kelvin wave-like oscillations done by Okamoto & Endoh (1995) further confirms the suitability of this location documentation of oscillation-like Kelvin wave in the bay conforts us in the choice of the location. During the summer season, Japan usually experiences many typhoons, so a chance of observing low-frequency internal waves in Lake Biwa is high.

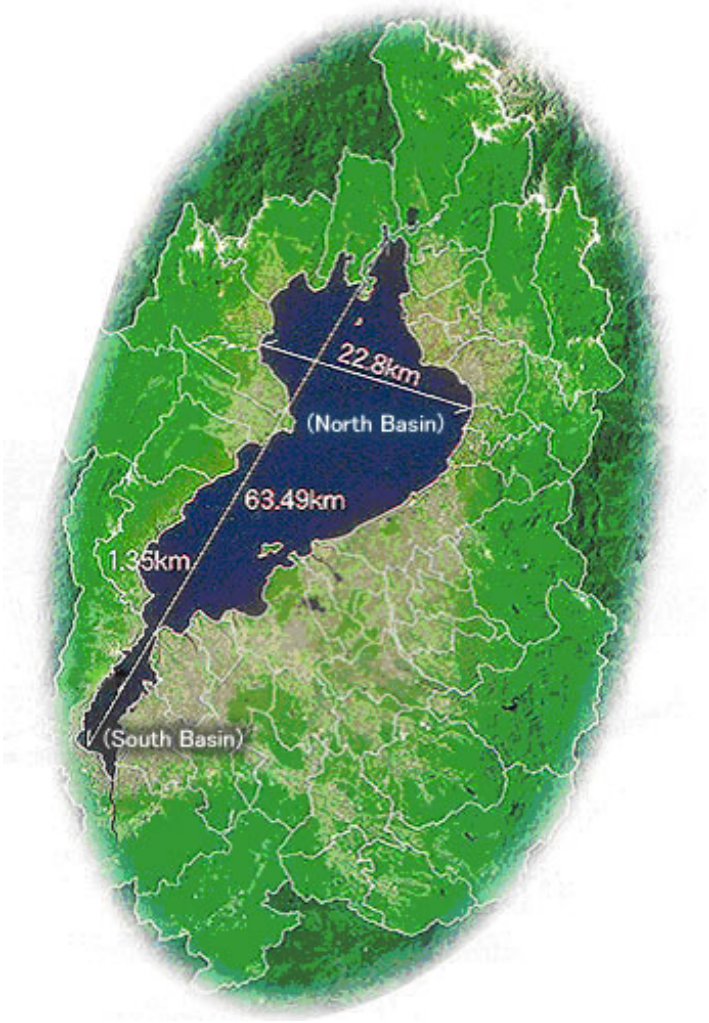

Figure 3.1: Lake Biwa - Map of Lake Biwa with main dimensions

3.1.2 Method

The reason I used this dataset is because about one week before the beginning of the main part of the field experiment, a typhoon passed along the Japanese shore. To prove the presence of a typhoon, we can look at satellite images and wind time series. Thanks to the

Table 3.1: Dimensions of Lake Biwa

Major Axis length	63.49 km
Widest crossing length	22.8 km
Norrowest crossing length	1.35 km
Deepest point	103.58 m
Average depth (Northern Basin)	43 m
Average depth (Southern Basin)	4 m

typhoon database "agora-typhoon" I can obtain the trajectory of the typhoon as well as the dates. Also, meteorological stations of the Japanese Meteorological Agency (JMA) are scattered all over Japan, measuring wind velocity and direction. Five stations are located around Lake Biwa (Nagahama, Hikone, Minami-komatsu, Otsu and Imazu). Making use of the data obtained at these five stations, we can analyze the wind velocity during the typhoon passage close to the Japanese coast, thus confirming the presence of a typhoon in the vicinity of Lake Biwa.

After extracting the trajectory of the typhoon from the database (agora.ex.nii.ac.jp/digital-typhoon/index.html.en), I display the trajectory on a map and assess how close to Lake Biwa the trajectory was (Figure 3.2a). This figure shows that on August 21 and 22, the typhoon's trajectory was close to Lake Biwa, suggesting strong winds over the lake. Figure 3.2b is the time series of 1-hour averaged and daily maximum wind velocity at Hikone Station. Looking at this figure, I notice that strong gusts of wind were present from August 21 to 22, with hourly-averaged velocity reaching 8 m s^{-1} and daily maximum velocity attaining 17 m s^{-1}. After the typhoon event, hourly averaged wind speeds showed a diel periodicity, with maxima typically in the afternoon. From August 23 to 26, maxima were only 2 - 3 m s^{-1}, whereas from August 27 to 31 winds were northwesterly with maxima near 6 m s^{-1}.

3.1.3 Instruments

The deployment took place at the mouth of Shiozu Bay (Figure 3.3) from the R/V *Hakken*. The experiment consisted in a free-fall microstructure profiler, TurboMAP in Fig. 3.4 (Wolk *et al.*, 2002) on August 29 to measure turbulence using a shear probe, as well as a fast-response temperature sensor, FP07, in addition to standard hydrographic (CTD) and bio-

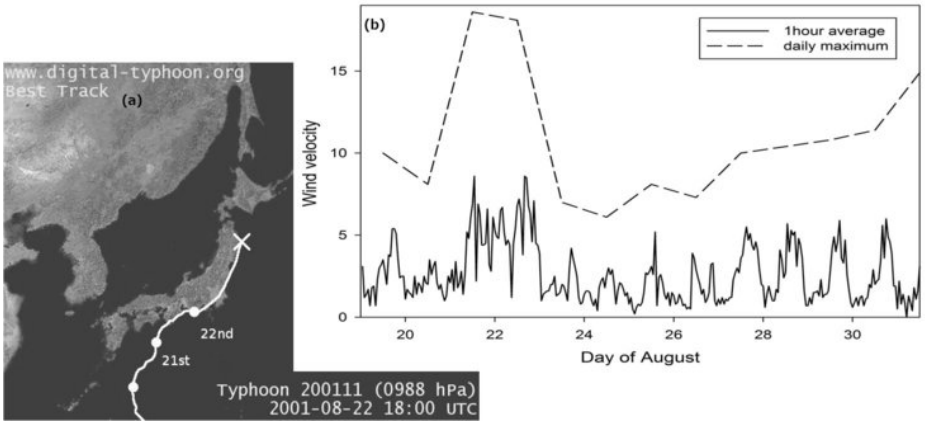

Figure 3.2: Proof of a typhoon's passage close to Lake Biwa - (a) Trajectory of a typhoon between August 21 to 23 based on satellite images. (b) Wind velocity time series extracted from AMEDAS stations located at Hikone. Solid line reprensents hourly-averaged wind velocity and dash line represents the daily maximum velocity. The unit of wind velocity is m s^{-1}

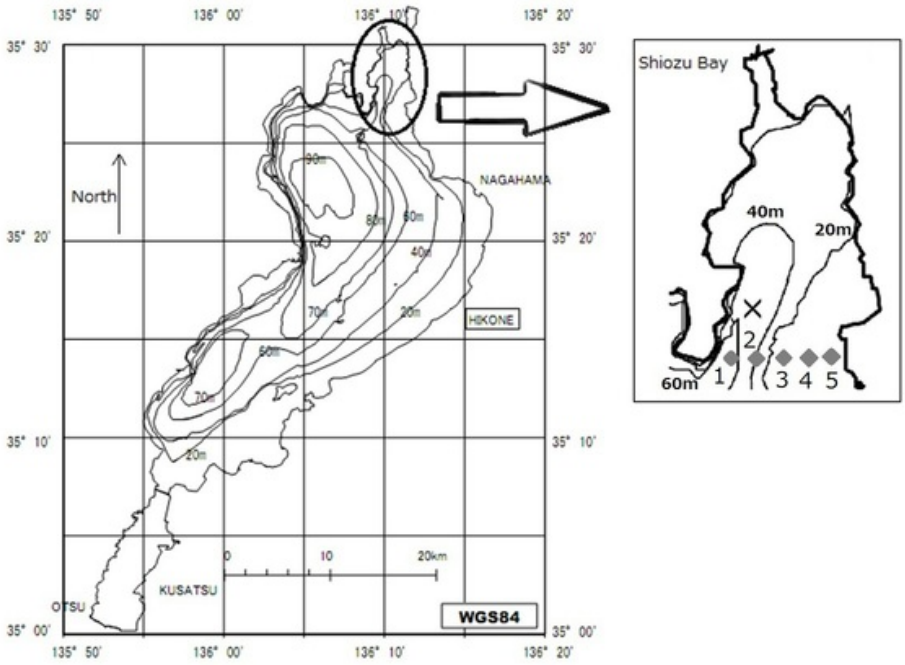

Figure 3.3: Experiment locations - Shiozu Bay in Lake Biwa (*cirlced*), and experiment site with F-probe and TurboMAP (X) (depth = 53 m) and ADCP stations (*gray diamond*).

optical (turbidity and fluorescence) parameters. The depth at the experiment site was approximately 53 m, and the deepest point reached by the instrument was 48 m. The profiler sank in free-fall mode with the falling speed at 0.7 m s^{-1}. The experiment was designed to measure the intensity of turbulence as a response of the lake to internal-wave propagation. Each channel of TurboMAP was sampled at 256 Hz. Unfortunately, the turbidity and the fluorescence probe of TurboMAP experienced some technical problems that made fluorescence data unusable and provoked a discrepancy in the turbidity data between the first day and the second day. Despite the discrepancy, the turbidity data are used qualitatively. The schedule of the TurboMAP deployment was 5 profiles in the first 15 minutes of each hour for 48 hours. Although the optic probe required technical servicing on August 31, we were able to obtain 220 microstructure profiles.

Figure 3.4: TurboMAP - a photograph of the microstructure profiler TurboMAP: Turbulence Ocean Microstructure Acquisition Profiler

Along with TurboMAP, another instrument, a fine scale profiler (F-probe, in Figure 3.5), was deployed hourly, providing fluorescence intensity and dissolved oxygen, as well as a redundancy of temperature, conductivity and pressure data. The maximum depth of each profile was 50 meters. The sampling frequency of the F-probe was 50 Hz, and 48 profiles were obtained during the experiment. Table 3.3 lists all the sensors that equipped the profiler.

The boat was equipped with a weather station during the experiment, allowing us to measure wind velocity and direction, as well as air humidity and air temperature.

Five Acoustic Doppler Current Profilers (ADCPs) were deployed at the mouth of Shiozu Bay to measure current velocity and direction. They were assigned Station 1 to 5 from west to east (Fig. 3.3). ADCPs at Stations 2, 3 and 5 were immersed at 12:00 (local time) on

Table 3.2: List of parameters measured by TurboMAP and the sampling frequency at which they are measured

Parameter	Unit	Sampling Frequency
Horizontal Velocity Shear	s^{-1}	256 Hz
Temperature(slow)	°C	256 Hz
Temperature (FP07)	°C	256 Hz
Conductivity	mS/cm	256 Hz
Pressure	dbar	256 Hz
Fluorescence	Relative Unit	256 Hz
Turbidity	Relative Unit	256 Hz
Acceleration X-axis	G	256 Hz
Acceleration Y-axis	G	256 Hz
Acceleration Z-axis	G	256 Hz
Sinking Velocity	m s^{-1}	256 Hz

Figure 3.5: F-probe - a photograph of the fine scale probe: F-probe

Table 3.3: List of parameters measured by the F-probe and the sampling frequency at which they are measured

Parameter	Unit	Sampling Frequency
Temperature	°C	50 Hz
Conductivity	S/m	50 Hz
Pressure	dbar	50 Hz
Fluorescence	Relative Unit	50 Hz
Turbidity	Relative Unit	50 Hz
Dissolved Oxygen	ml/l	50 Hz
pH	Relative Unit	50 Hz

August 24 and recorded data until August 31, thus providing seven days of current data. The other two ADCPs recorded at Station 1 between August 29 and 31 and at Station 4 between August 24 and 26. The sampling time interval was 5 minutes at Stations 1, 2 and 3, and 2 minutes at Stations 4 and 5. Previous studies in Lake Biwa, with similar conditions (Saggio & Imberger, 1998), documented basin-scale internal waves with a period of 1 day and longer. Therefore, in this study we used data from Stations 2, 3 and 5 for internal-wave frequency analysis since Stations 1 and 4 did not provide data long enough to clarify a low-frequency wave field. The ADCP at Station 1 was set to start measuring from 1 meter above the bottom, Stations 2 and 3 measured from 6 meters above the bottom, and Stations 4 and 5 from 13 m and 1.5 m above the bottom respectively.

Figure 3.6: ADCP - a photograph of one of the five ADCPs deployed at the mouth of Shiozu Bay

3.2 Results

3.2.1 Profiles

Figure 3.7 shows an example of the measurements made by TurboMAP. The temperature profile (center panel, green curve) shows a large temperature gradient between the epilimnion ($\sim 26^{\circ}$C) and the hypolimnion ($\sim 8^{\circ}$C). The decrease of temperature seems to occur in two steps from 8 meter depth to 17 meters and then a slow variation from 17 m to the end of the profile. Moreover in looking at conductivity profiles, I notice that values of conductivity are very low, about 6×10^{-2} mS cm^{-1}, leading to a salinity of 0.03 psu. Typical oceanic values for conductivity are about 50 mS cm^{-1}, and salinity 34 psu. Since salinity is very low in Lake Biwa, the role of salinity on the stratification will be neglected in this study. On the right panel, Fig. 3.7 displays the bio-optical parameter measured by the profiler. Looking at this figure one can notice the increase of fluorescence intensity throughout the profile. However as mentioned earlier the bio-optical probes required servicing during the experiment, leading to unusable fluoresence data, thus it is not shown. However, turbidity intensity profiles revealed qualitatively-usable data even though data from the first and second day showed a discrepancy. In Fig. 3.7 the turbidity profile (black curve in the right panel) exhibits high values between 10 to 25 m depth and relatively low values close to the surface and close to the bottom.

The strength of this dataset is the two-day-long microstructure experiment, which allows me to assess the temporal variation of turbulence activity in the water column during the propagation of internal waves. Since the signature of internal waves is the variation of temperature distribution in the water column, I look at profiles of temperature and velocity shear changes over time (Figure 3.8). As it is noticeable, temperature profiles seems to deepen or shallow over time (20 $^{\circ}$ C is about 13 m deep during the cast 82, 16 m deep during cast 142 and 12 m deep during the cast 182), suggesting the presence of internal waves in Lake Biwa. Moreover profiles of velocity shear show a variation over time. More precisely, shear below 30 m seemingly is weak at the beginning of the experiment then gains strength during the middle of the experiment. At the end of the experiment shear below 30 m recovers a very weak activity.

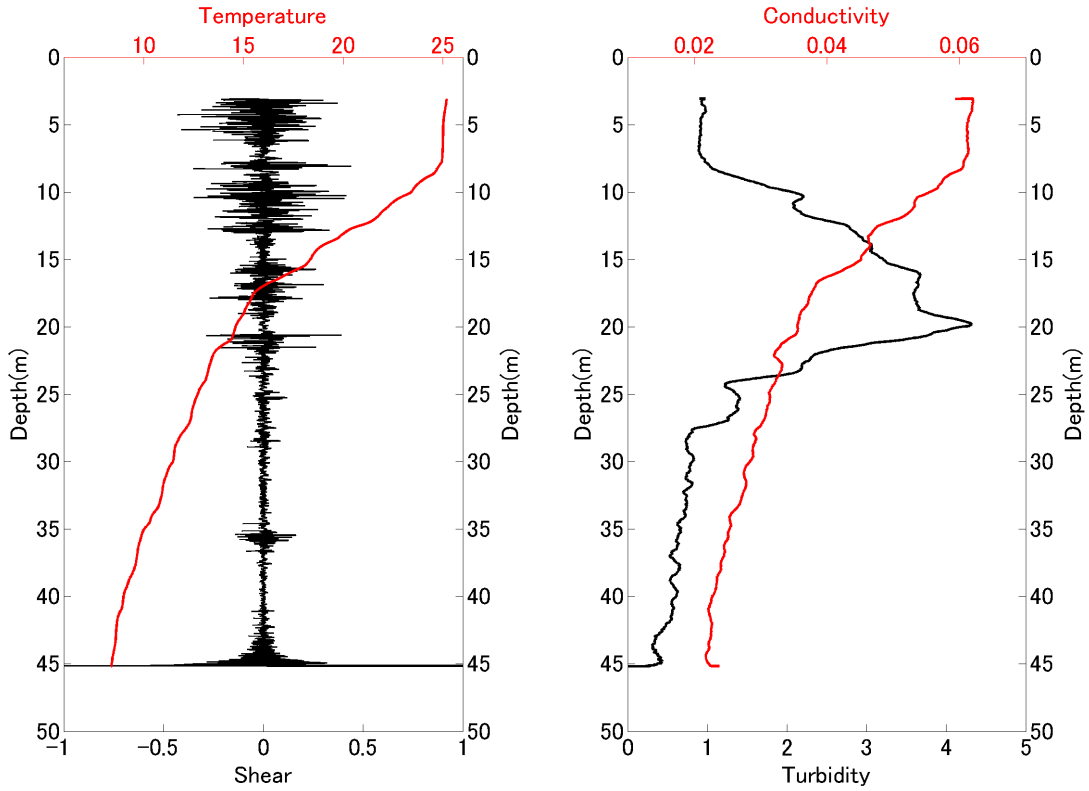

Figure 3.7: Parameters of TurboMAP - Profiles made from cast number 82 (day 30.216) using TurboMAP. Profile in the first left panel is a profile of horizontal velocity shear (black curve) in s^{-1} and temperature data (red curve) in °C. The right panel displays conductivity in mS cm^{-1} (red curve) and turbidity (black curve) profiles.

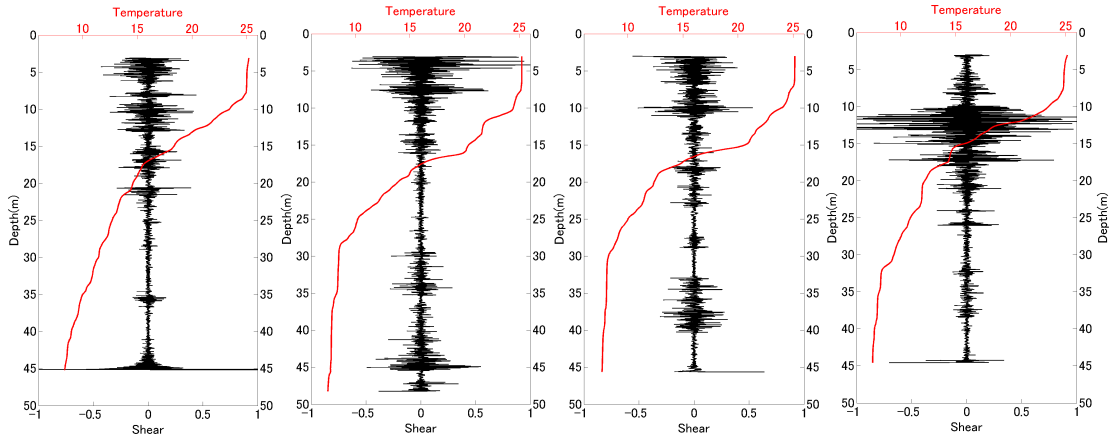

Figure 3.8: Evolution of shear and temperature over time - Four sets of shear (black curve) and temperature (red curve) profiles at cast, from left to right, 82 (day 30.216), 132 (day 30.6715), 142 (day 30.7542) and 182 (day 31.2097).

Even though the activity of turbulence is based on turbulence velocity shear, we cannot quantify the activity of turbulence in using shear. The intensity of turbulence is expressed in terms of the kinetic energy dissipation rate, ε.

$$\varepsilon = \frac{\nu}{2}\left\langle\left(\frac{\partial u_i'}{\partial x_j}+\frac{\partial u_j'}{\partial x_i}\right)\left(\frac{\partial u_i'}{\partial x_j}+\frac{\partial u_j'}{\partial x_i}\right)\right\rangle \quad , \quad i,j=1,2,3 \tag{3.1}$$

Making use of the local isotropy theory of turbulence, as well as stationarity and homogeneity, the dissipation rate can be expressed as follows:

$$\varepsilon = \frac{15}{2}\nu\left\langle\left(\frac{\partial u'}{\partial z}\right)^2\right\rangle \tag{3.2}$$

where u' is the horizontal component of turbulent velocity and ν the kinematic viscosity. $\left\langle\left(\frac{\partial u'}{\partial z}\right)^2\right\rangle$ represents the variance of turbulence shear and is estimated from a velocity shear spectrum. The integrated shear spectrum was compared against the Nasmyth empirical spectrum (Oakey, 1982) in order to estimate turbulent shear variance consistently. Each value of ε corresponded to a variance of 512 points of shear data. This data block was roughly equivalent to a 1.5-m thick layer in the water column.

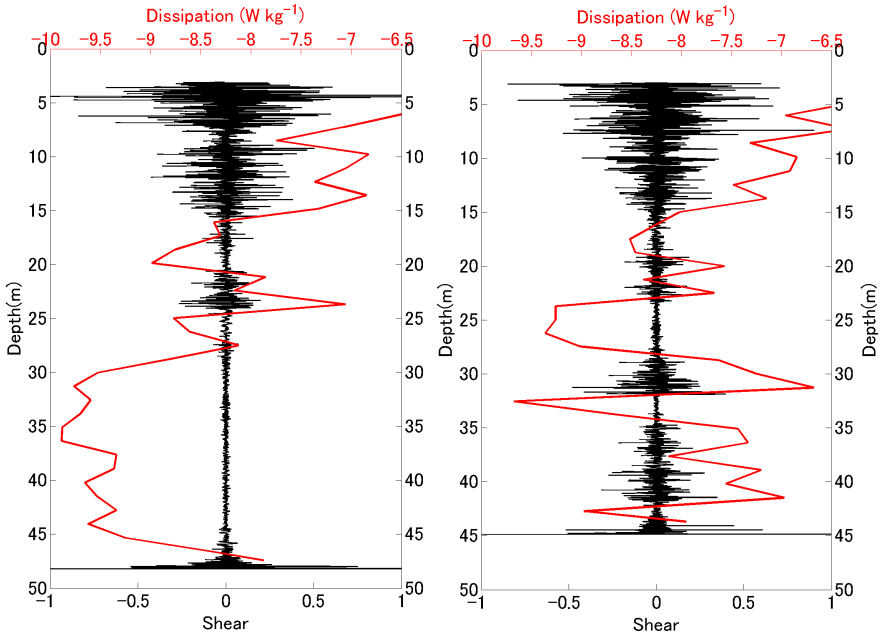

Figure 3.9: Energy dissipation rate - Two samples of turbulent velocity shear profile (*thin black line*) and the associated turbulent kinetic energy dissipation rate (*thick red line*) in logarithmic scale (Unit: W kg $^{-1}$)

3.2.2 Vertical and temporal distribution

When looking at selected profiles at several points in time, the temporal evolution of the parameters is not clear, so the distribution of each parameter over time and depth is plotted from here. TurboMAP and F-probe provided a picture of biological and physical events as a response to an internal wave field.

TurboMAP's data According to data from TurboMAP, the surface temperature was 26 °C during the day and 25 °C at night. At 45 meters depth, the temperature remained at about 8 °C during the whole microstructure experiment (Fig. 3.10). The clear vertical displacement of isotherms in the lake interior, with amplitude of 5 meters, alludes to the presence of propagating internal waves. Temperature profiles showed a strong temperature oscillation between 10 and 30 meters depth during the experiment. The temperature decreased from 24 °C to below 10 °C in this depth range, indicating a strong stratitification in this depth range. Using the squared buoyancy frequency, N^2, based on the density field, I quantify the stratification level of the water column and it is expressed as:

$$N^2 = -\frac{g}{\rho_0}\frac{\partial \rho}{\partial z} \tag{3.3}$$

where g is the gravitational acceleration, z the vertical coordinate taken positive upward, ρ_0 the mean density and ρ the local density. The peak of N^2 was on the order of 10^{-3} s^{-2} between 8 and 18 meters depth and decreased to 10^{-4} s^{-2} below 30 m (Fig. 3.11), supporting the statement of a strong stratification during the experiment. However, on August 30 between 00:00 and 12:00 local time, the N^2 value of 10^{-4} s^{-2} appeared around 40 m depth as the isotherms deepened.

As mentioned earlier in this thesis, even though the turbidity sensor provided data with a discrepancy between day 1 and day 2, turbidity data are used qualitatively. Figure 3.12 shows how the turbidity intensity varies over time and depth. Also isoline of squared buoyancy frequency are overlaid to easily compare with the stratification shown in Fig. 3.12. Overall, the tubidity distribution exhibits the same pattern as described in Figure 3.7: low turbidity at the top and bottom of the water column and a local maximum in the middle of the water

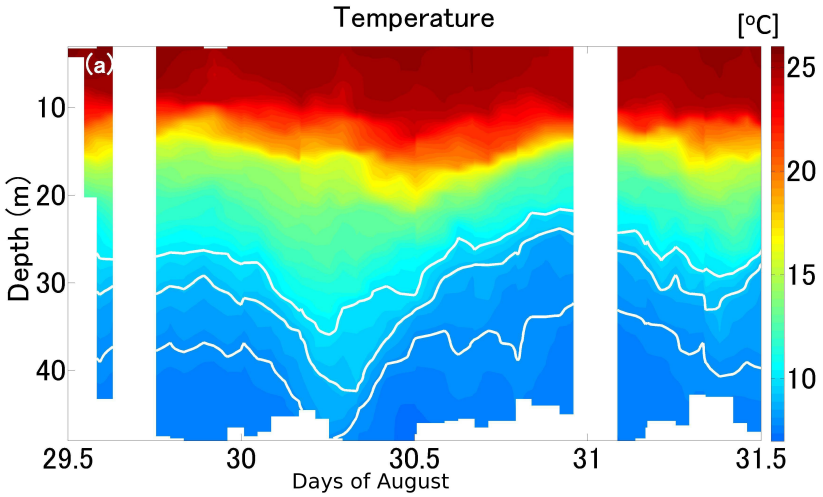

Figure 3.10: Temperature - Temperature (°C) distribution measured throughout the TurboMAP-experiment, depth in meters and days written as decimal days of August. White solid lines are 8-9-10 °C isotherms

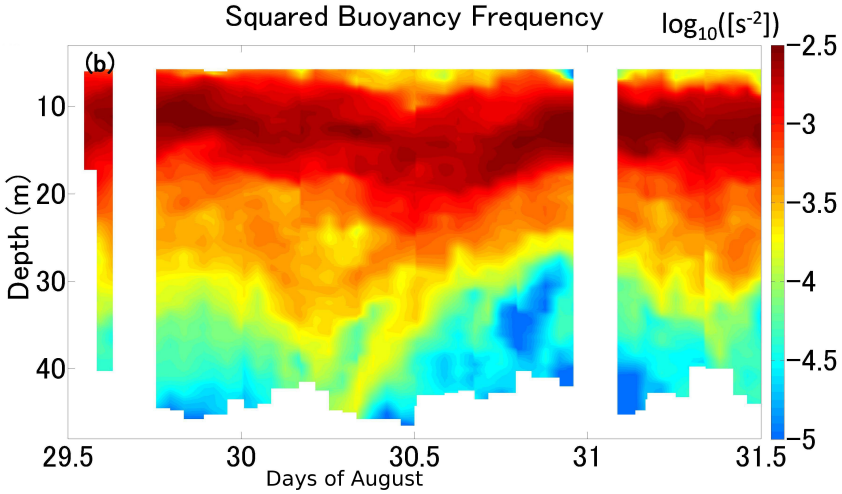

Figure 3.11: Squared buoyancy frequency - Distribution of N^2 in logarithmic scale, unit: [s^{-2}]. Depth in meters and days written as decimal days of August.

column. Also I notice that the high turbidity layer in the middle of ther water column shows a wave-like oscillation, but is not necessarlly inside the high N^2layer ($> 10^{-3}$ s^{-2}). However the most interesting part of this figure is what occurred at the bottom of the profile. Indeed, during the first day the turbidity intensity below 40 m depth was about 1 unit, whereas during August 30 morning (starting at about day 30.25 in August) a local high intensity (4 units) occurred. Moreover I notice that this local high turbidity is associated with weak stratification ($N^2 < 10^{-4}$ s^{-2}). This statement suggests that the high-turbidity water originates from the bottom.

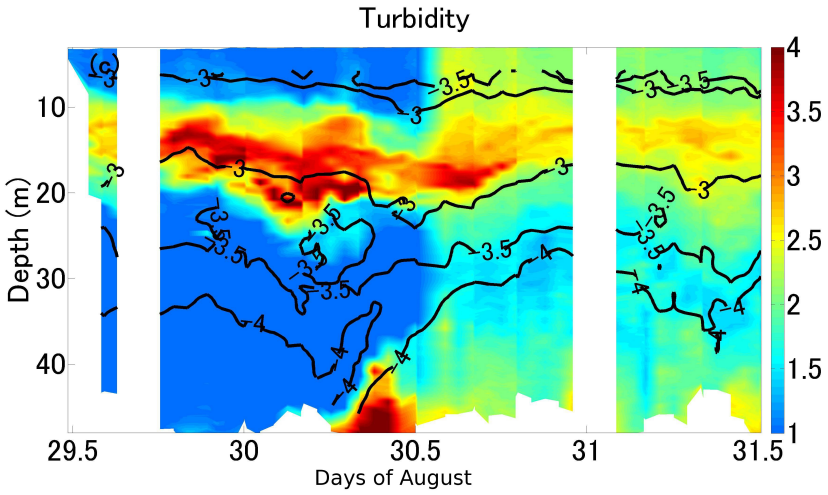

Figure 3.12: Turbidity - Distribution of turbidity in the water column, with N^2 isoline (solid line) of -4,-3.5,-3. Depth in meters and days written as decimal days of August

Figure 3.8 shows that velocity shear strength varied over time in the data set. After computation of ε I look at its temporal variation. By looking at the first and last 12 hours of the experiment, I can make an analogy with the three layers water column (Figure 1.3), except that the profiles do not reach the bottom, so I cannot observe the bottom boundary layer. However I clearly see a mixing layer at the top ($\varepsilon \sim 10^{-7}$ W kg^{-1}) and quiescent layer below ($< 10^{-9}$ W kg^{-1}) (Figure 3.13). Surprisingly, in the region below 35 meters, the water experienced a turbulent state, with ε on the order of $10^{-8} \sim 10^{-7}$ W kg^{-1} during the daytime of August 30. The fact that enhanced turbulence started at the same time as the highly turbid water, at 40 meters depth on day 30, suggests a common trigger.

F-probe data Even though I could not use fluorescence data from TurboMAP, data from a fluorescence sensor mounted on F-probe were available. According to the F-probe

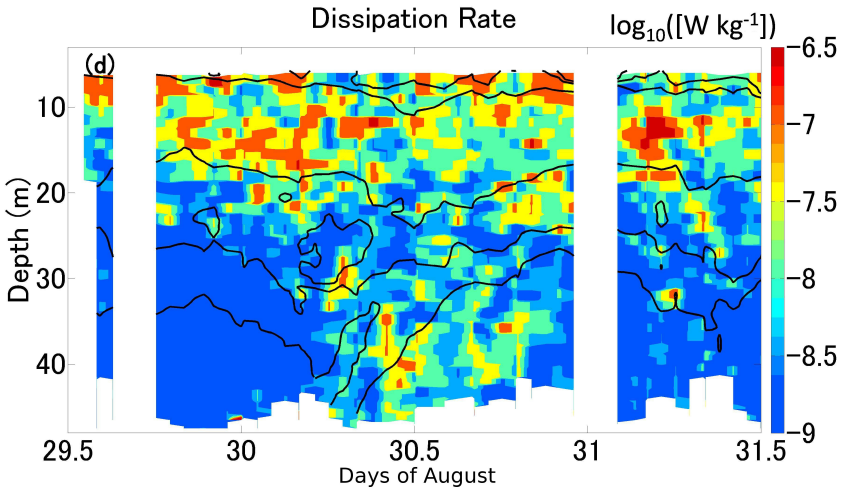

Figure 3.13: Turbulent kinetic energy dissipation rate - Distribution of ε in the water column in logarithmic scale (Unit: W kg^{-1}), with N^2 isoline (solid line) of -4,-3.5,-3.Depth in meters and days written as decimal days of August.

data set, relative fluorescence intensity diminished from 10 to 2 units from surface to hypolimnion during the experiment (Figure 3.14), with a rapid decrease in the metalimnion region. However, a local maximum (value of 3 units) appeared below 40 meters depth just before 12:00 on August 30. This local maximum, within the hypolimnion, was associated with a relatively high turbidity state (Figure 3.12). Since the high turbidity patch coincided with the local high fluorescence section, both features were probably driven by the same process. The section of high turbidity at 45 meters and the condition of low stratification ($N^2 \sim 10^{-5}$ s^{-2}) suggest that a resuspension of sediment from the bottom (53 meters) due to turbulence was responsible for this feature. Sakai *et al.* (2002) also observed sediment suspension during an internal wave event in Lake Biwa. Under these circumstances, the sediment suspension was likely linked to a low-frequency internal wave. The localized high turbidity (about 15 meters deep) is probably a layer of suspended material that was not due to elevated phytoplankton subsurface maximum since fluorescence signals do not show high fluorescence in the metalimnion region whereas it appears in the turbidity data. Increased inflow from local rivers caused by the typhoon's rain may be the origin of this feature.

TurboMAP data and seiche model Oscillations of isotherms at several periods are clues to the presence of internal waves in Lake Biwa. In order to investigate the period of the main basin-scale internal wave in the lake, a seiche model can be used. The model used in this study was based on an N-layered model system (Münnich *et al.*, 1992) and introduced

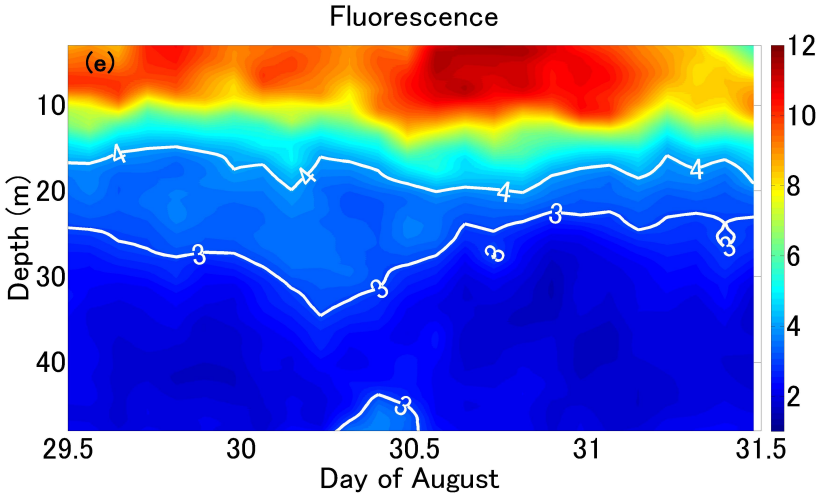

Figure 3.14: Fluorescence intensity - Distribution fluorescence relative intensity in the water column, with isoline of fluorescence intensity (*solid line*) of 3 and 4. Depth in meters and days written as decimal days of August.

in Chapter 2. For the study of the first baroclinic mode wave I assumed a two-layer medium. Therefore, we consider a two-layered rectangular lake 50 m deep and 50 km (L) long. Since high values of N^2 were located around 15 m depth, the first layer is taken to be 15 m thick (h_1) and the second one to be 35 m thick (h_2). For the computation, the period is expressed as

$$T_{n,m} = \frac{2L}{m\sqrt{g\lambda_n}} \tag{3.4}$$

where L is the characteristic length of the lake; n and m are the vertical and horizontal mode, respectively and λ_n resolves the equation:

$$\det\left(\begin{vmatrix} h_1-\lambda_n & h_2 \\ h_1\left(1-\frac{\Delta\rho}{\rho_1}\right) & h_2-\lambda_n \end{vmatrix}\right) = 0 \tag{3.5}$$

where $\Delta\rho$ is the density difference between the upper and lower layer, I use density data taken from TurboMAP profiles. In the case of a vertical mode 1 wave (V1), it appeared that two main periods can exist in Lake Biwa. The longest period is about 48.5 h corresponding to a horizontal mode 1 (H1), and a horizontal mode 2 (H2) with a period of 24.2 h also can exist. In lakes, internal waves are characterized by such modes. The first vertical mode wave will tilt along the metalimnion, with horizontal velocities in opposite directions above and below, whereas higher vertical mode waves have maxima in horizontal velocity in the

upper water column. The horizontal mode corresponds to the number of nodes the wave exhibits on the horizontal axis. With the period of the V1 internal wave the Rossby radius of deformation can be computed in using equation 2.12, and is equal to $R_R = 5.5$ km.

3.2.3 ADCP data

ADCP data at Stations 2, 3 and 5 permitted the analysis of the internal-wave field. According to the time series of these stations, we noticed several oscillating modes due to internal wave propagation (Figure 3.15). The frequency of these oscillations and their location in the water column were identified by the computation of the power spectrum at each depth bin of the ADCP data.

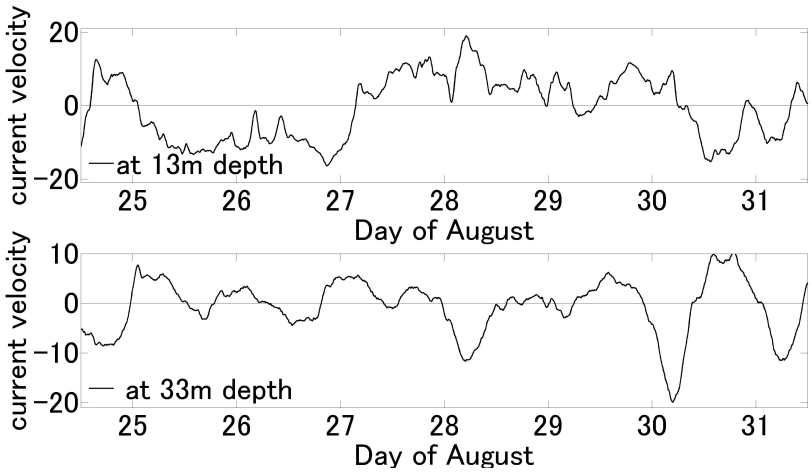

Figure 3.15: Sample of current time series - time series of northward current velocity (cm s^{-1}) of Station 3: (a) at 13 m depth and (b) at 33 m depth. Data were smoothed with a 1-h moving average.

Standard periodogram method for spectrum estimation is not suitable for the ADCP data in order to identify periodicity on an order of 1 day since the time series are not long enough to obtain statistically significant peaks in the low frequency range. Therefore, I made use of a parametric method, namely the Auto-Regressive (AR) model method, whose resolving power on short time series is greater than the conventional Fast Fourier Transform (Gangopadhyay *et al.*, 1989). Assuming each data point is a linear combination of previous data points, time series are expressed as follows:

$$x(t) = -\sum_{i=1}^{p} a_i \times x(t-i) + W(t) \tag{3.6}$$

where p is the model order, a_i the coefficients of the AR process, t the time step and W a white noise with zero-mean and σ_w^2 variance. The spectrum is expressed in the frequency domain:

$$S_{xx}(f) \quad = \quad \frac{\sigma_w^2}{\left|1+\sum_{j=1}^{p} a_j e^{-2\pi f j \Delta t \sqrt{-1}}\right|^2}, \; \frac{-1}{2\Delta t} \leq f \leq \frac{1}{2\Delta t} \tag{3.7}$$

The parameters a_j and σ_w^2, the variance of the white noise, are estimated from the time series by solving the Yule-Walker equation:

$$\tilde{\tilde{R}}_p . \tilde{a} \quad = \quad \sigma_w^2 \times \tilde{\delta} \tag{3.8}$$

where $\tilde{\tilde{R}}_p$ is the covariance matrix of the time series, $\tilde{a}$ the vector of the model coefficients, and $\tilde{\delta}$ the vector $\left| \begin{array}{ccccc} 1 & 0 & \cdots & 0 \end{array} \right|^{\mathrm{T}}$.

For convenience with this method, the ADCP time series were shortened prior to spectrum computation. At first I smoothed the time series to remove high frequency oscillations. Then, the sampling frequency was artificially reduced to one ninth of the original (i.e., ΔT=45 minutes for Stn 2 and 3 and ΔT=18 minutes for Stn 5) to focus on low-frequency periodicity.

The difficulty with this method is the choice of AR order. High order increases the fitness of the model to the original time series but generates spurious peaks in the spectrum, whereas low-order may suppress relevant peaks. We estimated the best model order of the spectrum by using the Akaike Information Criterion, *AIC* (Akaike, 1969):

$$AIC(p) \quad = \quad log\left[\sigma_w^2(p)\right] + \frac{2}{n}p \tag{3.9}$$

n being the number of samples. This criterion integrates the model order and a penalty for high model order. The best choice for the model order is indicated when the *AIC* attains its minimum.

The confidence interval was estimated from the large sample theory (Kay, 1988) and

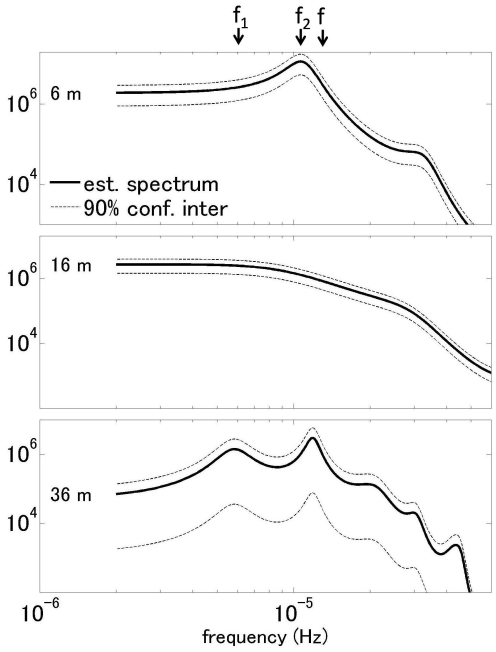

Figure 3.16: Spectral analysis - Current velocity spectrum and its confidence interval of 90% in the water column, at 6, 16 and 36 m depth at Station 3. The arrows indicate the main low-frequencies: $f_1 = 6.1 \times 10^{-6}$ Hz, $f_2 = 1.2 \times 10^{-5}$ Hz and the inertial frequency $f = 1.33 \times 10^{-5}$ Hz.

expressed as

$$S_{AR}(f) \begin{cases} \hat{S}_{AR}(f) \left[1 + z(1-\frac{\alpha}{2})\sqrt{\frac{2n}{p}}\right] \\ \hat{S}_{AR}(f) \left[1 - z(1-\frac{\alpha}{2})\sqrt{\frac{2n}{p}}\right] \end{cases} \tag{3.10}$$

where $z(1-\frac{\alpha}{2})$ stands for the $100 \times (1-\frac{\alpha}{2})$ percentage of a standard normal cumulative density function, $\hat{S}_{AR}(f)$ is the estimated spectrum and $S_{AR}(f)$ the true spectrum. Spectra were estimated from data at Stn 2, 3 and 5 since these data sets offered the longest duration among the five stations. Figure 3.16 represents spectra at several depths obtained from Stn 3 data. The figure shows two peaks in the low-frequency range. A low-frequency wave should be lower than, or close to, the inertial frequency in Lake Biwa (i.e. $f = 1.33 \times 10^{-5}$ Hz). The lowest frequency is $f_1 = 6 \times 10^{-6}$ Hz ($T_1 = 45.5$ h) and the second one $f_2 = 1.2 \times 10^{-5}$ Hz ($T_2 = 23$ h). These two frequencies are close to the ones computed from a seiche model. However, f_1 is noticeable only in the spectrum at 36 meters depth, whereas f_2 is present in all spectra except 16 meters depth, which corresponds to the location of the metalimion (Figure 3.11). The f_2 peak at 6 meters depth is at a slightly lower frequency than 1.2 10^{-5} Hz but it remains within the confidence interval; therefore, I considered both peaks to refer to the same internal wave. Although other peaks at higher frequency appeared, their energy level was low so they were considered not relevant to our discussion.

Two-day wave identification The identification of a 2-day wave was made through analysis of filtered current data from Stn 2 and 3 below 30 m depth. A Butterworth bandpass filter around the frequency $f_1 = 6.1\ 10^{-6}$ Hz was applied to the data. From this data I was able to assess the rotational pattern as well as the longitudinal speed at which the phase of the wave propagates. A comparison of the northward and eastward (Figure 3.17) time series at the mouth of Shiozu Bay, suggests a cyclonic propagation in the northern basin. The comparison highlights a time lag of about 2.5 hours between the two stations, with signals at Station 2 lagging behind those at Station 3 at 39 m depth. With the distance between Stations 2 and 3 ($\sim$800 m) we can estimate the longitudinal phase speed (0.1 m s^{-1}). This phase speed is much smaller than the phase speed estimated from the two-layer model ($\frac{2L}{T}$ $\sim$0.6 m s^{-1}). This result suggests that at the mouth of the bay, the wave propagates primarily northward, with a direction of propagation almost parallel to the east side shore. The 2-day internal wave features correspond to a Kelvin wave propagating cyclonically in the northern basin and entering into Shiozu Bay. Therefore, northward currents would be dominant at the experiment location, which is confirmed also in Figure 3.17. This observation is consistent with Okamoto & Endoh (1995), who observed 2-day-long isotherm oscillations at the north end of Shiozu Bay, which was linked to a first baroclinic mode Kelvin wave propagating in the northern basin of Lake Biwa. Saggio & Imberger (1998) also observed a similar phenomenon in Lake Biwa. Since these previous observations were consistent with our data, I consider the observed 2-day wave to be a Kelvin wave vertical mode 1 and horizontal mode 1 (V1H1 hereinafter). The lack of a 2-day oscillation in the surface layer (Figure 3.16) can be explained by the influence of the strong diurnal wind (Figure 3.2) on the surface layer current. Current associated to the Kelvin wave above the thermocline would be overcome by the winds, leading to a lack of peak at f_1 in the spectrum.

One-day wave identification The second internal wave I identified, 1-day wave, and the diel wind were in phase during the period between August 28 and 31, suggesting a linkage between them. On the other hand they were uncorrelated during the period between August 24 and August 27 (Figure 3.18). A comparison of wind velocity against current velocity time series reveals a large increase in current amplitude when the northwesterly

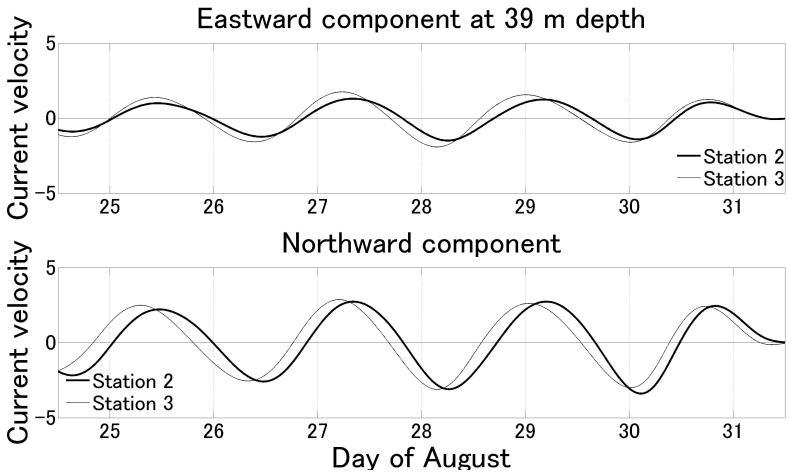

Figure 3.17: Currents associated with Kelvin wave (time series) - Comparison of northward and eastward currents associated with a 2-day wave at 39 m depth between Station 2 and Station 3. Both data were filtered with a Butterworth band-pass filter around $f_1 = 6 \times 10^{-6}$ Hz, applied back and forth in order to avoid any phase shift. Current velocity is in cm s^{-1}.

diel wind started to blow on August 28 (Figure 3.18b). Comparing the current velocity to the wind velocity in a scatter plot (Figure 3.18c), from August 28 to the end of the ADCP experiment, shows a strong correlation between these parameters, confirmed by a correlation coefficient of 0.83. The hypothesis of our time series being correlated was accepted at a 0.05 significance level. This correlation between current amplitude and daily wind velocity points to a strong internal wave resonance. Saggio & Imberger (1998) listed the internal waves they encountered in Lake Biwa after the passage of a typhoon over Japan in summer. This frequency was linked to either a Poincaré wave V1H2 or an inertial wave V1H1. One of the features of a Poincaré wave is its clockwise propagation (Shimizu *et al.*, 2007). In our data set, the signal of northward currents are in advance at Station 5 compared to Station 2 and Station 3 (Figure 3.19). Since this basin-scale wave was generated by the typhoon in the main basin, large enough to be affected by the Coriolis force, its rotational pattern could be deduced by the time lag at the mouth of the bay. In our case, this 1-day wave exhibits a cyclonic propagation in the main basin. Diel isotherm oscillations in Figure 3.10 allude to the presence of the 1-day wave in Shiozu Bay. However, we do not have a clear idea about the fate of this wave after it entered Shiozu Bay. During our observation no equivalent wave came out from the bay. Because inertial wave's frequency remains between the inertial frequency (f) and the medium's buoyancy frequency (N), I identified the diel wave as a Kelvin wave being vertical mode 1 and horizontal mode 2, corroborating the results from the

modal analysis.

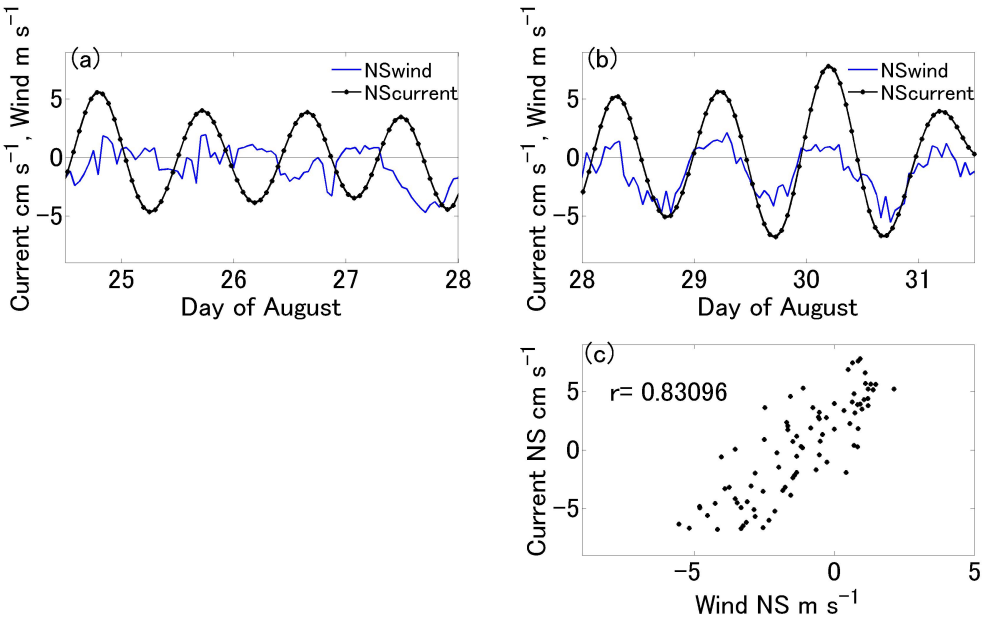

Figure 3.18: Correlation wind 1 day wave - (a) Comparison between current velocities (cm s^{-1}) associated with the daily wind and wind velocity (m s^{-1}) at 7 m depth at Station 2 from August 24 to August 28, velocities are positive northward. (b) Same as (a) but from August 28 to August 31. (c) Scatter plot of current velocity time series against wind velocity between August 28 and 31, 2001. "*r*" is the correlation coefficient. We applied a Butterworth band-pass filter around f_2 = 1.2 10^{-5} Hz, back and forth in order to avoid any phase shift.

3.3 Discussion

3.3.1 Consequence and cause of enhanced turbulence

Consequence: diapycnal mixing Previous studies stated that the hypolimnion is almost turbulence-free offshore and the turbulent mixing is at an order of molecular level (Münnich *et al.*, 1992; MacIntyre *et al.*, 2009a). However MacIntyre *et al.* (2009b) documented strong 2-day averaged turbulent diapycnal diffusivity in the hypolimnion likely generated by shear instabilities due to internal waves in Lake Toolik. Our observed data provide a 48-hour snapshot showing turbulence enhancement in the hypolimnion while internal waves propagate. Depending on the stratification, turbulence may generate enhanced diapycnal diffusivity (Figure 3.20). The amount of turbulent flux is estimated from the eddy

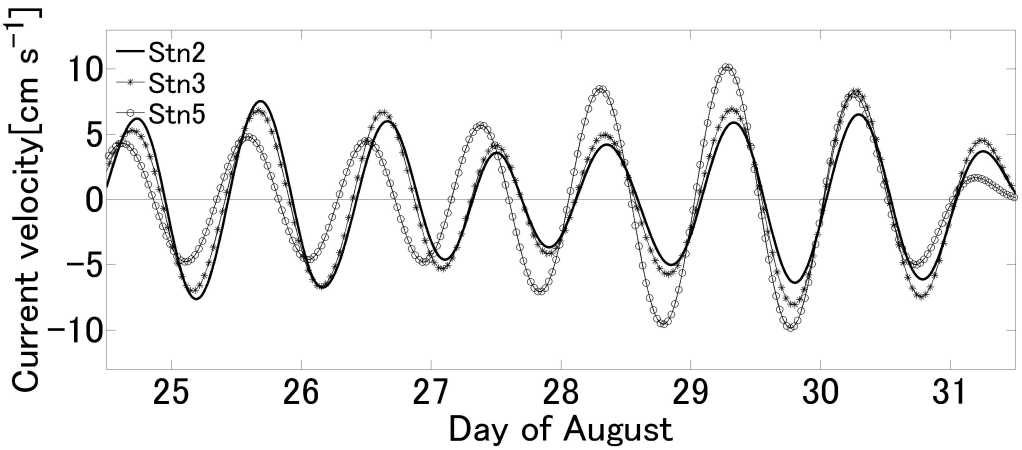

Figure 3.19: 1-day wave current - Comparison of northward currents associated with a 1-day wave at 2 m depth between Station 2, Station 3 and Station 5. Data were computed from a Butterworth band-pass filter around f_2 = 1.2 10^{-5} Hz. The current velocity is in cm s^{-1}.

diffusivity coefficient using the formula:

$$K_\rho \quad = \quad \Gamma \frac{\varepsilon}{N^2} \tag{3.11}$$

where Γ is the mixing efficiency factor and is equal to:

$$\Gamma = \frac{R_f}{1-R_f} \qquad \text{,with} \quad R_f = \frac{1}{1+\frac{\varepsilon}{b}} \tag{3.12}$$

$b = \overline{w'\rho'}g/\rho_0$ being the buoyancy flux, w' the turbulent component of vertical velocity and ε the turbulent kinetic energy dissipation rate. Ivey & Imberger (1991) showed that Γ is variable depending on the processes energizing the turbulence. TurboMAP does not measure w', therefore our dataset did not allow the computation of b, instead I followed Osborn (1980) and used the upper band of the mixing efficency $\Gamma = 0.2$. Wüest & Lorke (2005) 's study shows a remarkable consistency of K_ρ between tracer experiment and microstructure experiment using $\Gamma = 0.2$. According to the data, the eddy diffusivity exceeded the order of 10^{-4} m^2 s^{-1} when the turbulent kinetic energy dissipation rate was on the order of 10^{-7} W kg^{-1} in the hypolimnion (Figure 3.20). In other locations, diffusivity was on the order of 10^{-6} m^2 s^{-1} or smaller ($\sim 10^{-7}$ m^2 s^{-1}), corresponding to a molecular diffusivity level. Above 20 m depth, low values were consistent with strong stratification that suppresses turbulence.

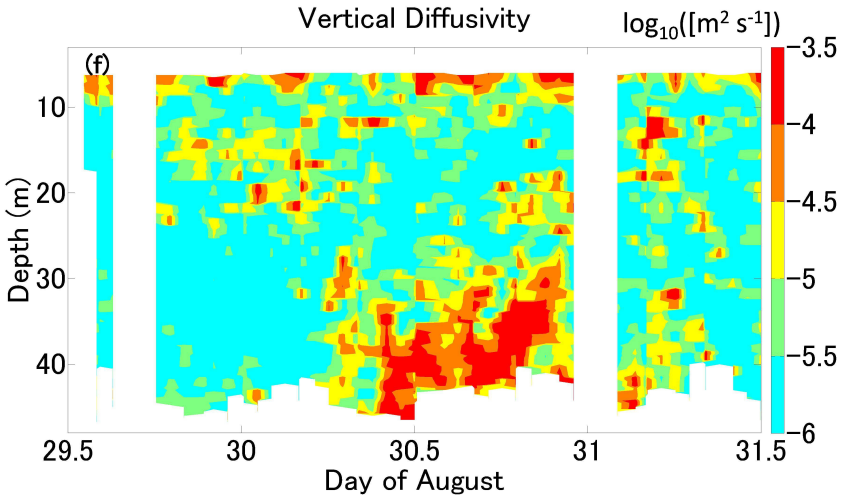

Figure 3.20: Eddy diffusivity - Estimated vertical eddy diffusivity K_ρ (m^2 s^{-1}) distribution in logarithmic scale. Strong values of diffusivity within the hypolimnion can be seen at day 30.5 while two-large-scale internal waves are in phase.

Cause As the turbulence event in hypolimnion occurred only once during the TurboMAP experiment (Figure 3.13), it seems to be associated with a low-frequency phenomenon, likely large-scale internal wave propagation. The enhanced turbulent event occurred when the velocity is weak, seen on day 30.5 (noticeable in Figure 3.15), rather than when the velocity magnitude is at maximum (day 30.2 or day 30.9), thus bottom stress was disregarded as the source. Münnich *et al.* (1992) hypothesized a generation of shear within the hypolimnion when waves are superposed, which in turn enhances turbulence. Therefore, I compare currents associated with the internal Kelvin wave and the inertial wave, and assess the superposition of the two waves. Current data were separated by a Butterworth bandpass filter around those corresponding frequencies that were found in our spectra. Between midnight, August 30, to midnight, August 31, I found currents induced by the two superposed waves are stronger than when waves are taken one by one. For instance, on August 30 at 5:00 am, day 30.2, local time, current speed was 16 cm s^{-1}, which could be a superposition of 12 cm s^{-1} for the inertial wave and 4 cm s^{-1} for the Kelvin wave (Station 2 at 42 meters in Figure 3.21a). This result indicates that the baroclinic Kelvin waves were acting cohesively and enhanced the total velocity field. Large internal waves were out of phase during the first and last 12 hours of the microstructure experiment, resulting in a weaker current.

Velocity shear was computed from current data associated to the two waves at Stn 2 and 3, as these stations are close to the TurboMAP experiment site. At 40 m depth, the

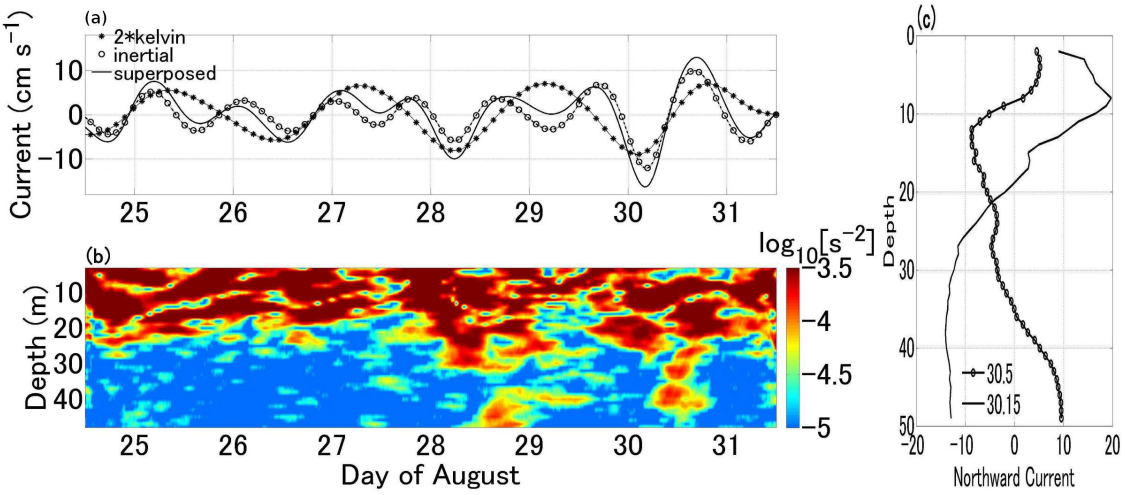

Figure 3.21: Shear distribution and internal waves current - (a) Comparison, at 42 m depth at Station 2, between the two internal waves and their superposition. The black-starred line stands for northward current associated with the Kelvin wave, the circles with the inertial wave and the thick line with the superposition of them (current associated to the Kelvin wave was doubled in order to emphasis the phase). (b) The correspondent shear distribution (s^{-2}) in the water column at Station 2 during the entire ADCP experiment. (c) Profiles of northward current at Station 2 at day 30.15 (black line) and at day 30.5 (black line with circles)

squared values of velocity shear were about 10^{-4} s^{-2} from 06:00 am, August 30 to 06:00 pm, August 30 at Station 2 (Figure 3.21b). The strong shear in the metalimnion region (20 meters depth) can be explained by the characteristics of Vertical Mode 1 internal waves. Horizontal velocities associated with this type of wave have opposite direction above and below the metalimnion, thus generating enhanced shear in this region. Figure 3.21c shows profiles of northward current before and during the enhanced shear event. To examine the effectiveness of enhanced hypolimnetic shear, we computed the gradient Richardson number, *Ri*, that is the ratio between stratification and shear strength:

$$Ri = \frac{N^2}{\left(\frac{\partial U}{\partial z}\right)^2} \tag{3.13}$$

when this parameter is less than 0.25, the strength of shear is enough to induce turbulence. In our observation, the hypolimnetic enhanced shear was strong enough to bring the Richardson number below the critical value a few times (Figure 3.22), but the values varied between 0.2 and 1 in the area of the enhanced turbulence event. Therefore, I could not assert whether shear instability was the trigger of the enhanced turbulence event. Values of *Ri* being low but not as low as the criterion value may be due to the fact that shear data were obtained

from ADCP at Stn 2, located 700 meters away from the TurboMAP experiment location. MacIntyre *et al.* (2009a) and Alford & Pinkel (2000) associated high dissipation to high rate of strain during internal waves event. In looking at 8, 9, 10 °C isotherms in Figure 3.10, high dissipation in the hypolimnion seems correlated to isotherms being pulled apart or squeezed; whereas in weak dissipation period, such a feature of isotherms is not noticeable. These features may suggest strain as a possible cause of the enhanced turbulence in the hypolimnion.

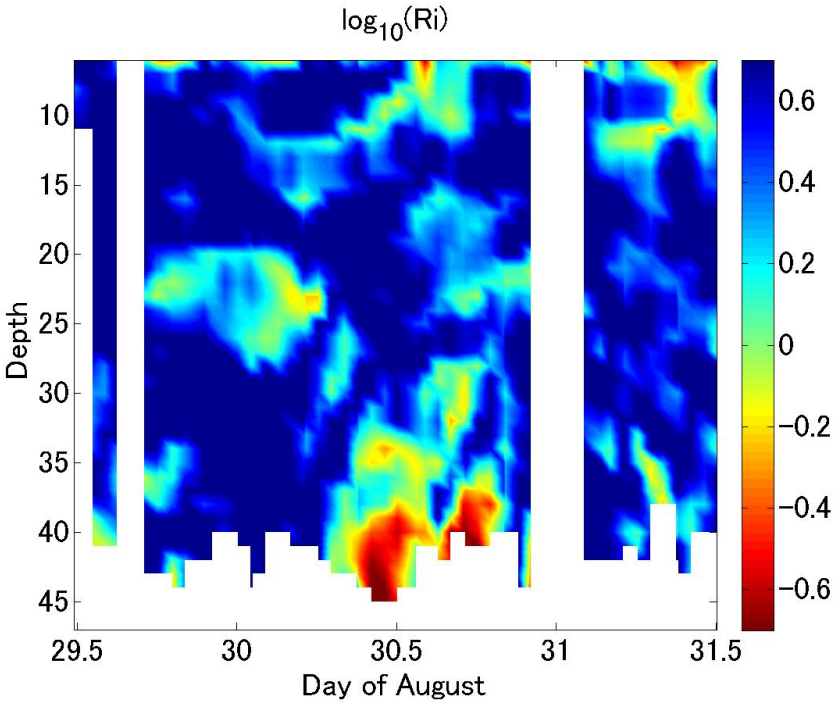

Figure 3.22: Richardson number - Distribution of log10 of Richardson number during the TurboMAP field experiment, corresponding to the presence of high turbulent event in the hypolimnion, $\log(Ri_c) \sim -0.6$

The fact that enhanced shear is correlated with the Kelvin waves being in phase suggests an occurrence of this event every 2 days. Looking at the whole time series from Station 2 (Figure 3.21a), we notice that the two waves were in phase every 2 days, from day 24.9 to 25.3, then from 26.6 to 26.9, from 28 to 28.8 and from 30 to 31. However, hypolimnetic shear enhancement happened above 45 m depth after August 27 (Figure 3.21b), when the internal Kelvin wave was in phase with the wind-energized diel wave (Figure 3.18). This result suggests that the enhanced shear event is dependent on the energy input from the wind and the coupling of the leading internal waves, since current amplitude of the waves superposition is higher at that moment, i.e. days 28 and 30.

3.3.2 Cause of sediment resuspension

High turbidity water appeared in the bio-optical data at the same time as the turbulence event. Sakai *et al.* (2002) indicated a correlation between such a biological event and internal wave propagation in Lake Biwa. However, neither the nature of the wave nor the physical process was specified. This study showed that the water with high turbidity and high fluorescence intensity, likely due to sediment resuspension, is correlated to large-scale internal waves. The enhanced current (day 30.2 on Figure 3.21a) in the water column, caused by two low-frequency waves, resulted in strong bottom stress above the sediment layer (Wüest & Lorke, 2003), leading to sediment resuspension (Figure 3.12) in the bottom boundary layer, which is then brought up to 40 m depth by successive turbulence that occurred at day 30.5 or by the upwelling caused by the internal wave field.

3.4 Conclusion

The study of Lake Biwa in August 2001, showed the generation of two phenomena caused by the superposition of two large-scale internal waves, more precisely, when these two waves were in phase. One phenomenon was sediment resuspension, likely induced by an enhanced bottom stress resulting from stronger current. The other event was enhanced turbulence (10^{-7} W kg^{-1}) within the hypolimnion (40 m depth), correlated to either shear instabilities or enhanced strain field. This turbulence event was associated with strong vertical diffusivity (10^{-4} m^2 s^{-1}). Therefore, our study suggests that the superposition of large-scale internal waves may play a role in the energy redistribution to the small-scales in the hypolimnion, as well as material flux near the bottom of the lake.

Because this study shows a directly observed correlation between large-scale internal waves and enhanced turbulence event within Shiozu Bay, the need to understand how these waves behave within the bay has become apparent. Unfortunately, the data set is not complete enough to clarify the fate of the wave entering into the bay. Some questions remain unanswered in our case, such as: once the wave propagates within the bay, is it completely dissipated, or is it reflected? Thanks to the refining of numerical simulation models with the increase of computational power, studies using such tools have shown great consistency

when compared to observation data. Therefore, using a numerical simulation I will be able to clarify the internal wave dynamics within the bay.

Chapter 4

Low-frequency internal waves in Shiozu Bay, Lake Biwa: A numerical approach.

4.1 Introduction

4.1.1 Background

In the previous chapter, the results have shown that Shiozu Bay may exhibit a different dynamic than the main basin. More precisely, the bay displays a low-frequency internal wave field that induces a turbulent event within the hypolimnion, as well as an internal Kelvin wave entering into the bay. These observed facts lead to the next stage that investigates the fate of basin-scale internal waves within Shiozu Bay. Unfortunately, the data from the campaign do not allow to reach that goal. Thus I employ a numerical model to simulate the situation that occurred in the bay after the typhoon. Thanks to the growing computation power of computers, numerical simulation is becoming more and more attractive to use as a tool to combine with the observed data.

Several studies have been done with the goal of simulating internal waves in large lakes, influenced by periodic wind. These studies have documented consistency between simulated results and observed results. ELCOM (Estuary, Lake and Coastal Ocean Model; Hodges *et al.* (2000)) was used by Shimizu *et al.* (2007) to study Lake Biwa, and Appt *et al.* (2004) applied the same model on Lake Constance. However, most of the studies focused only on

the main basin of the lake. Umlauf & Lemmin (2005) studied flux of water between the main and side basin of Lake Geneva, and concluded a different dynamic from previously thought, but no result on the fate of large-scale internals wave within the basin was documented.

Previous studies have shown that numerical simulations can provide a realistic picture of what is happening or happened during internal waves event. In order to understand the dynamic inside the bay, I have employed a recently developped numerical code, SUNTANS (Fringer *et al.*, 2006). SUNTANS stands for Stanford Unstructured Non-hydrostatic Terrain-following Adaptive Navier-Stokes Simulator. This C-coded simulator possesses three important features: unstructured grid, non-hydrostatic approximation and parallel-computing ability. At the time of this research, SUNTANS is the only simulator that provides these three features. Zhang *et al.* (2011) simulated the generation and the propagation of non linear internal waves in the South China Sea by using SUNTANS, and accurately reproduced its arrival time.

The parallel computing allows the user to split the computation among several processors for for the whole computation, enabling the computation time to decrease significantly. SUNTANS uses the message-passing interface (MPI) library to communicate with each processor. Moreover the ParMetis (Karypis & Kumar, 1996) package is used to even out the working load on each processor. Fringer *et al.* (2006) compares the processing time of two scenarios: in using a single processor and in using 2-4-8-16-32 processors. Unsurprinsigly, the parallel computation was much faster than monoprocessor case. For example using 8 processors, the simulation time was seven times shorter.

Auger *et al.* (2013) documents that at the mouth of Shiozu Bay in Lake Biwa, the velocity field associated with a V1H1 mode Kelvin is consistent with the wave entering the bay as well as the presence of other low frequency waves visible in the observed temperature data. Moreover Okamoto & Endoh (1995) observed 48 hours oscillations in Shiozu Bay, and mentioned that these oscillations were excited by the Kelvin wave from the main basin. But their data did not show the wave going out of the bay. In addition, Auger *et al.* (2013) observed an intense turbulence event within the hypolimnion that appears to be linked to the low frequency internal wave field. However whether the waves dissipated within the bay remains unclear.

MacIntyre *et al.* (2009a) documented that low-frequency internal waves may contribute to the energy redistribution to turbulence directly, in opposition to the convention of energy redistribution toward high-frequency waves. The observations made by Auger *et al.* (2013) of enhanced turbulence within the water column and of a portion of the main Kelvin wave entering into the bay without hints of reflection may suggest a complete dissipation. Such direct dissipation of internal wave energy to small scale would generate intense turbulence events within the bay and would impact the distribution of bio-materials.

The goal of this chapter is to understand the fate of the basin-scale internal wave field within Shiozu Bay. However the issue of using regular model is the grid, more precisely the type of grid cell that constitutes the grid. A conventional grid is composed of square "cells", whereas the unstructured grid in SUNTANS is composed of triangles. In Shiozu Bay, the shoreline may affect the internal waves because of the size of the bay compared to the wavelength of the basin-scale internal waves. Therefore in using the unstructured cells, the shoreline will be better resolved by using triangle-shaped cells (Figure 4.1) than by using the conventional rectangular grid cell. Matching the shoreline closely with a structured grid would require an increase in resolution (decrease in cell size) and thus an increase in computation and in simulation time. The main advantage of an unstructured grid is the accuracy at which irregular shoreline is resolved (when bays and islands are included for instance). In addition it allows an increase in resolution where dynamics with different scales are interacting with each other (Fringer *et al.*, 2006; Pain *et al.*, 2005). The change of resolution for a specific location where computational resources need to be focused increases the computational efficiency.

When we look at oceanic scales, numerical simulations are made by assuming the hydrostasy of the pressure, thus by neglecting the total derivation of the vertical velocity. Say we can divide the total pressure as $p = p_h + q$ where p_h is the hydrostatic component and q the nonhydrostatic component of the pressure. The momentum equation on the vertical axis can be written as:

$$\rho_{ref}\frac{\mathrm{D}w}{\mathrm{D}t} = -\frac{\partial(p_h+q)}{\partial z} - g\rho \tag{4.1}$$

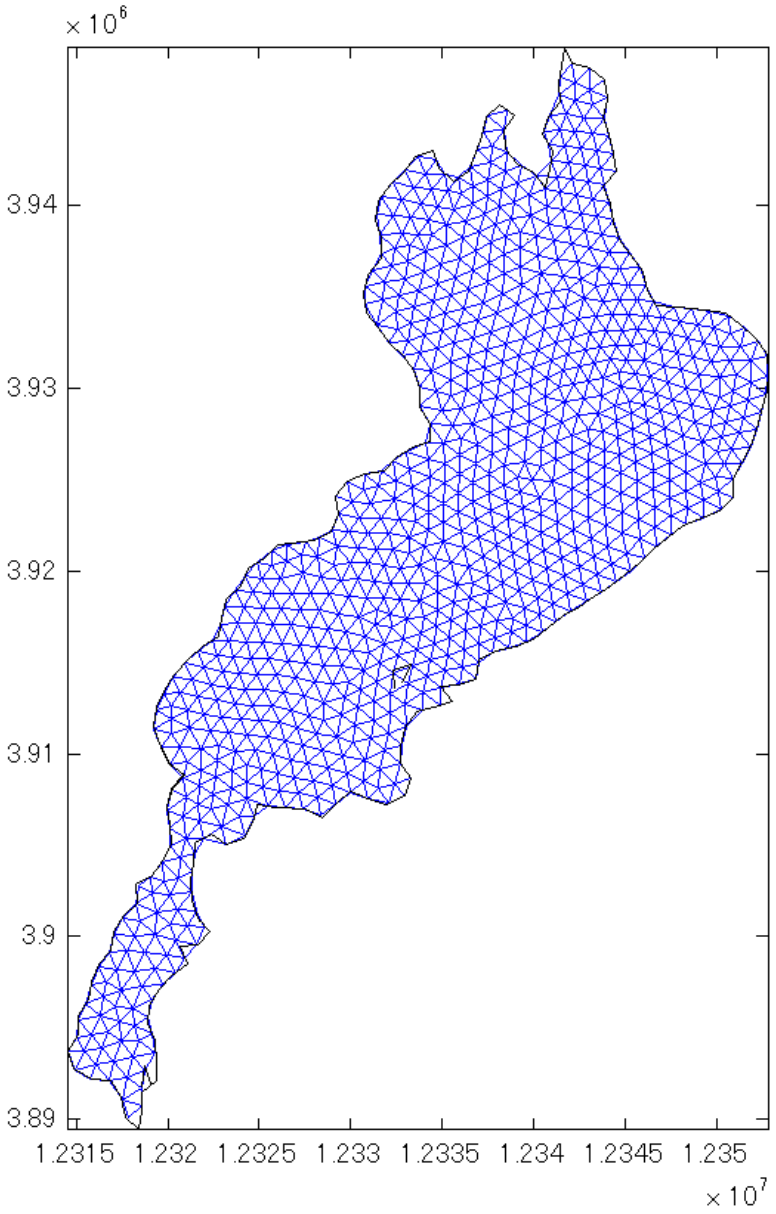

Figure 4.1: Unstructured grid - An example of an unstructured grid (*blue triangles*), representing Lake Biwa, and the coastline used to generate the grid is overlaid in thin black line.

in following the Boussinesq approximation with $\rho = \rho_{ref} + \rho_0(z) + \delta\rho(x,y,z,t)$ and

$$\frac{\mathrm{D}}{\mathrm{D}t} = \frac{\partial}{\partial t} + \mathbf{u}\cdot\nabla \tag{4.2}$$

In the hydrostastic assumption, the vertical gradient of pressure compensates the buoyancy, hence the assumption leads to $\partial P_h/\partial z = -g\rho$, and then equation 4.1 becomes:

$$\rho_{ref}\frac{\mathrm{D}w}{\mathrm{D}t} = -\frac{\partial(q)}{\partial z} \tag{4.3}$$

Therefore, neglecting the nonhydrostatic component of pressure is equivalent to supposing the total derivation of the vertical velocity is greatly inferior to $g\rho$, this is the hydrostatic assumption. Despite this assumption, ocean dynamics are well simulated. It is possible because these studies were focusing on scales larger than 10 km. However, in this study we focus on scales smaller than 10 km, since Shiozu Bay's characteristic length is about 8 km. Moreover, Bergh & Bernsten (2009), argue that between scales of 1 km and 10 km the hydrostatic approximation starts to break down, and there is a range of grid sizes between 1 meter and 1 kilometer where non-hydrostatic pressure effects may be important, even though they are not fully accounted for.

de la Fuente *et al.* (2008) describe the effect of weakly nonlinear and nonhydrostatic accelerations in a rotating stratified circular lake. They show that basin-scale internal waves may steepen due to nonlinearity , whereas nonhydrostasy acts against this steepening. When these two effects are balancing each other, solitary-type waves may be generated. They also highlight that with the inclusion of these two effects, Kelvin type waves quickly lose their energy to subazimuthal modes and solitary-type waves. This statement underlines the need to include the nonhydrostatic effects in the simulations since my study deals with features at a scale of about a kilometer.

4.1.2 SUNTANS

As mentioned earlier, SUNTANS uses an unstructured finite-volume grid, more precisely triangle-shaped cells on the horizontal plane and structured on the vertical axis (z-level grid).

It computes the three dimensional non-hydrostatic equations by storing velocity components at the faces of the cell, whereas all other variables, such as temperature or salinity, are stored at the barycenter of the cell (Voronoi point), see Figure 4.2 left panel. On the right panel a cell with its neighboring cells are displayed. The empty circles are called the Delaunay points, and we notice that cells have several of these points in common with neighboring cells. The black cross at the center of each cell represents the Voronoi points, which may be seen as the barycenter of the cells. The use of structured z-level on the vertical axis was chosen to make the access of memory more efficient, since water columns can be placed side by side. Moreover a z-level grid, used in SUNTANS, avoids pressure gradient errors that are generated when employing structured sigma-level used in ROMS (Regional Ocean Model System, Song & Haidvogel (1994)). In SUNTANS, the horizontal discretization follows a semi-implicit theta method to avoid instability caused by rapid surface waves.

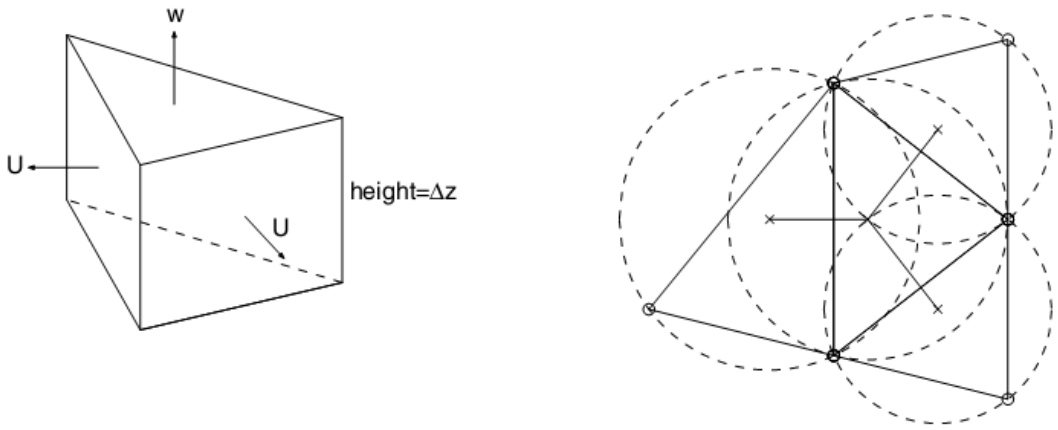

Figure 4.2: Cell from an unstructured grid - This sketch is a representation of a cell in the unstructured grid used in SUNTANS, after Fringer *et al.* (2006)

SUNTANS solves the three-dimensional Navier-Sotckes equations under the Boussinesq approximation and employs an eddy diffusivity model (when the Reynolds tensor is modeled as $\tau_{ij} = \nu_t \left\langle \frac{\partial u_i}{\partial x_j} + \frac{\partial u_j}{\partial x_i} \right\rangle$, where ν_t is the eddy diffusivity). The main equations can be written as follow:

$$\frac{\partial u}{\partial t} + \nabla.(\mathbf{u}u) - fv + bw = -\frac{1}{\rho_0}\frac{\partial P}{\partial x} + \nabla.(\nu_H \nabla_H u) + \frac{\partial}{\partial z}(\nu_V \frac{\partial u}{\partial z}) \tag{4.4}$$

$$\frac{\partial v}{\partial t} + \nabla.(\mathbf{u}v) + fu = -\frac{1}{\rho_0}\frac{\partial P}{\partial y} + \nabla.(\nu_H \nabla_H v) + \frac{\partial}{\partial z}(\nu_V \frac{\partial v}{\partial z}) \tag{4.5}$$

$$\frac{\partial w}{\partial t} + \nabla.(\mathbf{u}w) - bu = -\frac{1}{\rho_0}\frac{\partial P}{\partial z} + \nabla.(\nu_H \nabla_H w) + \frac{\partial}{\partial z}(\nu_V \frac{\partial w}{\partial z}) - \frac{g}{\rho_0}(\rho + \rho_0) \tag{4.6}$$

accompanied with the incompressibility constraint where $\nabla.\mathbf{u} = 0$ and b the vertical component of the Coriolis force.

The simulator incorporates a closure model to compute the eddy viscosity (turbulent vertical transfer of momentum) and eddy diffusivity (turbulent vertical transfer of scalar). SUNTANS uses the popular turbulence closure model Mellor-Yamada (MY2.5 hereinafter) (Mellor & Yamada, 1982). Both parameters are computed with two equations to estimate the turbulent kinetic energy q^2 and the turbulent kinetic energy times a turbulence scale $q^2 l$, and a stability function.

SUNTANS computes the non-hydrostatic pressure based on Casulli (1999) by splitting the total pressure into an hydrostatic and a non-hydrostatic component, $p = p_h + q$ where q is the non-hydrostatic component. First the hydrostatic component is computed, then the total pressure is computed by updating the pressure with the non-hydrostatic component with the use of a Poisson equation. Solution of the pressure-Poisson equation is the most computationally demanding part of the procedure. In SUNTANS it is solved by employing the preconditioned conjugate gradient algorithm with the block-Jacobi preconditioner (Marshall *et al.*, 1997a).

When using a standard personal computer that can be found on the market, the high cost in computing time would not be much of an issue in a small domain. However in a large-scale simulation as we will see in this research, the generation and propagation of large scale internal waves in Lake Biwa, it would be an issue. Thus, the parallel computing plays an important role in this case by greatly reducing the computation time for the same run, for this study, a 16-processors server is used. The difference in computation time between a 1 processor case and a 16 processors case is such that for a 3 months long event simulation it took 1 week when using 1 processor and 5 hours with 16 processors.

Through this chapter, I will investigate the dynamic of the internal wave field that occurs within Shiozu Bay by making use of the numerical simulator SUNTANS. Two grids were generated: a coarse grid and a fine-scale grid aimed at doing a nesting. First, this research will deal with the computation of the initial and boundary conditions for the coarse grid.

Then the simulated results will be compared with observed data and the consistency of the simulation will be assessed. In the second part of this chapter, I will study the results obtained from the fine-scale grid, compare them with observed results in the bay, and investigate the fate of the internal Kelvin wave within the bay. In addition, an explanation of an enhanced turbulence event within the hypolimnion is considered.

4.2 Method

4.2.1 Generation of initial conditions

Originally, SUNTANS does not contain routines that compute wind stress and heat fluxes, so we have to write and implement the routines allowing these computations. Thus the first section of this chapter describes the calibration of the developed code using the coarse grid case. Data computed from the coarse grid case will be used as the initial condition for the finer scale grid, which is a method known as ”nesting”.

Figure 4.1 shows the grid and the cells at the surface layer, and Figure 4.2 alludes to the z-level discretization on the vertical axis. The bathymetry is displayed in Figure 4.3, with the shape of cells. The colorbar is the depth at each cell in meter and shows that the deepest point of the grid is about 93 meters in the Northern Basin and 50 meters within Shiozu Bay. In a rectangular grid, the resolution, usually taken constant all over the grid, is represented as the distance between the barycenter of a cell to the neighboring one. In the case of the SUNTANS grid, the resolution may be identified as the distance between Voronoi points, which may be seen as the barycenter of the triangle (see Figure 4.2). For every Voronoi distance, there is a common edge between two neighboring cells. Thus, I can compute the grid resolution as the number of edges per range of Voronoi distance. In the right bottom corner of Figure 4.3 the resolution is shown as a histogram. I can infer there is no fixed resolution for this type of grid. However I notice from the Voronoi distance histogram that most of the Voronoi distances remain within the range of 400-700 meters. Moreover, the grid contains 1350 cells at the surface layer, and the resolution in the vertical axis is constant and is equal to $\Delta z = 0.93$.

To investigate the propagation of internal waves in Lake Biwa and further their fate within

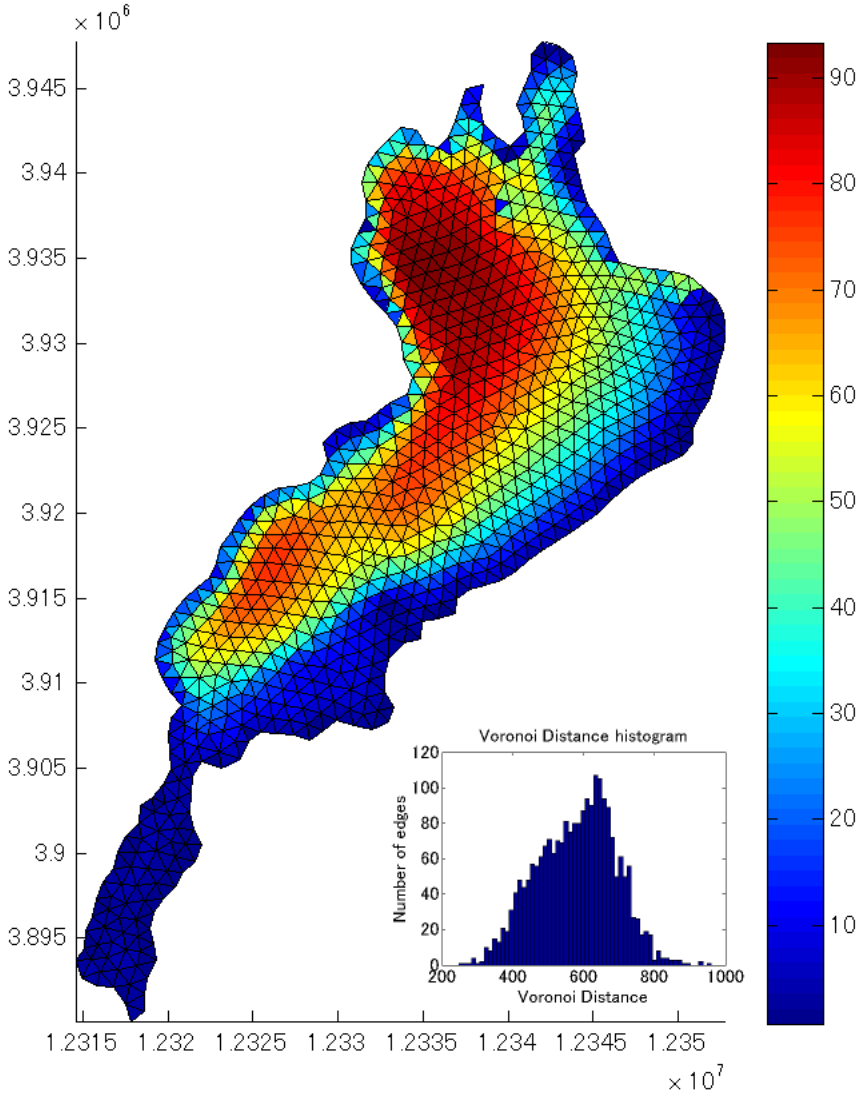

Figure 4.3: Coarse grid bathymetry - A representation of the bathymetry used in the coarse grid case as well as the Voronoi distance associated with this grid (histogram). The colorscale is the depth in meters.

Shiozu Bay, I must pay attention to the temperature field. Indeed, as one can see in equation 2.9 and 2.10, the period of basin-scale internal waves depends on the stratification. Unfortunatly, the temperature field obtained from the instruments was issued more than one week after the typhoon.

The Lake Biwa Research Institute (LBERI) carries out regular monitoring of Lake Biwa by using F-probe (figure 3.5) twice a month at few locations, and they publish data profiles, such as profiles of dissolved oxygen and temperature, on their website. Keeping in mind the lack of temperature data before the typhoon, I based the temperature initial condition on temperature profiles from the monitoring data. Also the nonhydrostatic effect magnitude in using the coarse grid is still unclear because the resolution of this grid is fairly lower than the scale range of hydrostasy breakdown. To know if the nonhydrostatic component is significant, the simulation will be run for a large time period of several months. With this method, even though the non-hydrostatic effect is small, a long time run would emphasize the effects in accumulating them and the difference between hydrostatic and nonhydrostatic cases would become significant.

In order to investigate the difference between the two cases, January 16 2001 was chosen as a starting point. I took into account the need for a long time range for the simulation, and on that day, the lake was entirely mixed, meaning that the intitial condition would match the reality. Profiles of temperature and dissolved oxygen on January 15 and 16 were obtained from the LBERI website, and are shown in Figure 4.4. Two temperature profiles were measured on January 16 in the Northern Basin and surface temperature was taken in the Sourthern Basin on January 15. The locations of these profiles are shown as yellow circles in the right panel of figure 4.4. According to the profiles of temperature and dissolved oxygen, the Northern Basin was completely mixed on January 16 12:00. Even though the temperature in the Southern Basin was taken on January 15 12:00, I assumed that the temperature in the Southern Basin was the same on January 16.

To obtain the initial condition of the temperature field, each temperature profile was averaged vertically and then the temperature was interpolated horizontally. The interpolation was made by computing an objective analysis of the temperature, taken from *ROMS tools*

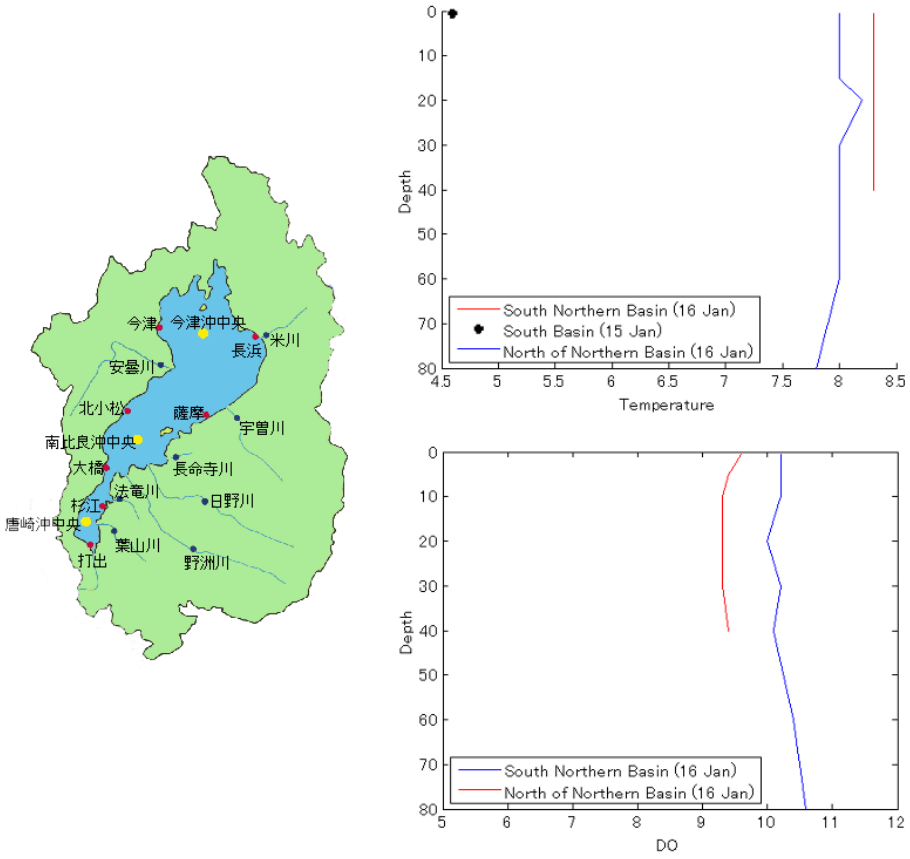

Figure 4.4: Temperature and DO on 2001 January 16 - Location and profiles issued from LBERI monitoring in Lake Biwa on Jan 15 and 16. Yellow circles represent the profile locations, top right panel depicts the temperature profiles and bottom right shows the dissolved oxygen profiles

library. It consisted of

$$T_e(x,y) = \overline{T_N} + \sum_{i=1}^{N} W_i(x_e,y_e,x_i,y_i) \times T_i' \tag{4.7}$$

where $\overline{T_N}$ is the average temperature between the N stations, T_i' the temperature fluctuation of a profile location i being $T_i' = T_i - \overline{T_N}$, and $W_i(x_e,y_e,x_i,y_i) = \mathbf{R_2}/\mathbf{R_1}$ being a weight function depending on the distance between stations ($\mathbf{R_1}$), as well as the distance between stations and extrapolated points ($\mathbf{R_2}$), with:

$$\mathbf{R_1}(i,j) = e^{-d_{ji}a} \quad ,i,j = 1\ldots N \tag{4.8}$$

$$\mathbf{R_2}(1,j) = e^{-d_{ei}a} \quad ,i = 1\ldots N \tag{4.9}$$

where d_{ji} is the distance between location i and j, d_{ei} is the distance between the extrapolated point and the station i, and a is the inverse of an uncorrelation coefficient with a unit of m^{-1} taken to be 1/20000. The choice of the parameter a was made by taking the ratio of the length of Lake Biwa over the number of point ($\frac{60\ \mathrm{km}}{3}$) and inversing the ratio. Because the lake was vertically mixed on January 16 12:00, the temperature was assumed to be identical vertically at each cell. Thus, the temperature field is initialized as shown in Figure 4.5 at each z-level.

4.2.2 Boundary conditions

In order to carry out the simulation from January 16^{th} to the beginning of September, I must use two types of data sets: wind time series in order to mimic the typhoon and weather data to reproduce the stratification at the time of the typhoon (air temperature, cloudiness, relative humidity, short wave radiation,). These two datasets were obtained from the meteorological stations network from the Japanese Meteorological Agency. Around Lake Biwa, five stations recorded wind velocity and direction: from southernmost and clockwise, Otsu, Minami-komatsu, Imazu, Nagahama, and Hikone. Also, the meteorological station in Hikone measured air parameters such as vapor pressure, shortwave radiation. Equations for boundary conditions involving heat fluxes and wind forcing are documented in the litterature (Berliand

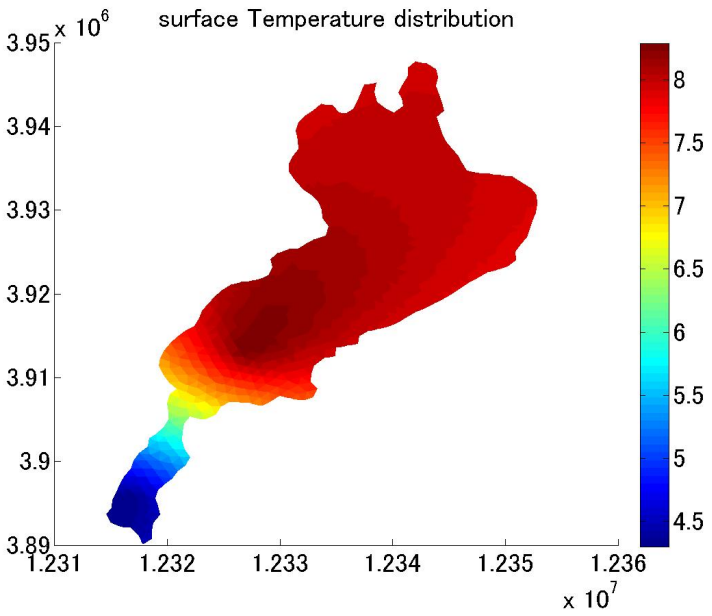

Figure 4.5: Initial temperature field - A representation of the temperature distribution at the surface layer that was extrapolated from the LBERI dataset. The colorbar is temperature scale from 4.4 °C to 8.3 °C.

& Berliand, 1952). The following section describes the incorporation of the surface conditions in SUNTANS.

Heat fluxes Heat fluxes allow heating and cooling of the water, and finally the generation of stratification, the main condition for the presence of internal waves. Atmospheric parameters were measured only at the JMA station located in Hikone City. Therefore, in the simulation I assumed that meteorological data remain the same throughout the lake. Because the size of Lake Biwa is small compared to the scale of meteorological event, the assumption of identical atmospheric variables all around the lake, such as shortwave radiation, may be reasonable.

Heat fluxes are categorized into four types: short-wave radiation (S_w hereinafter), sensible heat flux (H_S hereinafter), long-wave radiation (L_w hereinafter) and latent heat flux (H_l hereinafter). The equation of temperature changes at the surface layer is expressed as follows:

$$\frac{\partial T_{top}}{\partial t} = \frac{1}{C_p \rho \Delta z} \Delta Q \tag{4.10}$$

where $Q = S_w + L_w + H_s + H_l$ is the total heat flux, C_p the specific heat of water and ρ the density of the water.

Following Berliand & Berliand (1952) and Gill (1982), I employed the following equation for computing the long wave radiation (L_w):

$$L_w = -E\sigma T_a^4(0.39 - 0.05\sqrt{e_a})(1 - 0.8 * F_{cloud}) - 4E\sigma T_a^3(T_w - T_a) \tag{4.11}$$

where E is the long-wave emissivity, 0.985, σ represents the Stefan-Boltzmann constant, 5.67×10^{-8} m^{2}K^{-1}, T_a air temperature and T_w temperature at water surface, both being in Kelvin. F_{cloud} is a dimensionless parameter describing the cloudiness and equals 0 when the sky is clear, and e_a is the vapor pressure. Sensible heat flux is estimated from the following equation:

$$H_s = \rho_a C_{pa} C_h U_0 (T_a - T_w) \tag{4.12}$$

where air density is ρ_a, the specific heat of air C_{pa}, a transfer coefficient C_h, wind velocity above the surface U_0 and temperature difference between air and water ($T_a - T_w$). Latent heat flux is given as follows:

$$H_l = \rho_a L_e C_e U_0 (q_a - q_w) \tag{4.13}$$

where air density is ρ_a, the latent heat of evaporation L_e, a transfer coefficient C_e and wind velocity above the surface U_0 and difference of specific humidity of atmosphere (q_a) and water surface (q_w). The specific humidity parameters are give as follows:

$$q_s = \frac{0.62198 e_s}{P_a - 0.377 e_s} \tag{4.14}$$

$$q_a = \frac{0.62198 e_a}{P_a - 0.377 e_a} \tag{4.15}$$

The previous three heat fluxes are concentrated in the surface layer, whereas S_w penetrates into the water column. The penetrating depth depends on the water type of the lake. The water type depends on how turbid the water is. The less the turbidity, the deeper the short wave radiation reaches. As the short wave radiation deepens, it provides thermal energy to heat up the neighboring water. Therefore the intensity of the radiation decreases with depth.

The visible light penetration is expressed sa follows:

$$I(z) = I_0 (Re^{-z/k_1} + (1-R)e^{-z/k_2}) \tag{4.16}$$

where $I_0 = (1-\alpha)I_{meas}$ is the initial intensity after removing reflected radiation by the water surface ($\alpha \sim 0.05$), z the depth and R, k_1, k_2 are parameters depending on the water type. The first exponential term characterizes the rapid attenuation within the upper 5 meters due to the absorption of the red end of the spectrum whereas the second exponential term repsents the absorption of the blue-green light below 10 m, so $k_2 > k_1$. Jerlov (1968) distinguished oceanic water types and coastal water types. As I am dealing with a lake, we have to chose the water type from among the coastal water types.

Coastal water can be split into nine water types. A water type 1 is a very clear water, while a water type 9 will be a mudy water, with the shortwave radiation heating up the first few meters of the water column. Because the water in Lake Biwa was observed to be neither clear nor brown-colored, the medium water type (type 5) was taken. The parameters are usually computed from the data set published in Jerlov (1968); however only 5 points were available in the profile, making the estimated parameters statistically irrelevant. Zaneveld *et al.* (1981) expressed the decrease of short wave radiation intensity as:

$$I(z) = I_0 e^{-zK_1}(1 - K_2 \tan^{-1}(K_3 z)) \tag{4.17}$$

and $K_1 = 0.3541 \times 10^{-2}$ cm^{-1}, $K_2 = 0.4626$, $K_3 = 3.6806 \times 10^{-2}$ cm^{-1} for a coastal water type 5.

A module to compute the $S_w(z)$ was already integrated in SUNTANS using the equation 4.16 and an algorithm for the vertical conservation of intensity. An issue that may appear in a numerical simulation is that the short wave radiation may be missing if the water column is too shallow to allow the radiation to dissipate completly. Therefore, equation 4.17 was approximated with equation 4.16 to extract R, k_1 and k_2. As mentioned earlier, the first exponential term of equation 4.16 is the rapid decrease of intensity in the first few meters, meaning to below ten meters the second exponential term is dominant. Thus $I(z) = (1 - R)e^{-z/k_2}$ below 10 meters, and I use a least-mean square fit to estimate R and k_2. When

focusing on the first few meters in the water column and by using the previously estimated R and k_2, I apply another least-mean square fit to estimate k_1. Figure 4.6 shows the data from Jerlov (1968), the curve computed from equation 4.17 and the estimation of 4.16 based on 4.17.

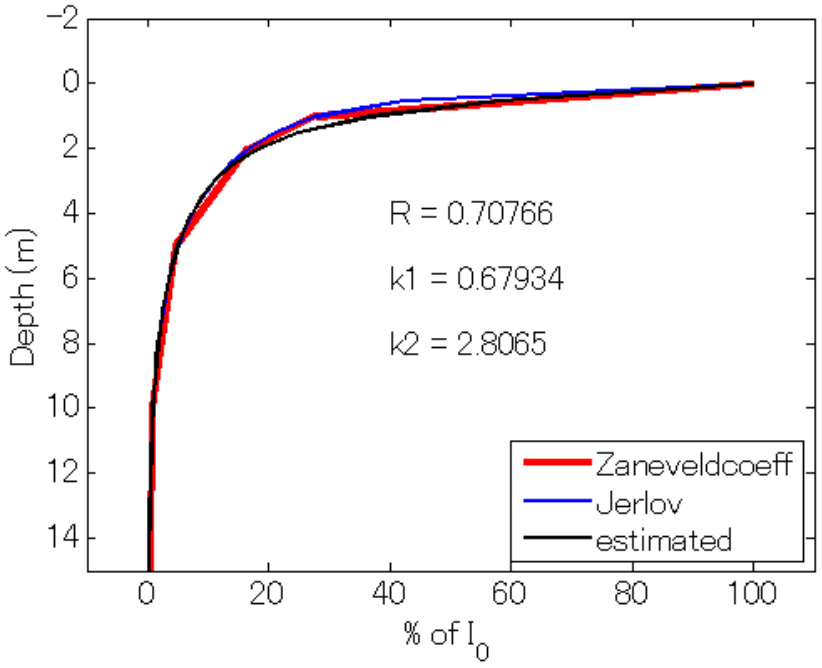

Figure 4.6: Shortwave radiation - Profile of short wave radiation intensity following observed data from Jerlov, analytical expression by Zaneveld *et al.* (1981), and estimated coefficient

Usually, heat fluxes are input as a single parameter, say $\frac{\partial T}{\partial t} = Q$, depending on the water surface temperature. Because SUNTANS solves the system of equations using tridiagonal matrix inversion, heat sources have to be linearized and split into two parameters A and B such that $Q(T_w) = A(T_w) + B(T_w)T_w$ where T_w is the water surface temperature. Heat fluxes parameters are rearranged in order to respect the solving methodology. $A(T_w)$ and $B(T_w)$ expressed as:

$$A(T_w) = Q(T_w) - \left.\frac{\partial Q(T)}{\partial T}\right|_{T=T_w} T_w \tag{4.18}$$

$$B(T_w) = \left.\frac{\partial Q(T)}{\partial T}\right|_{T=T_w} \tag{4.19}$$

Therefore, for each non-penetrative heat flux, I have to compute the parameters A and B. The decomposition of heat fluxes expressed as a linear equation between air and water surface temperature will be quite straightforward (H_s and L_w). The parameters of the long wave

radiation are expressed as follow:

$$B_{Lw} = -4E\sigma T_{aK}^3 \tag{4.20}$$

$$A_{Lw} = 4E\sigma T_{aK}^3 T_a - E\sigma T_{aK}^4 (0.39 - 0.05\sqrt{e_a})(1 - 0.8F_c) \tag{4.21}$$

where T_{aK} is the air temperature in °K. The parameters of the sensible heat flux are expressed as follows:

$$B_{Hs} = -\rho_a C_{pa} C_h U_0 \tag{4.22}$$

$$A_{Hs} = \rho_a C_{pa} C_h U_0 T_a \tag{4.23}$$

By using the equations linked to the latent heat flux, presented previously, the parameters A_{Hl} and B_{Hl} are expressed as follows:

$$B_{Hl} = -0.62198 \frac{\rho_a L_e C_e U_0}{P_a - 0.377 e_s} \frac{\partial e_s}{\partial T} \left(1 + \frac{0.377 e_s}{P_a - 0.377 e_s}\right) \tag{4.24}$$

$$A_{Hl} = H_l(T_w) - B_{Hl} T_w \tag{4.25}$$

Wind stress The other surface boundary condition that has to be specified is the wind stress. Five meteorological stations are spread out around Lake Biwa. They are included within the AMEDAS network, providing wind velocity and direction data hourly. Figure 4.7 displays the wind time series, showing each component of wind velocity, at each meteorological station around Lake Biwa. These timeseries cover day 19 to 31 of August 2001, including the typhoon period (August 21 to 23) and a diurnal wind after August 27. By comparing the wind velocity time series in Figure 4.7, I infer a great variation in the wind field over Lake Biwa. For instance, the intensity of the wind speed during the typhoon period (August 21 to 23) are quite high at Hikone City, about 8 m s^{-1}, (third panel from the top) whereas at Nagahama City (first panel from the top) wind speed during the typhoon did not reach 3 m s^{-1}.

Because the wind field appears to vary significantly over the lake, an objective interpolation was applied thanks to the five meteorological stations to get the wind field over the whole lake. The interpolation was made by using equation 4.7, except that there were more

stations and each components of the wind velocity (northward and eastward) were interpolated separately. Because 4 stations can split the major axis of the lake, the coeffiecient a in Eq. 4.7 becomes $a = \frac{4}{60000}$. Figure 4.8 displays two samples of the interpolated wind field based on data from the five stations. These two samples represent the wind field during the typhoon, and they exhibit the large variation of the wind field over Lake Biwa. At day 21.833 the wind direction clearly shows two patterns; in the north part of Lake Biwa the wind was northward, whereas in the rest of the lake, the wind was southwestward.

During the field experiment in August 2001 in Lake Biwa, the boat was equipped with an ANDERAAS station. Therefore measured and extrapolated wind velocity data at the same location could be compared. As seen in the left panel of Figure 4.9, the interpolated wind velocity is underestimated compared to the observed wind. By computing a linear regression between the interpolated wind and the observed wind (Figure 4.9), I extract a correction factor: 3.2. In order to correct the interpolated wind speed data , we follow Shimizu *et al.* (2007) and multiply the interpolated wind speed from the land-based stations by 3.2. The right panel of Figure 4.9 shows the direction of the observed wind against the simulated wind. The scatter plot highlights the discrepancy between observed wind direction on the boat and the simulated wind direction at the same point for weak wind velocity (taken inferior to 3 m s^{-1}). However during strong wind events (speed superior to 3 m s^{-1}) the direction seems to be similar. Lake Biwa is surrounded by mounts, so the wind field is likely to be extremely modified by the orography.

Even though the extrapolated data show a different pattern from observed data, wind stress was implemented in SUNTANS after the extrapolation and the correction as:

$$\tau = \rho_{air} C_d |U_{10}| \mathbf{U}_{10} \tag{4.26}$$

where τ is the wind stress, ρ_{air} is the densitry of air, C_d the drag coefficient, and $\mathbf{U}_{10}$ the wind velocity at 10 meters height.

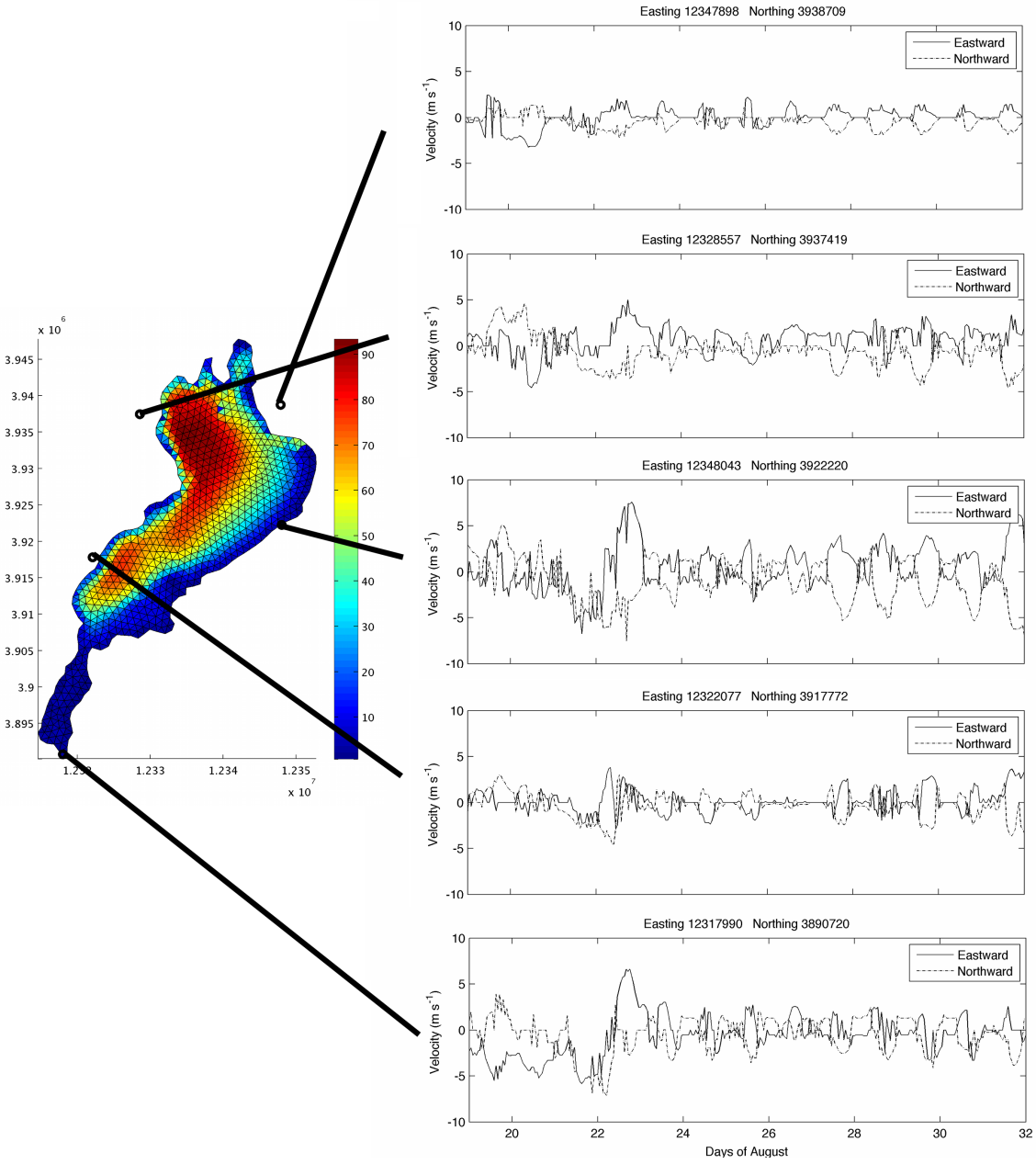

Figure 4.7: AMEDAS stations - Locations of AMEDAS stations around Lake Biwa. The panels on the right display the two components of the wind velocity at 10 meters high. Eastward component is displayed with a *black line* and northward component with a *dash-dotted line*. The time series cover the period August 19 to 31 during the year 2001 with the typhoon period. Stations are, from top right and clockwise, Nagahama, Hikone, Otsu, Minami-Komatsu, Imazu.

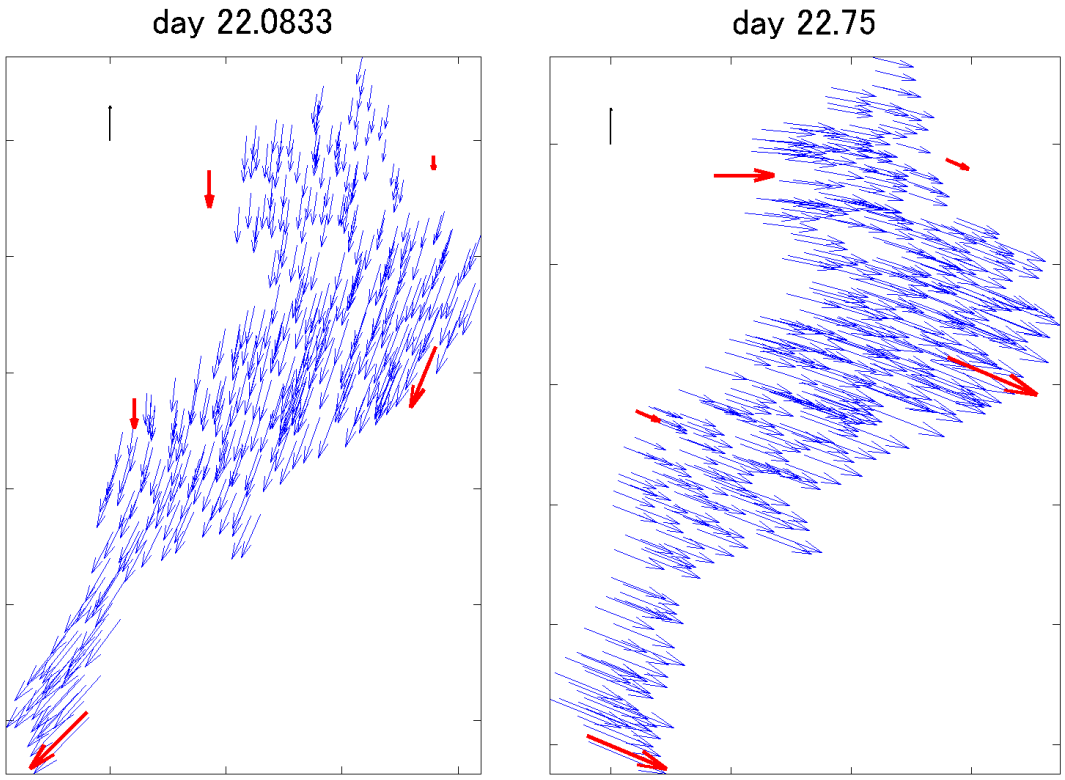

Figure 4.8: Interpolated wind field - Extrapolated wind field (*blue arrows*) all around Lake Biwa. Overlaid with *red arrows* are measured wind from AMEDAS meteorological stations. Stations are, from top right and clockwise, Nagahama, Hikone, Otsu, Minami-Komatsu, Imazu. The *black arrow* stands for a scale of northward wind velocity at 3 ms^{-1}

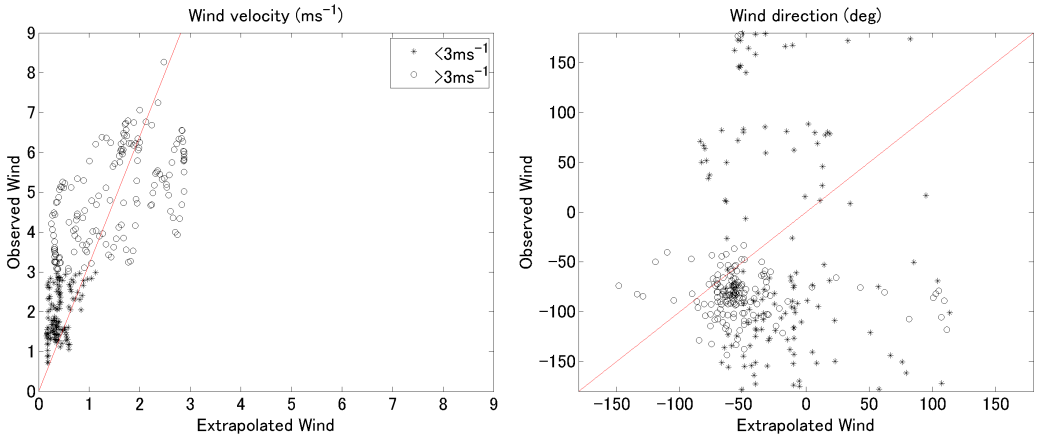

Figure 4.9: Extrapolated vs observed wind velocity - Left panel: a comparison of the extrapolated and observed wind velocity in m s^{-1}, and the curve y=3.2*x, where *empty circles* stands for observed velocity higher than 3 ms^{-1} and *black stars* lower than 3 ms^{-1}. The right panel displays the wind direction in degrees as extrapolated wind as abscissa and observed wind as ordinate.

4.3 Results

4.3.1 Results of the coarse grid

Once the initial temperature field, as well as the surface boundary conditions (heat fluxes and wind forcing) are specified, I can run the simulation. Since the initial current velocity field is unknown, I have to assume that the medium is at rest at the initial step. In order to avoid making the simulation unstable, I have to specify a time step using the Courant number criterion. According to the user-guide provided with SUNTANS, we have to chose Δt such as:

$$\Delta t < C \min\left[\frac{\min(D_g)}{\max(|U|)}, \frac{\min(\Delta z)}{\max(|w|)}, \frac{\min(D_g)}{\max(c_i)}, \frac{1}{2}\frac{\min(D_g)^2}{\max(\kappa_{sH})}, \frac{1}{2}\frac{\min(D_g)^2}{\max(\kappa_{TH})}, \frac{1}{2}\frac{\min(D_g)^2}{\max(\nu_H)}\right] \tag{4.27}$$

where c_i is the internal wave speed, C is the relevant Courant number, D_g is the minimum Voronoi distance, $|U|$ is the absolute value of horizontal velocity, w the vertical velocity, κ_{sH} the horizontal diffusivity for salt, κ_{TH} the horizontal diffusivity for temperature and ν_H is the horizontal turbulent viscosity. After computation, $\Delta t = 30$ s was a good candidate for the simulation. In order to run the simulation from January 16 to September 3, the computor has to run 662400 time steps. Using the 16 multiprocessor computer, the simulation took about 10 hours in walk clock time. Because of small duration, I could run the simulation with hydrostatic pressure and in including the computation of nonhydrostatic pressure component for comparison.

SUNTANS allows the user to output profile data and three-dimensional data into separate files. Therefore I can set SUNTANS to export these files at a different time step. After the end of the simulation, surface temperature data from LBERI and the simulated results can be compared to clarify the computation of heat fluxes in the simulation.

Figure 4.10 is a representation of stations where profiles were extracted. The stations are associated with numbers from 1 to 11. Figure 4.11 demonstrates the correctness of the heat fluxes routine since the observed and the simulated data (Station 7), both being taken at the center of the main basin, exhibit a similar trend. The simulated data are slightly underestimated compared to the observed surface temperature. Figure 4.11 also shows the

surface temperature from hydrostatic and non-hydrostatic case, and they appear quite similar throughout the time series, but this aspect will be discussed in later section.

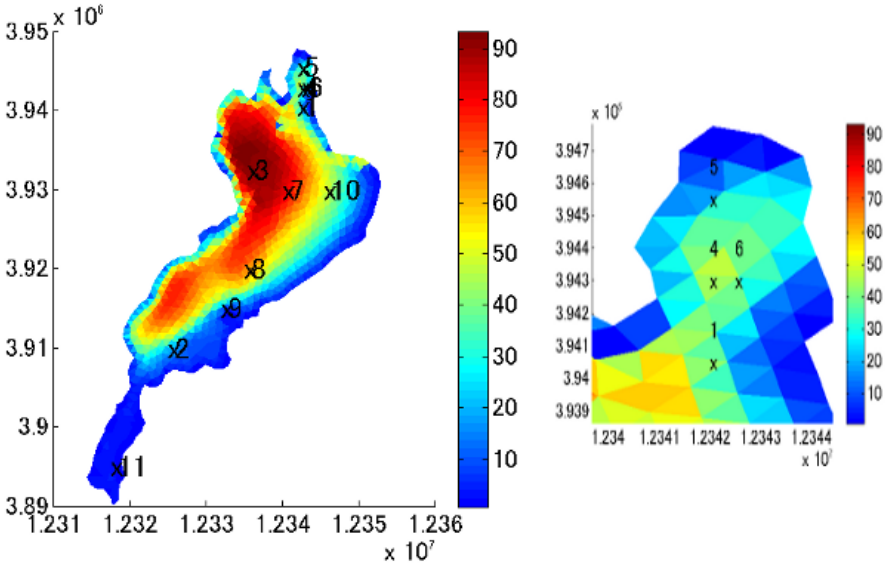

Figure 4.10: SUNTANS- Profile locations - Locations of the profiles output from SUNTANS. The blue dots are the Voronoi points of the cells

Figure 4.12 displays the temperature distribution over depth and time at Stations 1, 2, 3, 4, 6 and 8 from January 16th to September. This figure shows the stratification period clearly and reveals the thickening of the layer of high temperature gradient. Toward the end of the simulation, the surface temperature is about 26 °C and the temperature in the hypolimnion is about 8 °C, which appears to be similar to the temperature distribution observed with TurboMAP during the campaign in August 2001. Moreover, oscillations of temperature are visible, alluding to the presence of internal wave propagation. By focusing on the period August 20 to 31, we can assess the impact of the typhoon on the temperature distribution as well as on the propagation of basin-scale internal waves (Figure 4.13). For instance, at Station 4, the 19 °C isotherm, located within the metalimnion, shallows during the tyhpoon event after August 22, and then the isotherm oscillates until the end of the simulation. Also we notice that the isotherm exhibits a diel and two-day period, being consistent with the periods that were observed in the ADCP data during the campaign.

The next step would be differentiating between the simulated temperature and observed temperature in a neighboring location. Figure 4.13 depicts the simulated temperature distribution at Station 4 (location shown in Figure 4.10) and displays the metalimnion oscillating

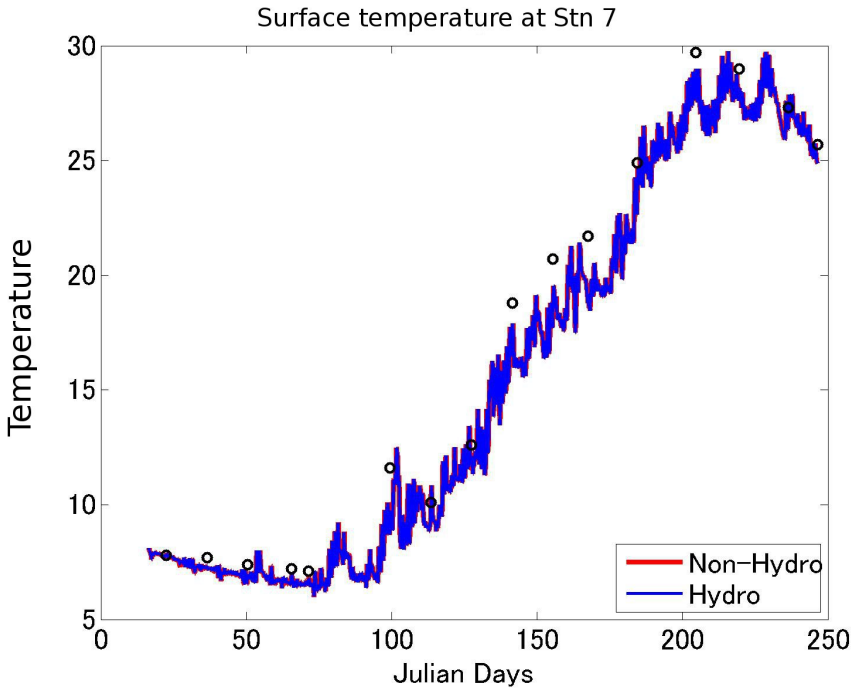

Figure 4.11: SUNTANS- Surface temperature - Surface temperature from SUNTANS: hydrostatic (blue curve) and non-hydrostatic (red curve) and observed surface temperature from LBERI (empty black circles)

around 15m depth. By comparing with TurboMAP temperature data (Figure 3.3), I can observe that the depth of the metalimnion is consistently simulated with SUNTANS. Although the layer at 24 °C appears to be thicker than in the observed data, the oscillations seem to be consistently reproduced. Also, the oscillations in the simulated data seem to lag a few hours behind compared to the observed data. This lag may come from the fact that the wind field was extrapolated from 5 locations around the lake. Therefore the specified wind field may be different from the actual wind field.

Because of the consistency between the simulated and the observed temperature field, the identification of the internal waves existing in the lake can be assessed. As pointed out earlier, diel and two-day periods in the simulated data were observed. Since internal waves are the oscillations of isotherms, a frequency analysis of isotherm elevation will clarify the periods seen in the temperature distribution. The isotherm elevation was made using a linear interpolation between the two closest points in the vertical, and the power spectrum was computed using isotherm elevation (20°C) from stations at the mouth and inside the bay (Station 1 and 4 respectively). Then spectra were smoothed in the frequency domain to increase the statistical confidence (Figure 4.14). These spectra corroborate the presence of diel period as

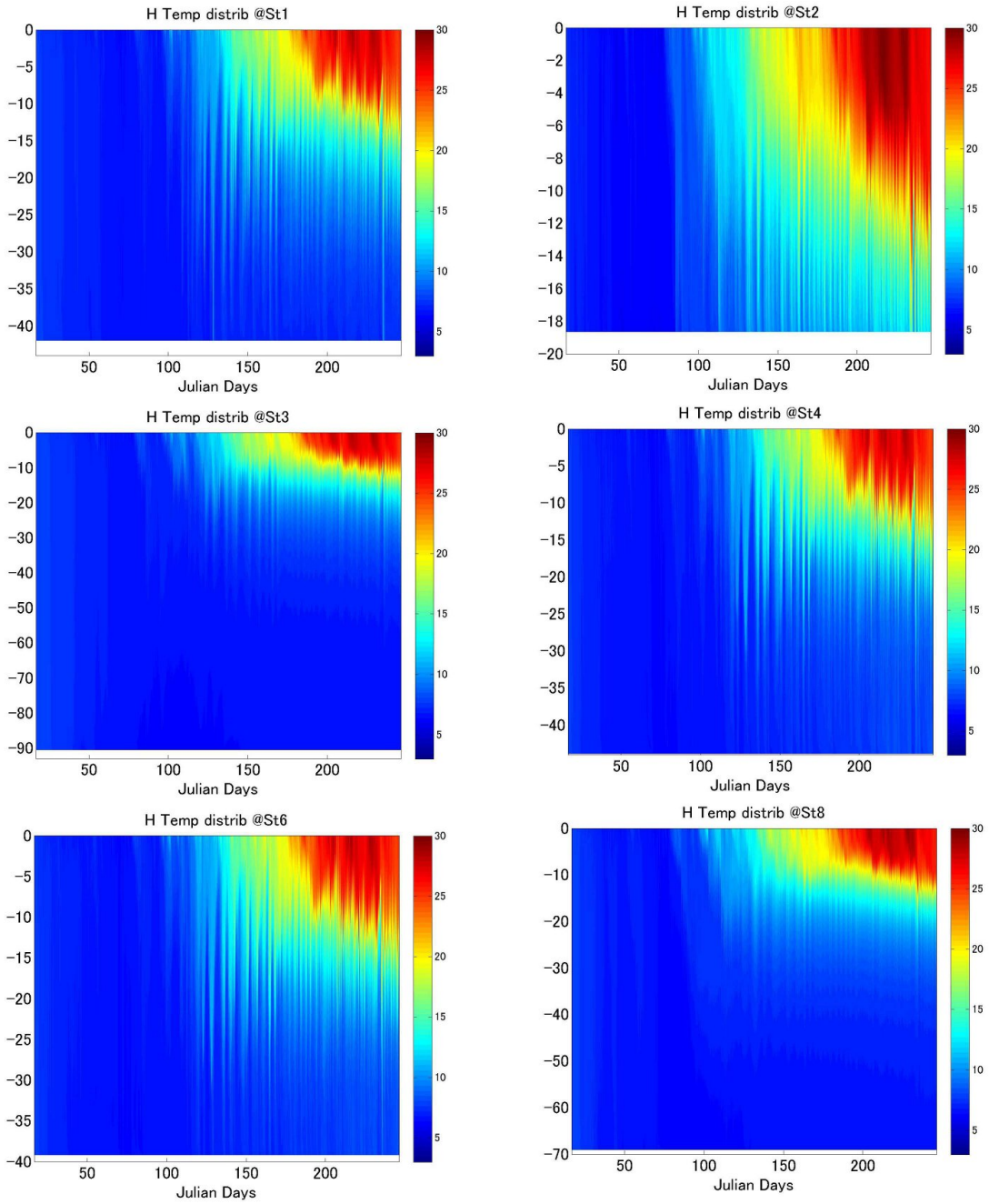

Figure 4.12: SUNTANS- Temperature distribution - Temperature distribution at several Stations output from SUNTANS. Vertical axis is the depth in meters, and horizontal axis is Julian day of the year 2001.

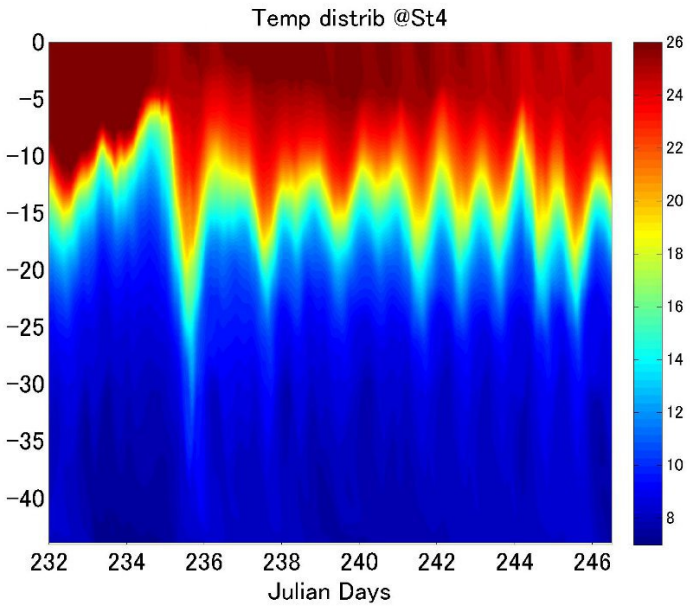

Figure 4.13: SUNTANS- Temperature Station 4 typhoon period - Temperature distribution at Station 4 between August 20 (Julian Day 232) and September 3 (Julian day 246). Vertical axis is depth in meters, and horizontal axis is Julian day of the year 2001.

well as a two-day period in the temperature field, since the isotherm oscillations exhibit two consistent peaks at low frequency: about 6×10^{-6} Hz and 1.2×10^{-5} Hz. Furthermore these frequencies are quite similar to the ones found in the observed data (Figure 3.16).

Within the frequency range $2 \times 10^{-5} \sim 4 \times 10^{-5}$ Hz, the spectrum at the mouth of the bay appears to be quite energetic compared to the spectrum inside the bay. This discrepancy points out the fact that oscillations within the main basin do not necessarily appear within Shiozu Bay. Also an excess of power is noticeable within the low-frequency range (1 and 2 days) at inside the bay compared to Station 1. This feature may be explained by the increase of oscillation amplitude caused by change of width (Sakai & Redekopp, 2010).

The three-dimensional simulation allows me to look at the spatial characteristics of the waves seen in the isotherm timeseries. In chapter 2, characteristics of basin-scale internal waves and their structures were presented. Therefore, by using the profiles data I can identify the internal waves. First of all the horizontal modes were identified through phase spectra of 20°C isotherm elevation at Stations 1, 2, 3 and 7 (Figure 4.15). This method makes it possible to look at how synchronized time series depend on the frequency directly, instead of filtering the time series and making a comparison afterward.

First I acknowledged the fact that at a frequency of about 6×10^{-6} Hz the phase differ-

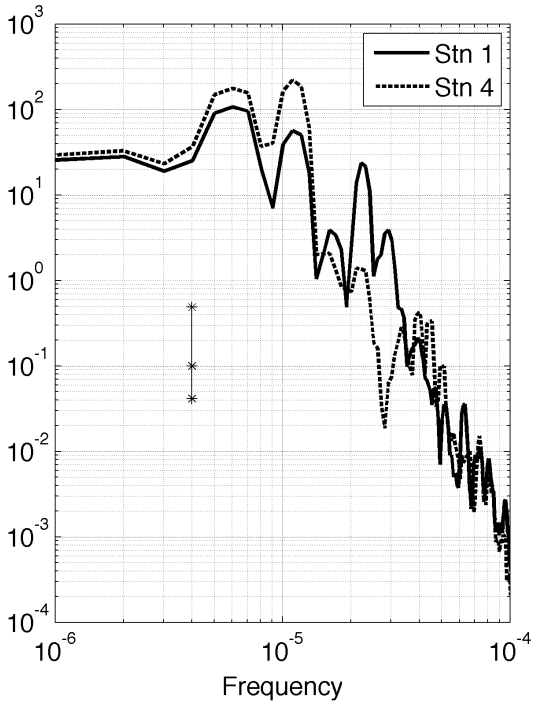

Figure 4.14: Isotherm elevation spectra at Stations 1 and 4 - Periodogram of 20°C isotherm elevations at Station 1 (*black line*) and Station 4 (*dashed line*); and the 95% confidence interval (*stars and thin black line*). Spectra have been smoothed in the frequency domain to improve the statistical confidence.

ence between Stations 1 and 2 is about π radians and about 1 rads between Stations 1 and 3. The results from Figure 4.15 allude to a horizontal mode 1 for this wave because elevations at Stations 1 and 2 are out-of-phase and slightly unsynchronized at Stations 1 and 3. Stations 1 and 2 are located at opposite sides of the lake, whereas Station 3 is located at the west side of the lake. Then the other low frequency internal wave found in the spectra, the diel periodic wave, exhibits synchronised oscillations at Stations 1 and 2 (phase difference is about 0 radians) and phase difference of $\pi/2$ radians between Stations 1 and 3. These results are not consistent with a horizontal mode 1 wave. We analyzed the phase difference between Station 1 and Station 7 (in the middle of the lake), and the phase spectrum suggests that the two signals were out-of-sync at the diel period range. The results of the phase spectra concerning the diurnal wave are consistent with a horizontal mode 2 wave. Also, in Figure 4.13 we notice that isotherms are parallel. That leads to the conclusion that the low-frequency internal waves are of vertical mode 1. The results concerning the modes of the low-frequency internal waves are consistent with Shimizu *et al.* (2007).

In Chapter 2, it was mentioned that the Earth's rotation influences the propagation of basin-scale internal waves by forcing them into a rotation around the lake that may be cyclonic or anti-cyclonic. The time lag of filtered time series of isotherm elevation at Stations 1 and 3 gives such information. If the time lag is shorter than half the period we can as-

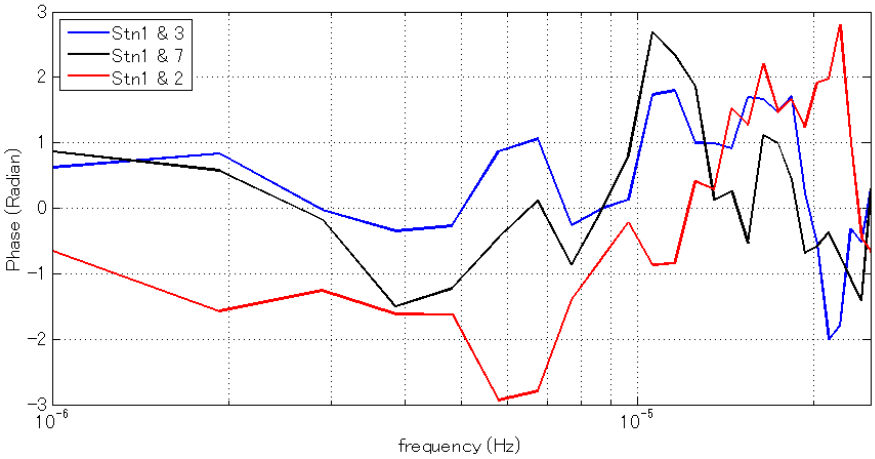

Figure 4.15: Phase spectra - Phase spectrum of the 20°C between Stations 1, 2, 3 and 7.

sume that the rotation pattern is counter-clockwise (cyclonic), and if the time lag is greater than half period, the propagation is anti-cyclonic. Figure 4.16 and Figure 4.17 depict the filtered time series between Stations 1, 2 and 3 for both periods, and they clearly show the cyclonic propagation for both waves since the time lag of the elevation between Stations 1 and 3 is less than half of the period. Therefore I confirm the presence of a two-day Kelvin wave first baroclinic mode and a diel wave horizontal mode 2. These results are consistent with Shimizu *et al.* (2007) in Lake Biwa, as well as the observed data presented in Chapter 3 (Auger *et al.*, 2013). Moreover, I can remark that isotherm oscillation amplitude of the diel wave decreases during the first half of the timeseries (before August 27) and increases after. The diel wave observed with the ADCPs showed the same feature, because it was likely energized by the diurnal wind. The fact that the diel wave is energized by the diurnal wind suggests that the 1-day wave is an inertial wave.

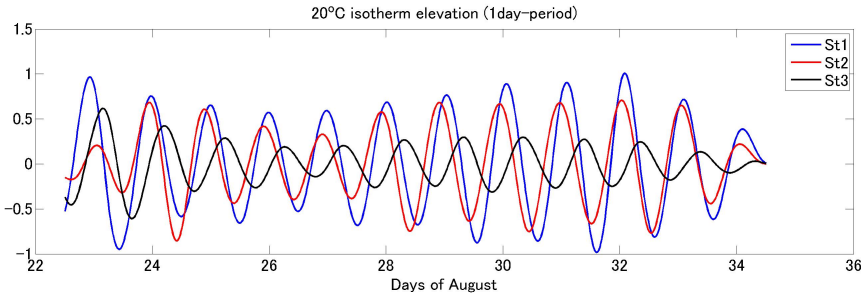

Figure 4.16: One day isotherm elevation - 20°C isotherm elevation at Stations 1, 2, and 3 associated with the diel wave

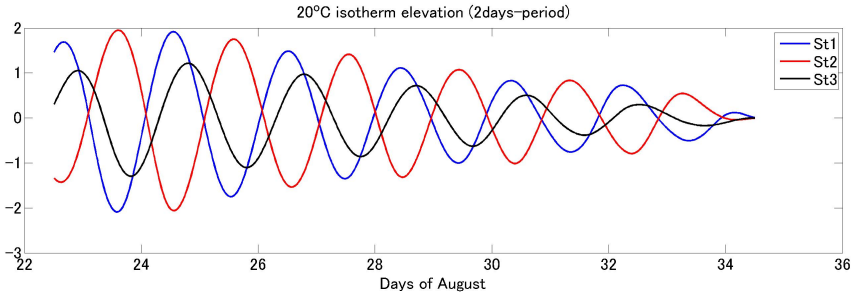

Figure 4.17: Two days isotherm elevation - 20°C isotherm elevation at Stations 1, 2, and 3 associated with the 2-day wave

4.3.2 Difference between Hydrostatic and Non-Hydrostatic

One of the strength of SUNTANS is the non-hydrostatic pressure computation. Bergh & Bernsten (2009) mentionned that non-hydrostatic pressure may play a role in scales smaller than the kilometer-scale, even though the nonhydrostatic effect is not completely accounted for. However Hodges *et al.* (2000)'s conclusion on the nonhydrostasy by using ELCOM states that if $\Delta x/\Delta z > 100$ nonhydrostatic effects would be overwhelmed by numerical diffusion. Therefore two simulations were carried out, one with the hydrostatic pressure component only and the other including the non-hydrostatic pressure component.

There are two ways to pinpoint differences between hydrostatic and non-hydrostatic simulation. SUNTANS offers the possibility to output the component of the non-hydrostatic pressure, that is expressed as the difference between the total pressure (p) and the hydrostatic pressure (p_h): $p = p_h + q$. As an example, Figure 4.18 displays time series of q during a part of the simulation. Until Julian day 80, q reached the order 10^{-6} Pa, whereas after Julian day 80, q decreased 100-fold. Comparing Figure 4.11 against 4.18 I notice that the correlation with the beginning of the surface layer warm-up and q is significant until the stratification is established.

Also, by just looking at the non-hydrostatic component of pressure, how effective non-hydrostasy is on the dynamic remains unknown. Since hydrostasy assumption implies the neglect of the the total derivation of the vertical velocity due to the pressure field, the distribution of w should exhibit the influence of the nonhydrostatic assumption on the field as shown in Figure 4.19. For instance between Julian days 40 and 60, an important discrepancy is present in the distribution: the amplitude reaching the mm s^{-1}, vertical velocities inside the water column are of opposite direction. However, as the non-hydrostatic pressure, after

Julian day 80, velocities dramatically decreased, becoming much smaller than the order of the mm s^{-1}.

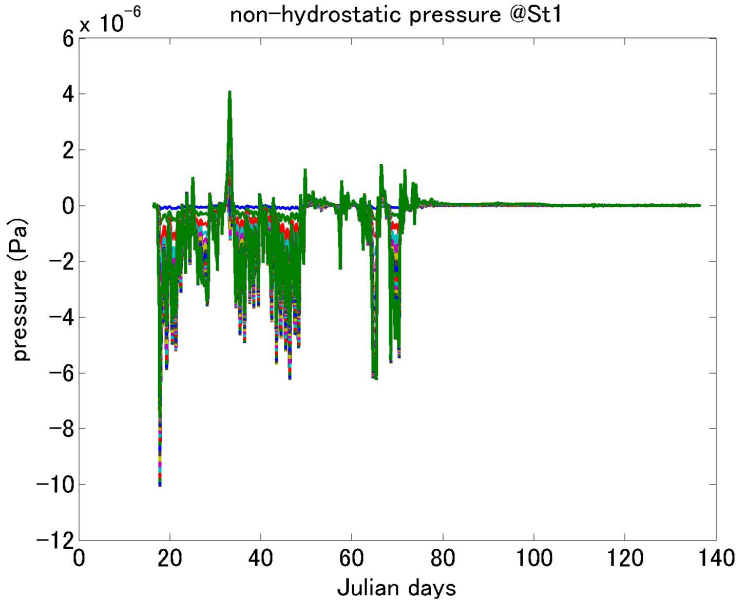

Figure 4.18: Non-hydrostatic pressure at Station 1 - Non-hydrostatic pressure (Pa) at each z-level over time, from Julian day 16 to 138

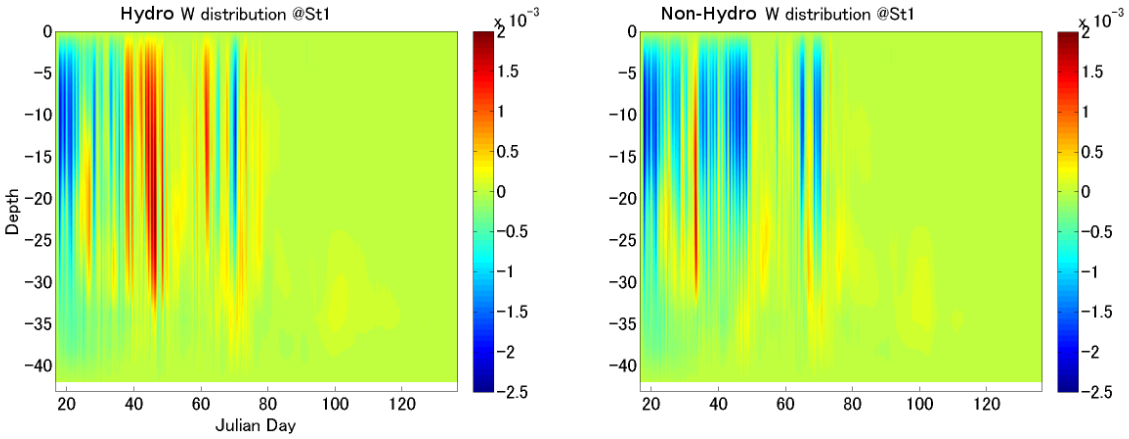

Figure 4.19: Vertical velocity distribution at Station 1 - Distribution of vertical velocity (in m s^{-1}) at Station 1. On the left panel the velocity issued from a hydrostatic run, on the right panel the velocity output from nonhydrostatic run.

Vitousek & Fringer (2011) underline the link between the depth of the interface (i.e., metalimnion) and the resolution needed to properly compute the non-hydrostatic effects. By analyzing the Korteweg and de-Vries equations (Korteweg & de Vries G, 1895), they conclude that the horizontal resolution must agree with the condition $\Delta x < h_1$, with h_1 being the depth of the metalimnion. Also Dorostkar (2012) documented similar limitations of the grid for the nonhydrostasy effect to appear, with another numerical model (MITgcm). Since

during winter time the water column is unstratified, we can assume that the depth of the metalimnion is infinite; therefore non-hydrostatic effects would be noticeable with a coarse resolution grid. However I expect that intensity of nonhydrostastic effects would depend also on the grid resolution. Then, when the lake enters the stratified period (the beginning of spring in Lake Biwa) nonhydrostasy is drastically diminished.

The statement that the vertical gradient of pressure compensates the buoyancy is the basis of the hydrostatic assumption. This simplification of the vertical momentum equation leads then to the neglect of the total derivation of the vertical velocity compared to the buoyancy ($b = -g\frac{\delta\rho}{\rho_{ref}}$ where $\rho = \rho_{ref} + \rho_0(z) + \delta\rho(x,y,z,t)$). Therefore the hydrostatic assumption is consistent with reality when

$$\frac{\mathrm{D}w}{\mathrm{D}t}\frac{1}{b} \quad << 1 \tag{4.28}$$

Based on the incrompressibility assumption, we can extract another relationship between w and b. Incompressibility implies $\frac{\mathrm{D}\rho}{\mathrm{D}t} = 0$, which leads to:

$$\frac{\mathrm{D}\delta\rho}{\mathrm{D}t} + w\frac{\partial\rho_0}{\partial z} = 0 \tag{4.29}$$

And by multiplying by $-g/\rho_{ref}$ we obtain:

$$\frac{\mathrm{D}b}{\mathrm{D}t} + wN^2 = 0 \tag{4.30}$$

where N is the buoyancy frequency expressed as $N^2 = -g\partial\rho_0/(\rho_{ref}\partial z)$. Supposing that each element of the total derivative possesses the same scale ($\mathrm{D}/(\mathrm{D}t) \sim U/L$), we can carry out an *analysis of scales* with equations 4.28 and 4.30. From equation 4.30 we can consider that

$$w \sim \frac{Ub}{LN^2} \tag{4.31}$$

where U is a velocity scale and L a horizontal length scale. Then, when incorporated in equation 4.28, it leads to a condition on the scales of the system to agree with the hydrostatic assumption (Marshall *et al.*, 1997b):

$$\frac{U^2}{L^2N^2} \quad << 1 \tag{4.32}$$

When the water column of a lake is stratified, N^2 is large, meaning the condition for hydrostasy will be reached quite easily. However in the case of a completely mixed lake during winter, like Lake Biwa, N^2 is small and may even been considered as null ($N^2 \sim 0$). Therefore, the condition would not be reached and it would imply that the nonhydrostatic component of pressure is not negligible.

What these results suggest about this comparison of hydrostasy against nonhydrostasy for a coarse grid, is that nonhydrostatic effects are noticeable even though the resolution of the grid is quite low, when the lake is completely mixed, or overturning. Such features would not appear in the oceanic case (offshore region), since ocean does not experience a complete mixed state. Therefore the numerical study of lakes during the overturning period should include nonhydrostasy.

However, discerning the fate of the internal wave field within the bay is quite complex since on the horizontal plane, about 30 cells make out Shiozu Bay, visible in Figure 4.3. This number includes the cells corresponding to water columns not deep enough to reach the metalimnion. Thus no internal wave processes are expressed. Therefore, the fine-scale grid will be used to simulate the propagation of internal waves in Shiozu Bay.

4.3.3 Fine resolution grid

Limitations and initial conditions The bathymetry and the histogram of Voronoi distance are displayed in figure 4.20. Here, the shape of the cells has been removed to reveal the bathymetry. The colorbar stands for the depth at each cell in meters. From this figure, the fact that there is no fixed resolution for this type of grid is underlined. However, the Voronoi distance histogram displays that most of the Voronoi distances remain within the range between 80 and 150 meters. The histogram shows two modes in the distribution: one mode with a mean at about 120 meters and the other mode with a mean at about 90 meters. The number of grid cells is about 36000 at the surface layer. The resolution in the vertical axis remains the same as the coarse grid, namely $\Delta z = 0.93$. Marshall *et al.* (1997b) mentions that $\gamma = u^2/(L^2N^2) << 1$ is the condition for the hydrostasy assumption, and in using this grid $\gamma \sim 0.2$, therefore the simulation has been run in using the non-hydrostatic computation.

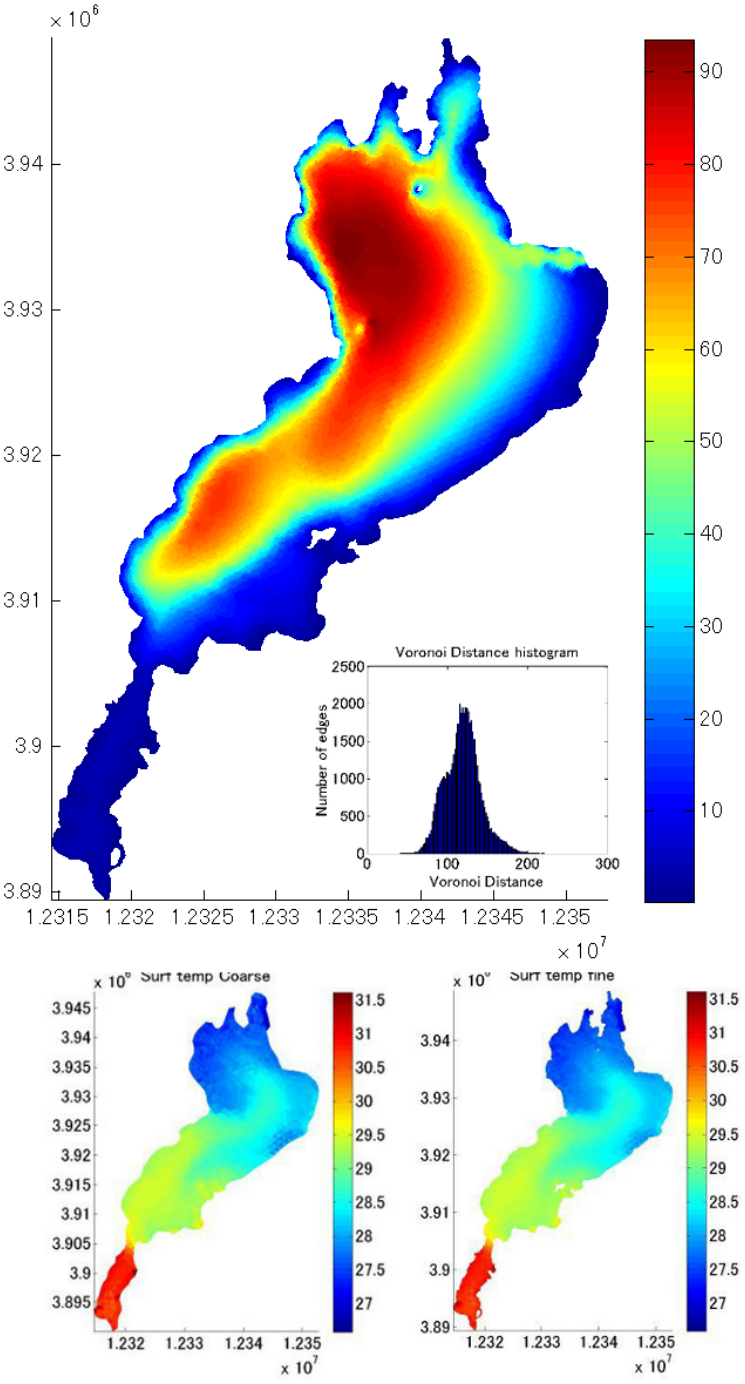

Figure 4.20: Fine grid bathymetry - A representation of the bathymetry used in the fine grid case as well as the Voronoi distance associated with this grid (histogram). The colorscale is the depth in meters. The two bottom panels are a comparison between the surface temperature of the coarse grid simulation and the initial step of the fine scale grid

A visual comparison between the coarse grid and the fine-resolution grid highlights the difference between the two. Because the shoreline is more finely resolved, it becomes more complex and exhibits features (such as islands or side bays) that did not appear in the coarse grid case.

When using the fine resolution, the computation time increases significantly. For example, in this case the computation time goes from 10 hours to more than a month. To reduce the computation time, I shortcut the simulation by taking an output of the temperature and velocity field at a specific time. I use the data from a lower resolution simulation as the initial condition for the fine scale case and force with a higher resolution. Then, I interpolate to match the fine-scale grid and use this as an initial condition. Unfortunately, the new features made the simulation unstable because of the initial velocity field at the boundaries. Because the most important in the study of internal waves is the temperature field, I assumed quiescent velocity field as initial condition. To minimize the discrepancy in the velocity field, the simulation was initiated one month before the typhoon event, when the current volocity field was weak, using the coarse grid results (Figure 4.20). Thanks to this method, the computation time was reduced to 9 days. To keep the conditions specified by equation 4.27, the time step was set to 10 seconds.

Results When I compare the simulated temperature distribution against the observed temperature distribution, the stratification appears consistent. However oscillations in the temperature field appear to lag in the simulation in comparison to observed data, as we mentioned realier (Figure 4.21). When I compared current velocity time series at the same depth and location, velocity seems to be out of phase at the beginning of the time series (before August 27), but synchronized after August 27. August 27 corresponds to the diel periodic wind blowing in the afternoon, which corroborates the diurnal wave being an inertial wave. Moreover the time series display the dominance of the North/South axis on the velocity field, as during the observation in August 2001.

The discrepancy of the velocity can be explained by the fact that wind velocity and direction appear to vary throughout Lake Biwa as seen in Figure 4.7. Orography, such as mountains, greatly affects the wind field over lakes, as observed by Lee *et al.* (2008) in the

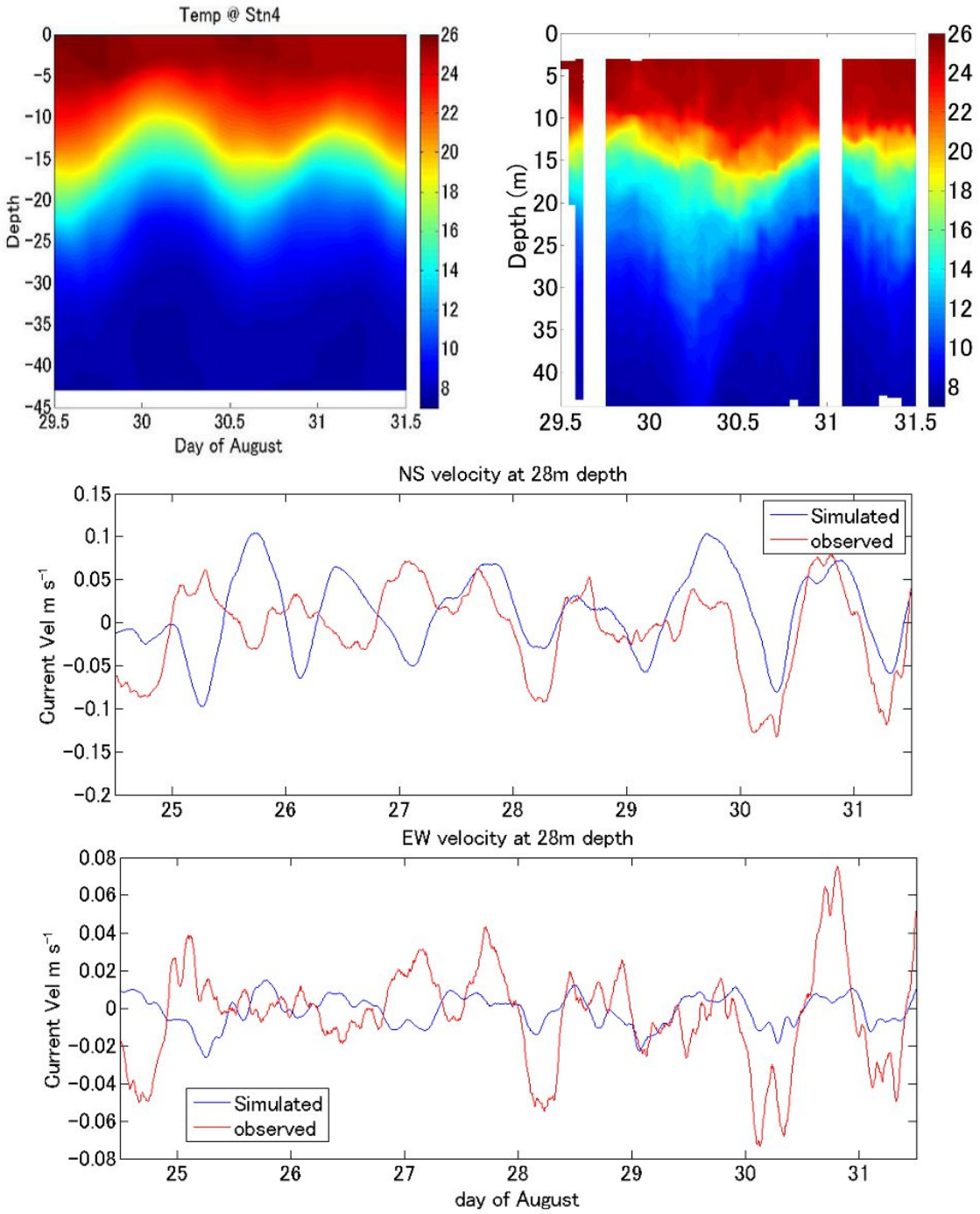

Figure 4.21: Fine scale temperature - A comparison between temperature distribution from SUNTANS fine-grid at Station 4 (left side panel) and TurboMAP experiment (right side panel) on top of the figure. Comparison of northward and eastward current at 33 meters depth at the mouth of the bay between observation (*red line*) and simulation (*blue line*)

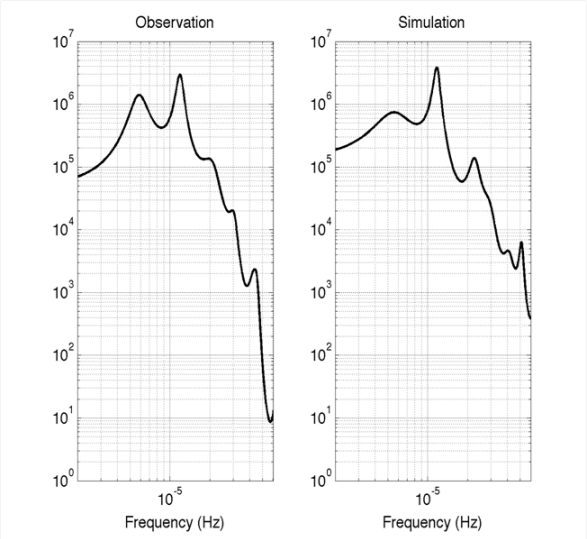

Figure 4.22: Velocity spectra - Horizontal velocity spectrum below the metalimnion in using Auto-Regressive spectrum from observation (*left panel*) and simulation (*right panel*)

Ariake sea vicinity and Shimizu *et al.* (2007). As it is noticeable in Figure 4.9 the wind direction is slithly off, and we could compare only with the 48 hours long weather data at the end of August. Interpolated wind data including the typhoon period could not be certified by observed data on Lake Biwa.

However, horizontal velocity distribution against time and depth shows common features that are noticeable in the observed data, but were not present in the coarse grid result. Some of the common features were the weak velocity field below 20 meters depth slightly before August 29 and the step-like horizontal velocity profile below 25 meters around day 30.5 (Figure 4.23). These features were the cause of enhanced shear within the hypolimnion. Even though the depth at the location is not identical (observed: $\sim$50 meters, simulated: $\sim$35 meters) and the processes are not exactly at the same depth, these two features are similar. Moreover the current velocity amplitude in the fine resolution case is close to the observed amplitude.

Figure 4.22 shows the spectrum of horizontal velocity using the auto-regressive spectrum method from simulation and observation data. In the simulation, velocity associated with the internal Kelvin wave seems to possess less energy than in the observation case; as opposite to the inertial wave that possesses more energy in the simulation than in the observed data. Moreover, looking at the spectra of isotherm elevation, peaks at these frequencies appear to possess the same power. Such discrepancy should be expected, since the ratio of potential to kinetic energy is much smaller than 1 for the Kelvin wave low horizontal mode and the ratio diminishes for higher horizontal mode (Antenucci & Imberger, 2001). This result

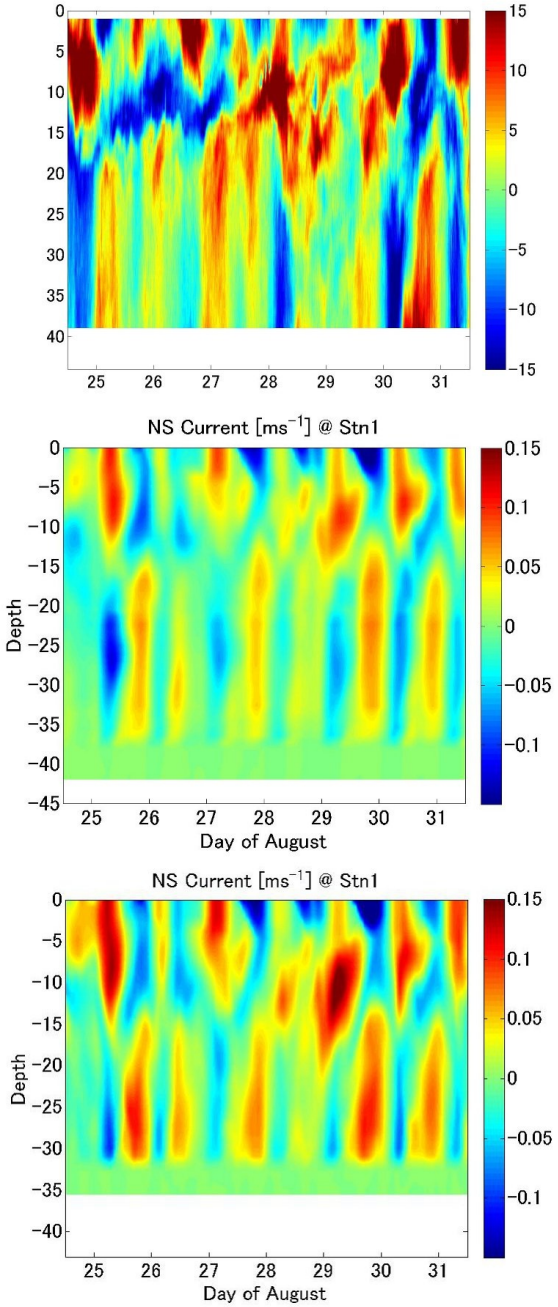

Figure 4.23: Current at the mouth of Shiozu Bay - A comparison of North/South current velocity between observed at the mouth of Shiozu Bay (ADCP 3) in cm s^{-1} (top panel), simulated from coarse gird (Stn 1) in m s^{-1} (middle panel) and simulated from fine scale grid (Stn 1) in m s^{-1} (bottom panel) from August 24 noon to August 31 noon.

suggests that the velocity field is dominated by the diel wave in the simulation, whereas in the observed data the energy peak at the V1H1 Kelvin wave's frequency appears to possess slighlty lower power than the energy peak at the V1H2 Kelvin wave's frequency.

4.4 Discussion

The purpose of this chapter is to understand what the dynamics of the low frequency internal wave field within the bay. The process of complete dissipation of waves within the bay would be characterized by an increase of background potential energy in the bay, since the mixing in the metalimnion elevates potential energy irreversibly. Therefore, I look at the bay-average potential energy of Shiozu Bay computed as:

$$PE(t) = \int_x \int_y \int_0^H \rho g z \, \mathrm{d}z \mathrm{d}x \mathrm{d}y \tag{4.33}$$

where z is the height from the bottom, H the depth of the water column, and ρ the density depending on the height and time ($\rho(z,t)$).

Because I am not dealing with analytical data, the integration changes slightly. From the grid files in SUNTANS, I use the cell areas to compute the total potential energy inside the bay.

$$PE_n(t) = \int_0^H \rho_n g z \, \mathrm{d}z \tag{4.34}$$

being the potential energy per surface unit (Jm^{-2}) for the cell n

$$PE(t) = \sum_{n=1}^{N} \mathcal{A}_n \int_0^H \rho_n g z \, \mathrm{d}z \tag{4.35}$$

where $\mathcal{A}_n$ is the area of the cell n and N the total number of cell in the grid. Then I compute the time series of the potential energy within Shiozu Bay.

The time series of potential energy exhibits diurnal and two-day oscillations, alluding to the propagation of the internal waves seen earlier (Figure 4.24). Because the data set deals with three-dimensional data, the sampling period is 2 hours. However other frequencies are not noticeable. This may be explained by the fact that integrated potential energy

magnifies the contribution of vertical mode 1 waves compared to higher modes. Indeed V1 waves deepen or shallow isotherms of the entire metalimnion, whereas higher mode waves will shallow only a part of the metalimnion. The power spectra of the detrended potential energy corroborates this statement because the power of the first low-frequency internal waves ($\sim 6 \times 10^{-6}$ Hz and $\sim 1.2 \times 10^{-5}$ Hz) is almost 100-fold the power of the next peak in the spectrum (Figure 4.25). Additionaly within the low-frequency internal waves range the Kelvin wave appears to dominate the potential energy field.

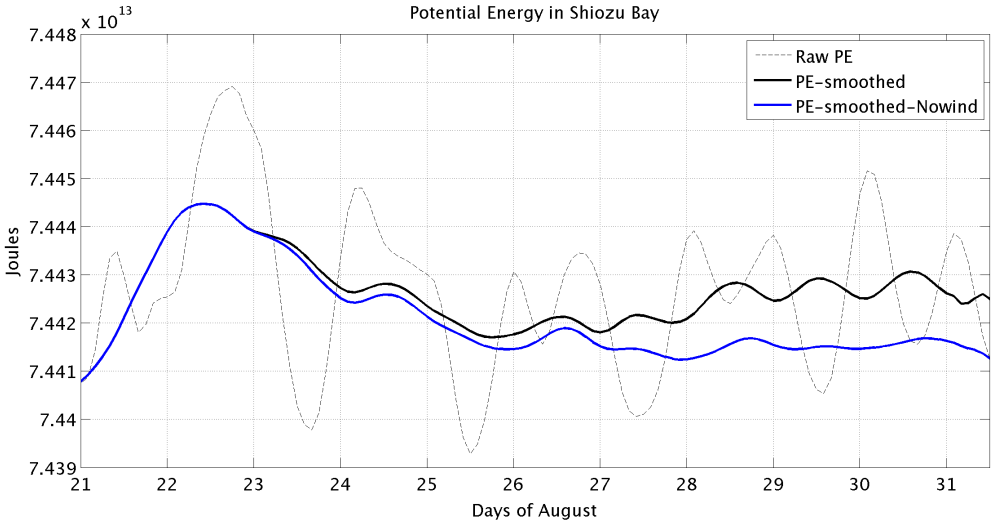

Figure 4.24: Time series of potential energy - Three types of time series of potential energy within Shiozu Bay. The dashed black line stands for the original values of PE(t) with wind forcing after the typhoon event. The *thick black* and *blue* lines represent the 42-hours smoothed original PE(t) time series and the 42-hours smoothed potential energy in the case of no wind forcing from day 23.3, respectively.

The trend of the potential energy time series exhibits another feature of Shiozu Bay. The trend of the parameter shows that the energy decreases immediately after the typhoon (August 23), whereas the energy seems to increase slightly before August 27. The smoothing of the time series, by making use of a moving average over 42 hours, reveals the increase of potential energy after August 27. August 27 corresponds to the strong afternoon diel wind blowing over Lake Biwa, especially in the vincinity of Shiozu Bay, shown by the wind distribution around the lake in Figure 4.7 at the two Northernmost meteorological stations. This correlation would imply that the increase of potential energy would come from the input of energy by the diel wind. However the fact that increase starts slightly before August 27 may suggest a more complex origin. The diel wind forcing is likely responsible for a part of

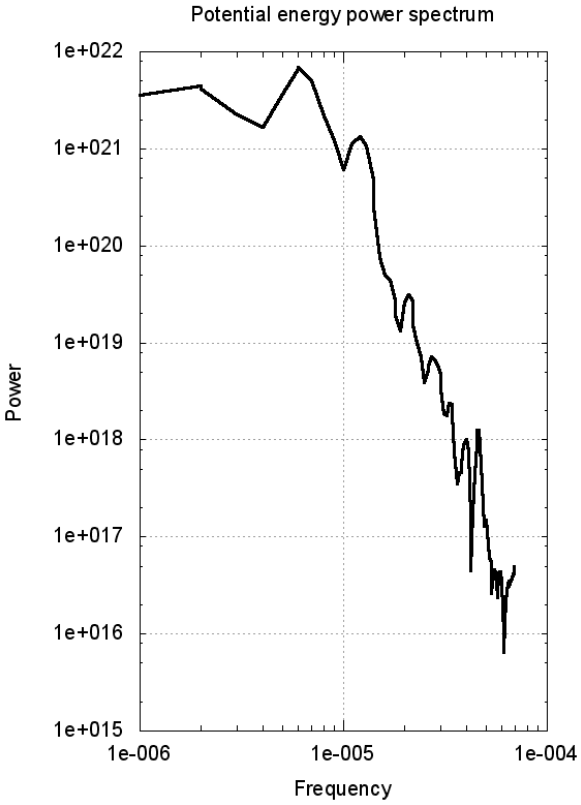

Figure 4.25: Potential energy spectrum - Power spectrum of the total potential energy of Shiozu Bay based on the potential energy time series plotted in black in Figure 4.24. The spectrum was smoothed in the frequency domain to improve the statistcal confidence.

the energy input, but another process, such as dissipation of the wave field through breaking, might have a role in the energy input.

A method to qualify the impact of the wind forcing after the typhoon is a simulation that switches off the wind forcing after the typhoon event. In this case, the wind was switched off at day 23.3, roughly 8 hours after the end of the typhoon event, in order to match a quiet period and avoid a sharp decrease in wind forcing. Figure 4.24 exhibits the discrepancy of potential energy for the case with wind stress and without wind stress. The change in potential energy over time, marked by a 2×10^{10} Joules difference between the two time series during the diel wind period, alludes to the main role of the diel wind for the increase in the potential energy. Indeed, the integrated potential energy decreases until it reaches a constant state at about 7.4415×10^{13} Joules until the end of the time series. This statement alludes to the fact that the increase in the potential energy in the orignal run is due to the wind forcing after the typhoon, rather than an energy transfer from kinetic energy to the background potential energy through wave breaking and dissipation.

To assess the energy dissipated in the bay I take advantage of the turbulence closure model included in SUNTANS, that is the Mellor-Yamada 2.5 closure model (Mellor & Ya-

mada, 1982). The Mellor-Yamada 2.5 closure model can provide values of turbulent kinetic energy dissipation rate, ε. Namely, ε is estimated as a ratio of velocity cube to a length scale.

$$\varepsilon = \frac{q^3}{l * B_1} \tag{4.36}$$

where B_1 is considered as a universal constant ($B_1 = 16.6$). The unit of ε is W/kg, then in computing:

$$\sum_{n=1}^{N_c} \sum_{k=1}^{N_k} \varepsilon_{nk} \rho_{nk} \mathcal{A}_{nk} \Delta z_{nk} \tag{4.37}$$

for each time step, I obtain a time series of how much kinetic energy is dissipated per second. N_k and N_c are the total number of cells in the vertical and horizontal planes, respectively. Because the time series is basin-averaged, the sampling period is 2 hours. Moreover, wind forcing may generate high ε within the surface layer, so the surface layer has to be ignored to estimate the energy dissipated by the internal wave field within the thermocline or below. Also the energy dissipation in the surface layer would be the situation where the energy input by the wind directly dissipated within this layer, as explained in Figure 1.4 and by Boegman (2009), and is thus irrelevant to the internal wave-induced dissipation.

When I compare the two time series of integrated ε with and without the surface mixing layer (the first 8 meters were set to be turbulence-free $\varepsilon \sim 10^{-10}$ W kg^{-1}), I notice that some enhanced dissipation events are caused by the wind below the surface layer. When the wind blew (August 20 to 23 and after 27), the great discrepancy between the two time series exhibits the impact of the wind on the surface layer. For instance within the typhoon period, August 22, the integrated ε is about 2 order of magnitude higher in the case where the surface layer is included ($10^3 << 4 \times 10^4$ J s^{-1}). Although in some cases the surface layer contains a significant part of dissipation during wind event, seen in Figure 4.26 with the discrepancy between the two curves, time series of dissipated energy clearly shows enhanced dissipative events taking place elsewhere than the surface layer. Because the surface layer is assumed to be experiencing low intensity turbulence, I infer that these highly dissipative events occured below the epilimnion.

Figure 4.26 shows that these high dissipative events after the typhoon do not reach the total amount of energy within Shiozu Bay. At the peak of potential energy right after the

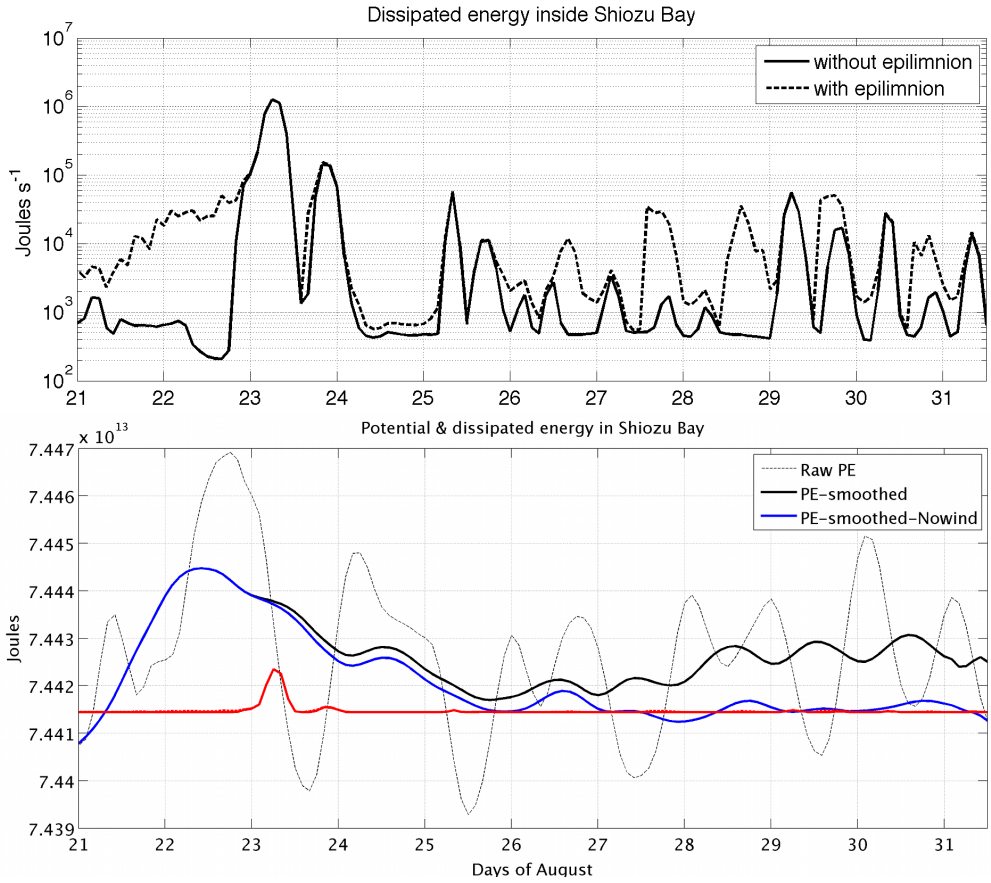

Figure 4.26: Dissipated energy in Shiozu Bay - Top panel: Timeseries of integrated kinetic energy dissipation rate within Shiozu Bay (unit: Js^{-1}) original values in *black dash-line*, and in assuming the epilimnion being turbulence-free ($\varepsilon_{epil} \sim 1 \times 10^{-10}$ W kg^{-1}) in *black*. Bottom panel: same as Fig. 4.24 with total energy dissipated energy inside Shiozu Bay + background potential energy (*red line*)

typhoon, the time series shows that the bay possesses 7.447×10^{13} J. By assuming that each high dissipation level remains for 2 hours, the total dissipation of kinetic energy at the same period would be 1.1×10^{10} J. I assume that the last portion of PE time series without wind is the potential energy at rest (or background potential energy) since it remains constant for at least 4 days. Thus the maximum energy dissipated is about the same order of potential energy variation when compared to the background potential energy (Figure 4.24), though the actual amount of energy detained by the internal wave field at the same period is several times larger than the total energy dissipated inside Shiozu Bay (shown in the bottom panel of Fig. 4.26).

Assume 1000 J s^{-1} being the background dissipation (it corresponds to the scenario where each single cell possesses a dissipation rate at the order of 10^{-10} W kg^{-1}), the dissipation rate below the epilimion reached 10 times the background value after the typhoon on several occasions. Despite these enhanced turbulence events, the total eernergy dissipated remained much smaller than the energy detained by the low-frequency internal wave field. Therefore I infer that the low-frequency internal waves did not dissipate completely inside Shiozu Bay.

The discrepancy between the dissipation and the available energy to the internal wave field brings up the issue of the isotherm oscillation origin. For instance, the internal Kelvin wave entering the bay should be either dissipated completely or reflected back to the main basin, but neither of these situations is visible in the data set. Therefore, I may infer that the identity of the waves may not remain in the bay. In the field of coastal water, an internal Kelvin wave generates oscillations in estuaries and its straight, with a frequency equal to the Helmholtz frequency. This frequency is the natural frequency depending on the size of the estuary.

In assuming Shiozu Bay to be composed of two rectangles, one representing the straight of length L_S and the other rectangle the rest of the bay, the width of both rectangles being equal. The Helmholtz frequency can be computed as follows:

$$\omega = \sqrt{\frac{g' A_2}{A_{RS} L_S}} \tag{4.38}$$

where g' is the reduced gravity, A_2 the area of the cross-section between the lower layer of the two rectangles, and A_{RS} the area of the bay (second rectangle). With $g' = 0.0305$, $A_2 = 12 \times 2.5 \times 10^3$ m^2, $L_S = 1 \times 10^3$ m and $A_{RS} = 5 \times 10^3 \times 2.5 \times 10^3$ m^2 the Helmholtz frequency becomes $\omega = 4.3 \times 10^{-5}$ Hz. This frequency is much higher than the frequency of the internal V1H1 Kelvin wave (6×10^{-6} Hz), as well as the frequency of the V1H2 Kelvin wave (1.2×10^{-5} Hz). Therefore, the Helmholtz frequency can not explain the low-frequency oscillations inside the bay. However this frequency may explain the peaks of energy in the frequency range $3 \times 10^{-5} \sim 5 \times 10^{-5}$ Hz in the spectrum taken from inside the bay (Figure 4.14).

As explained previously, internal waves may break at boundaries, generating high turbulence events. An internal wave breaking occurs when the slope of the bottom boundary (α) is about the same as the angle of the internal wave ray (θ). The angle of the internal wave ray depends on the stratification (N^2) and the frequency of the wave. Thus I can estimate the frequency of internal waves that will break du to topography. This frequency is called the critical frequency (f_c) and it equals:

$$f_c = \sqrt{N^2 \sin(\alpha)^2 + f^2 \cos(\alpha)^2} \tag{4.39}$$

where $N^2 = \frac{g}{4\pi^2 \rho_0} \frac{\partial \rho}{\partial z} \sim \frac{10^{-2.7}}{4\pi^2}$ and $f = 1.33 \times 10^{-5}$Hz the inertial frequency and $\alpha = 0.023$ rad ($\sim 1.32^\circ$) at the depth of the metalimion. Then using equation 4.39 we obtain $f_c = 1.7 \times 10^{-4}$ Hz, indicating that internal waves with frequency similar to f_c would ultimately break onto the slope. However the internal Kelvin waves possess a frequency (6×10^{-6} Hz and 1.2×10^{-5} Hz) much lower than f_c. This statement suggests that the Kelvin waves would not break, corroborating the inference made from Figures 4.24 and 4.26

Based on the equation of internal Kelvin wave equation (2.18), it is noticeable that the elevation depends on the size of the bay compared to the internal Rossby Radius of deformation. Because of the consistency between the simulated data and the observed data, I suppose the Rossby Radius of deformation is equivalent in the simulation and the observed data, e.g., $R_R = 5.5$ km. By looking at Fig 4.20, I deduce that at the metalimnion level, that is the wave-guide for internal waves, the width of the bay (~ 2 km) is almost twice smaller than

R_R. Therefore, the width would preclude the propagation of the whole internal Kelvin wave, but the wave may scatter.

In following Kawamura *et al.* (2005) as well as LeBlond & Mysak (1978), I assess the scattering of the internal Kelvin wave inside Shiozu Bay. When the bay width is much smaller than the internal Rossby Radius of deformation, the excited wave period within the bay may be computed as follows:

$$T = \frac{4L}{c(2m_a - 1)} \tag{4.40}$$

By assuming the horizontal mode (m_a) would be 1, the phase speed of the 1 baroclinic mode (c) to equal 0.5 m s^{-1} and the length of the bay (L) to be 6 km, we obtain a period of the excited wave to be about 13.3 hours ($\sim 2.1 \times 10^{-5}$ Hz). This period is lower than the period of the main internal Kelvin wave. Therefore this result illustrates the fact that the main internal Kelvin wave does not generate a 2-day wave by scattering at the mouth of the bay.

The equation 4.40 under the assumption of scattered wave of horizontal mode 1 proves the wave would have a much higher frequency than the internal Kelvin wave that propagates within the main basin. Assuming higher horizontal mode would increase further the frequency, therefore making the assumption of scattered wave not coherent. Furthermore, this statement alludes to a more complex dynamic of the internal Kelvin wave. The requirement to use equation 4.40 is the bay to be much smaller than the Rossby radius of deformation ($\sim$ 5.5km). But the condition does not provide a clear threshold to assert if equation 4.40 can be used in my case. Therefore to get a clear picture of the wave propagation, I focus on Shiozu Bay, compute the isotherm elevation (19°C for instance) and filter the obtained time series to display oscillations due to the internal Kelvin wave.

Figure **??** shows the 19°C isotherm elevation after being filtered at each cell (bandpass between 4×10^{-6} and 8×10^{-6} Hz using a Butterworth filter order 6) to match the propagation of the internal Kelvin wave V1H1. Because the wave entering the bay will only be a part of the internal Kelvin wave, the rotational pattern may be noticeable as an amplitude modulation of the wave. Therefore the elevation associated with the Kelvin wave in the bay was normalized ($\eta_{norm} = \eta / max(|\eta_{elevation}|)$ at each time step. To keep track with the elevation

caused by the Kelvin wave in the whole basin, the average elevation in the bay is illustrated in the bottom panel of each case.

When the crest of the wave enters Shiozu Bay on August 30 in early morning (Figure **??**), the wave exhibits high elevation on the right-hand side, consistent with an internal Kelvin wave. Also, the propagation step-by-step ($\Delta t = 2$ hrs) shows a cyclonic pattern within the bay, with the entered part of the Kelvin wave moving around the bay. This result is consistent with the fact that the wave does not dissipate completely in the bay, based on the potential energy and total dissipated energy (Figure 4.24). Moreover, the results show that during he experiment, the outward V1H1 Kelvin wave was observed during the August 2001 campaign.

Processes of turbulence event The enhanced turbulence below the epilimnion may remind of the observed enhanced turbulence event presented in Chapter 3 (Auger *et al.*, 2013). The distribution of simulated ε over time and depth at the same location as the observation exhibits similarities (Figure 4.28). An enhanced turbulence event appears at the same time, reaching 30 meters depth, but does not last the same amount of time. Also other hypolimnetic turbulence events, though much weaker and only few meters high in the water column, appear to occur on a daily basis. When comparing simulation against observation, the closure model employed in SUNTANS appears to overestimate the kinetic energy dissipation rate within the hypolimnion (Simulation: $\varepsilon \sim 10^{-6}$ Wkg^{-1}, observation: $\varepsilon \sim 10^{-7}$ Wkg^{-1}), as well as underestimate of the turbulence intensity within the metalimnion. Stacey *et al.* (1999) show that overestimation in weakly stratified regions and underestimation in strongly stratified regions are inherent to the turbulence closure model (MY2.5), in comparing turbulence estimation through observational methods and closure model.

The discrepancy between the simulated and the observed data may be due to the lack of data between the deepest point of the profile and the bottom at the experiment location. Indeed the simulated data are displayed from surface to bottom whereas the observed data from the observation do not show data the last 5 m. In addition the deep turbulence event (day 29.75) occurs at the same time as high velocity. Moreover the isotherms overlaid on ε distribution are squeezed and pulled apart where the 16-m thick turbulent layer occurs. These events are similar to the observed features. The discrepancy of water column depth is due

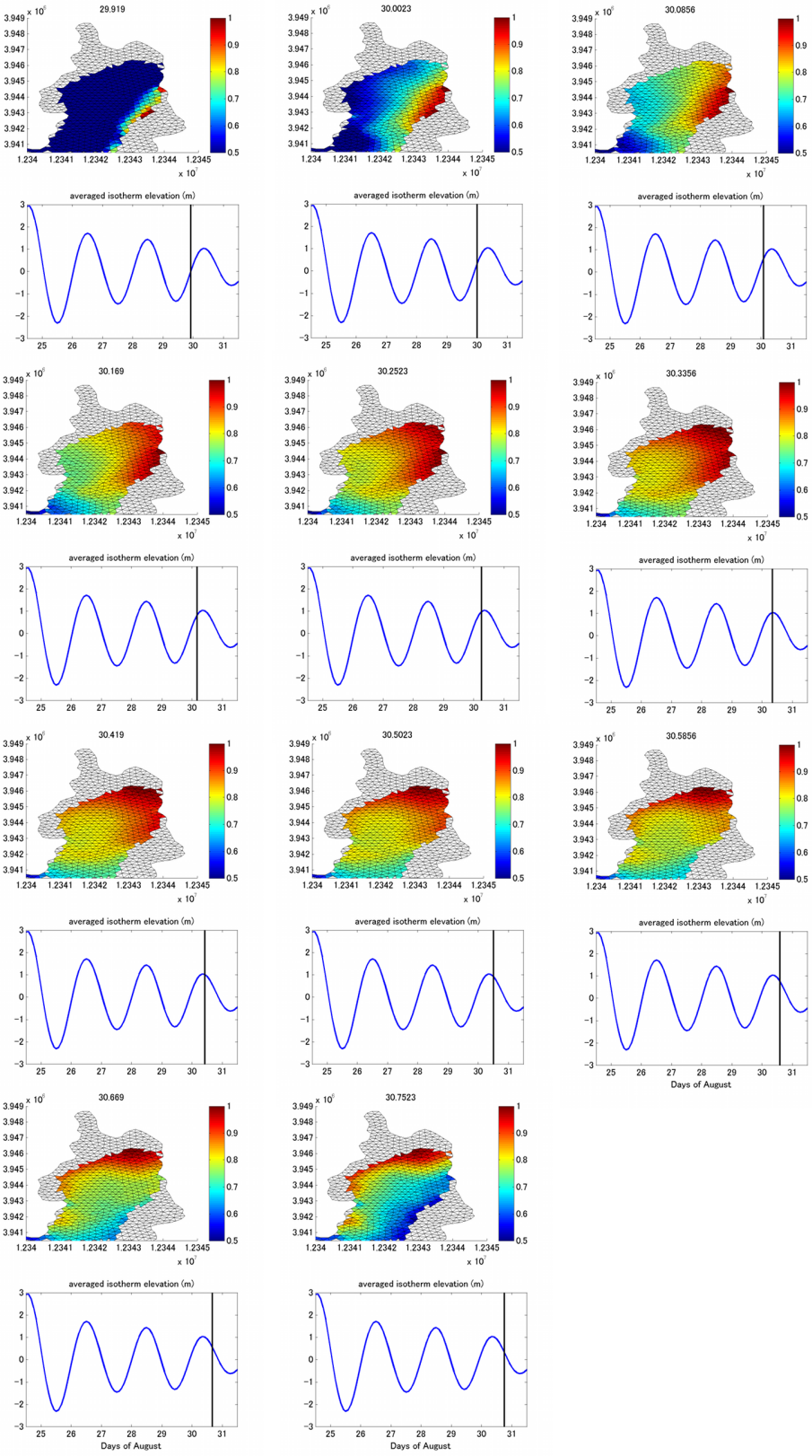

Figure 4.27: Kelvin wave within Shiozu Bay - 19°C isotherm elevation associated with the internal Kelvin wave (period: ~ 2 days) in Shiozu Bay. The bottom pannel displays the bay average elevation in the bay. A vertical thin black line is overlaid to indicate what moment we are looking at. The elevation starts at day 29.919 and ends on day 30.7523.

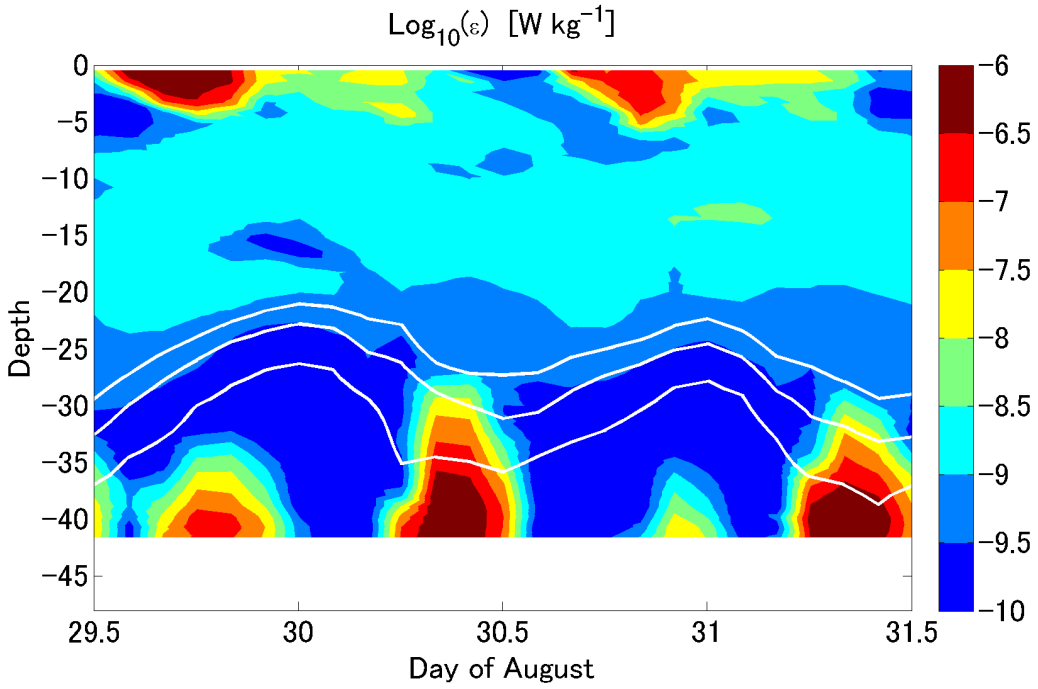

Figure 4.28: Profile of kinetic energy dissipation rate - Distribution of kinetic energy dissipation rate in logarithmic scale (unit: Wkg^{-1}). 8-9-10 °C isotherms are overlaid in *thick white line*

to the stair-stepping approach of bathymetry computation. If the depth changes sharply, depending on the cell thickness and horizontal resolution, the bottom depth will differs greatly between two neighbouring water column; which is the case in our situation. Even though the simulation appears to be slightly different from the observation, we use the simulated data to understand the process that generates the enahnaced turbulence event likely linked to the low-frequency internal wave field

The time series of simulated turbulence dissipation reveal that turbulent dissipation took place below the epilimnion, but the data do not identify the entire dissipative feature in the bay. By making use of the three dimensional distribution of ε, I can identify where the highly dissipative events occur in the bay. Figure 4.29 shows the distribution of $\log_{10}(\varepsilon)$ following a transect accross the bay as shown in the left panel of the same figure. The transect corresponds to day 30.419, the period when total dissipation within the bay was high (10^4 J s^{-1}). This figure shows that the dissipation reaches the order 10^{-6} W kg^{-1} above the bottom and this feature appears to be specific to this area. Moreover, when looking at the location of this turbulent event on the left panel of Figure 4.29, I notice that this event seems to take place at the entrance of the bay, when the layer below 20 m depth becomes narrow.

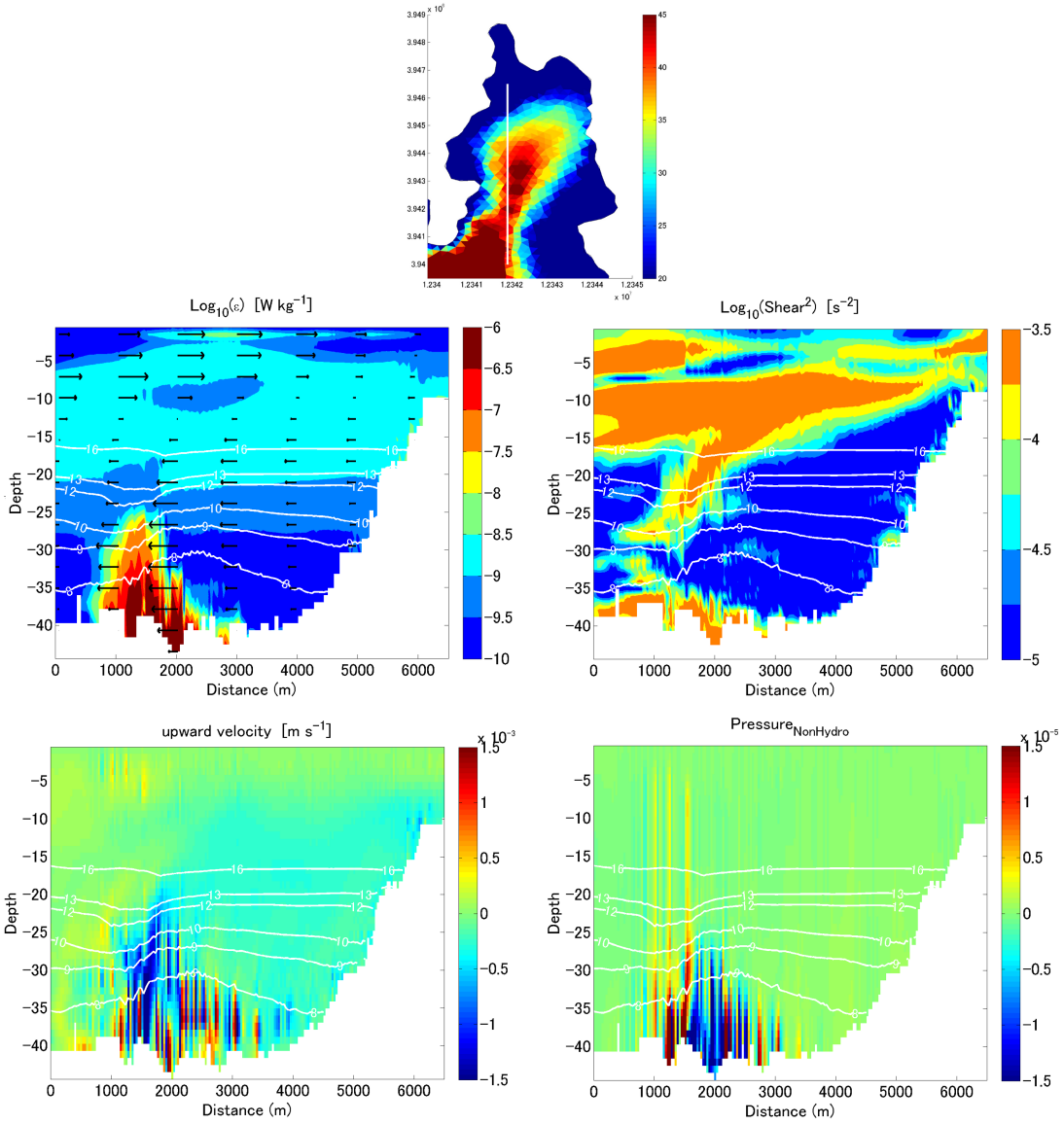

Figure 4.29: Dissipated energy Shiozu Bay transect - Top pannel: Bathymerty of Shiozu Bay, *white line* stands for the transect. (a) Distribution of ε (right panel) in logarithmic scale along the transect. Isotherms of 8-9-10-13-16 °C elevation are overlaid on the dissipation distribution in *white lines*. (b) Distribution of $log_{10}S^2$ on day 30.41. Isotherms of 8-9-10-13-16 °C elevation are overlaid. (c) Distribution of vertical velocity on day 30.41. Isotherms of 8-9-10-13-16 °C elevation are overlaid. (c) Distribution of non-hydrostatic pressure component on day 30.41. Isotherms of 8-9-10-13-16 °C elevation are overlaid.

In stratified medium, turbulence is usually generated by velocity shear. The black arrows overlaid on Figure 4.29 indicate the direction as well as the flow speed along the North-South axis. On the same transect and moment, bottom water appears to experience an intense turbulence event that is associated with locally increased southward velocity. The velocity at this location exhibits an increase from the metalimnion and a decrease mid-way toward the bottom. This feature of latitudinal velocity is likely to generate velocity shear above and below this hypolimnetic enhanced velocity portion, as shown in the top right panel of Figure 4.29. The magnitude of squared shear ($S^2 = (\frac{\partial u}{\partial z})^2 + (\frac{\partial v}{\partial z})^2$) is plotted in logarithmic scale as seen with the colorbar. The vertical resolution used in the computation of velocity shear is $\Delta z = 0.93$. The distribution clearly shows the correlation between the turbulent event and the shear that both occur at the same place. As mentioned previously, I notice the presence of enhanced shear below and above the enhanced velocity section. However, there is a location where ε is high, but exhibits shear with weak intensity the order of 10^{-6} s^{-2} (the layer between 31 and 35 meters depth).

The region with enhanced turbulence and weak shear alludes to another source of turbulence than shear production. Around the same location that has high ε values along the transect, isotherms above the enhanced turbulence region appear to deepen. Therefore it may allude to a linkage between the two features. Moreover, slightly after the deepening of isotherms, the water section is accelerated. Within the same region of enhanced turbulence with weak shear, the distribution of vertical velocity displays an enhancement of w. The bottom left pannel of Fig. 4.29 shows that vertical velocity reached the scale of mm s^{-1} whereas it is one order of magnitude smaller elsewhere. This statement emphasizes the role of strain in the generation of enhanced turbulence event within the hypolimnion. In addition isotherms below 20 meters are deepening, whereas above 20 meters (16°C for instance) they do not exhibit this feature. Also, the intensity of the deepening seems to be more important when isotherms are close to the bottom. Because the isotherm deepening and the enhanced vertical velocity ossur at the same location, I assume they are linked to the same process.

The bathymetry shown in Figure 4.29 highlights the fact that the enhanced turbulence events occurred where the lake below 20 meters depth is funnelled (cone-shaped) and the bottom exhibits a slope. Moreover, this event occurred in the same area where the enhanced

turbulence event isotherms seem to deepen, alluding to a possible link between the enhanced turbulence and isotherms deepening. Sakai & Redekopp (2010)'s theoretical work on the effect of narrow lake's topography changes on internal waves documents the superiority of width effects on internal wave elevation compared to the effect of depth change. This statement may suggest that the main feature of the topology that affects the internal wave field is the narrowing of the lake. The fact that affected isotherms are located below 20 m depth, where the narrowing is much more pronounced compare to the surface layer, strengthens the assumption of the role of the lake width.

Such deepening of isotherm and high velocity in an area with greatly changing topogropahy was associated with hydraulic jump (Dorostkar, 2012). Thorpe (2005); Horn *et al.* (2001) hypothesize that this phenomenom occurs when the velocity is great and the topology is complex. Although hydraulic jumps have been observed at various locations and where strong tidal flow encounters a sill (Farmer & Armi, 1999), they are not well understood (Boegman, 2009; Dorostkar, 2012). Also, hydraulic jumps appear to be associated with locally enhanced velocity and enhanced kinetic energy dissipation rate (Thorpe, 2005).

By assuming the flow to be hydrostatic, the composite Froude number (G^2) is an indicator of whether the flow is hydraulically controlled. When $G^2 = 1$ the flow is critical, subcritical when $G^2 < 1$ or supercritical when $G^2 > 1$. Since the internal waves exhibit a vertical mode 1 pattern (water column can be approximated to a two layer medium), the composite Froude number is expressed as:

$$G^2 = \frac{u_1^2}{g' d_1} + \frac{u_2^2}{g' d_2} \tag{4.41}$$

where u_i and d_i are the velocity and the thickness of the layer i respectively. Based on transect data, let's use $T_1 = 25.5°\text{C}$, $T_2 = 7°\text{C}$, $g' = 0.0305$, $u_1 = 0.15$ ms^{-1}, $u_2 = 0.18$ ms^{-1}, $d_1 = 18\text{m}$ and $d_2 = 25\text{m}$, thus $G^2 \sim 0.08$. This value of the composite Froude number suggests that the water is at a subcritical state, so the assumption of hydraulic jump can be discarded.

The previous equation used to compute the composite Froude number assumed that the basin or bay is composed of two rectangles of constant width from top to bottom, as well as constant depth. This assumption may lead to consistent results in large scale systems, but

in the case of lakes, such an assumption may not hold. In the case of lakes, the bathymetry changes greatly within a small area, especially at the boundaries with the presence of slopes. Because the change of width may play a role in the generation of hydraulic jump, Sannino *et al.* (2009) introduced an expression for the composite internal Froude number including the change of depth, G^2 becomes:

$$G^2 = \frac{1}{w_I^{-1}\int_0^w (g'H_1/u_1^2)\mathrm{d}y} + \frac{1}{w_I^{-1}\int_{yL}^{yR} (g'H_2/u_2^2)\mathrm{d}y} \tag{4.42}$$

where $w_I \sim 2$ km is the width at the interface between layer 1 and 2, H_1 and H_2 are the thickness of the layer 1 and 2 along the cross section represented by y. Because the velocity does not change greatly it is assumed constant. If the other parameters are taken as in the previous case, then we obtain $G^2 = 0.15$. Therefore, the value of the composite Froude number being lower than 1 suggests that the physical process provoking the enhanced shear and isotherm deplation is not an hydraulic jump.

According to the simulated data, G^2 remains lower than unity because of the flow characteristics, more specificaly the flow speed as well as the stratification. In Dorostkar (2012), the water column at the location of the hydraulic jump displays a flow speed reaching 50 cm s^{-1}, and the temperature gradient between the top and bottom layer appears to be greater in the case of Lake Biwa. In addition, studies dealing with hydraulic jump (Dorostkar, 2012; Cummins *et al.*, 2006; Maderich *et al.*, 2012) with a Froude number around the critical value ($G^2 = 1$) documented deepening of almost every isotherm. Plus, when they studied the effect in a lake and a bay, the narrowing was applied to the whole vertical, whereas in the case of Shiozu Bay, the width decrease appears to be effective below the metalimnion (below 20 meters) where the contraction is the most noticeable.

Because the enhanced turbulence occurs at a specific location, it is worthwhile to assess the location with the horizontal distribution of ε in the hypolimnion over time (Fig 4.30). At the bottom of the figure, the 19°C isotherm elevation is displayed to show the evolution of the internal wave field. Figure 4.30 clearly highlights the location specificity since it appears to occur periodically at the narrowing of the bay below the metalimnion.

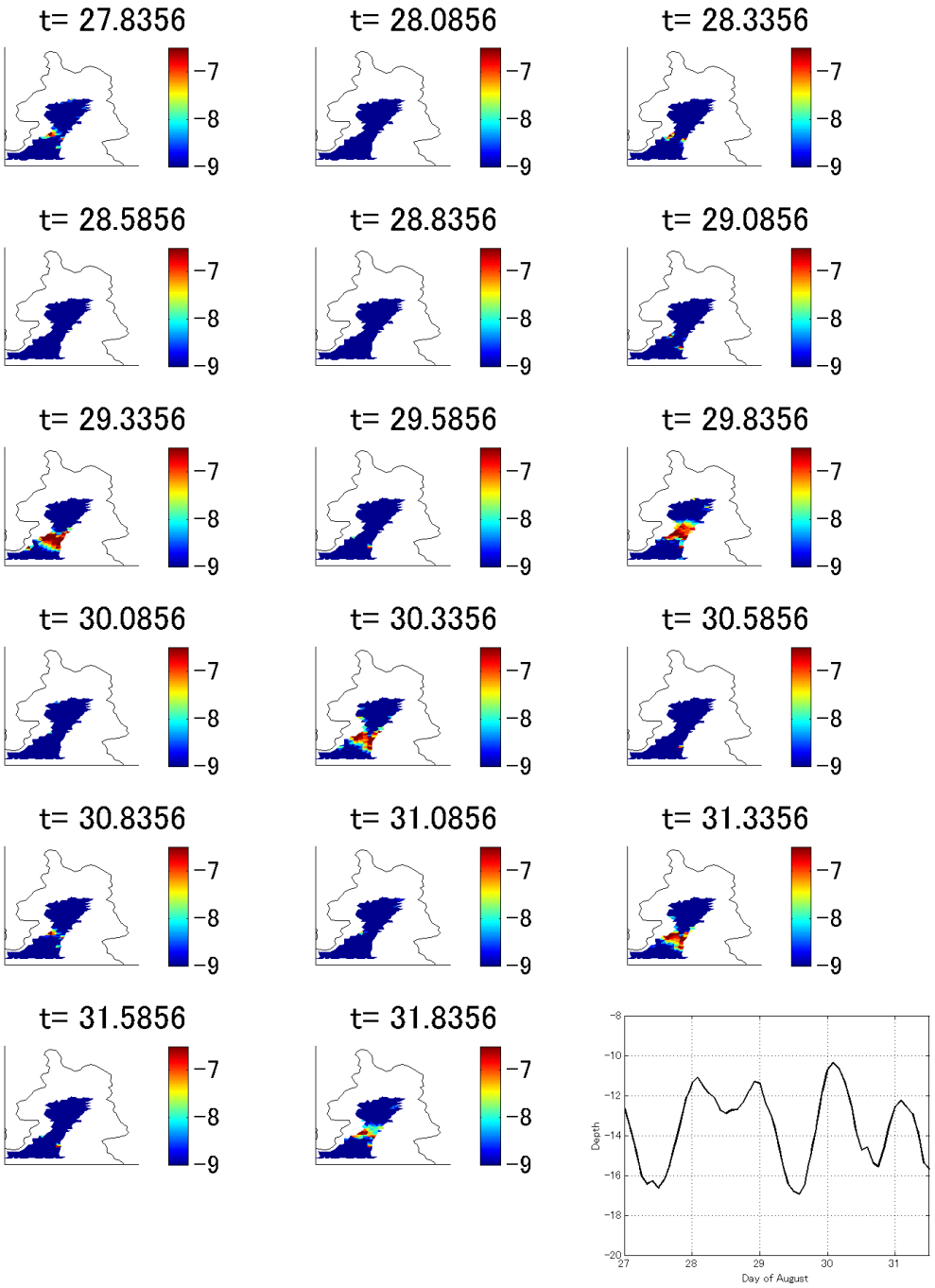

Figure 4.30: Kinetic energy dissipation rate horizontal distribution - Horizontal distribution of the kinetic energy dissipation rate within Shiozu Bay at level 40 with time step of 12 hours. 19°C isotherm elevation

So far, it has been shown that the hypolimnetic enhanced appears to be linked to the deepening of isotherms deep in the water column, as well as to be localised at the bays contraction. When looking at the temperature distribution as well as the horizontal velocity at about 33 meters during the same time of day as Fig. 4.29, I notice that the deepning of isotherms (left panel of Fig. 4.31) and the increased of velocity (right panel of Fig. 4.31) are due to contraction effect.

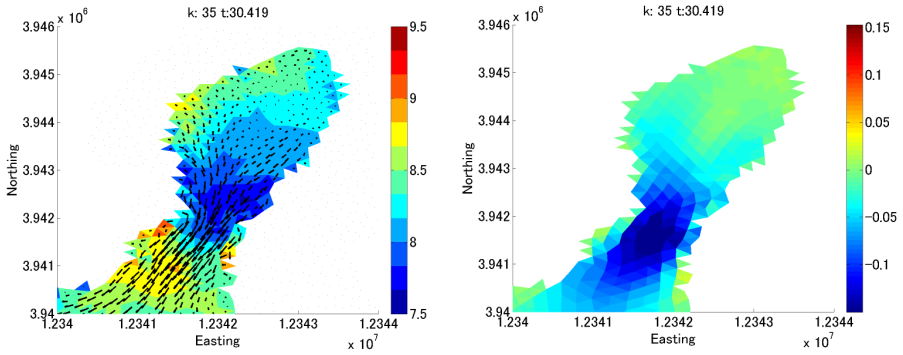

Figure 4.31: Temperature and velocity - left side represents the temperature field with velocity field (*black arrows*) and the right panel represents the northward velocity field at the layer 35 ($\sim$ 33 meters)

Previous studies, such as Dorostkar (2012); Sannino *et al.* (2009), documented at location where the contraction affects the entire vertical boundary, with the whole metalimnion being deepened. However, in the case of Shiozu Bay, the contraction appears to be effective only below the metalimnion. Computing the composite Froude number (G^2) by assuming more than 2-layer would decrease the density gradient between the layers and may increase the Froude number to the critical value ($G^2 = 1$). However this method would not match the data since the velocity clearly shows a 2-layer flow, making the assumption of a 3-layer flow inconsistent.

de la Fuente *et al.* (2008)'s results show that non-hydrostasy acts against the non-linearity, conclusively generating a solitary wave. As mentioned by Vitousek & Fringer (2011), the non-hydrostatic effect would not be effective if Δx is higher than the depth of the metalimnion, which is our case. Even though the grid resolution would prevent the generation of solitons, I look at the distribution of the non-hydrostatic pressure qualitatively. As one can see in the lower panel of Figure 4.29, the non-hydrostatic pressure is relatively high at the

narrow region of the bay in comparison to the rest of the transect ($3 \times 10^{-5} >> 10^{-7}$). The fact that high values of non-hydrostatic pressure are located just above the bottom, and not around the isotherms deepening, may suggest that propagating soliton waves would not be generated even with smaller Δx. Moreover this intense activity of non-hydrostatic pressure would suggest the presence of non-linear effects at this location.

The equation to compute the composite Froude number is based on the assumptions that the flow is hydrostatic, with no mixing and no friction(Ivey, 2001). Figure 4.29 clearly shows the presence of intense mixing downstream the hypolimnion flow and the presence of relatively enhanced non-hydrostatic pressure, which would make the use of the composite Froude number not clear.

Few studies show the impact of the topography upon the temperature and at the same time upon the velocity field. Dorostkar (2012) explains the increase of velocity by the flow being in a critical state (hydraulic jump), corroborated by a composite Froude number equals to 1. As mentioned earlier, it is not the case here. Thus the acceleration below the metalimnion is so far unexplained. One can argues the assumptions made for the hydraulic jump, and if they would have an impact on the velocity field. Mixing, as well as nonhydrostasy, would affect the flow at smaller scale than the region of accelerated flow. However friction of bottom or side wall may affect the velocity field.

SUNTANS implements bottom stress in using the bottom roughness length, set at 5 mm (Wüest & Lorke (2003) 0.1 mm $< z_0 <$ 10 mm and Umlauf & Lemmin (2005) used 10 mm), and side wall drag is computed with the drag coefficient $C_w = 0.0025$. Pratt (1986) studies the impact of bottom friction upon hydraulic controled flow, and found that when the flow is subcritical, the friction causes the flow to accelerate. The explaination of this unintuitive effect of friction is based on the ability of friction to remove energy from the flow. Because in subcritical flow the energy is mainly detained in potential form, the energy of the flow can decrease only by deleting potential energy, thus decreasing the layer thickness and increasing the flow downstream.

Pratt (1986) mentions that contraction and sill would have the same effect on the flow, that is the deepening and increase of velocity when the flow is subcritical. Moreover these processes would occur slightly downstream. These conditions for these phenomena to occur

matches the situation in this study as we can see on Figure 4.29. Because the event occurs far from the bottom, the source of the deepening of isotherms is suggested to be due to the wall friction. Moreover Figure 4.31 bottom panels clearly shows the impact on temperature horizontal distribution at the exit of contraction downstream with an increased southward component of the velocity field.

This process is consistent with the assumption of turbulence event due to low-frequency internal wave field. Indeed flow being contraled by the topography implies a greater impact at the scale that dominated the flow. Moreover the impact on isotherm will be greater at the scale that dominates the isotherm elevation. During this part of the thesis I have showed that the low-frequency internal wave field dominates both. Fig. 4.32 emphasizes the correlation between enhanced turbulence events in the hypolimnion with low-frequency internal waves. This figure shows that intense turbulence events occur during the trough of the internal wave field. Moreover, these hypolimnetic turbulence envents seem to be more intense during the diel wind is blowing (after August 28), marked by the isotherms deepening further.

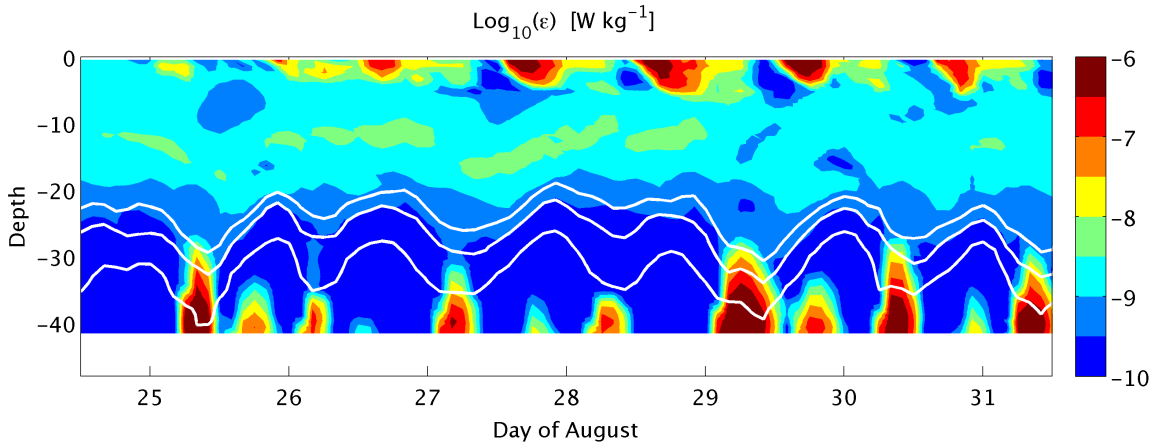

Figure 4.32: Dissipation rate distribution from day 24.5 to 31.5 - Distribution of the kinetic energy dissipation rate in logarithmic scale at the same location as TurboMAP campaign, with isotherms (8-9-10 °C overlaid in *white line*)

4.5 Conclusion

Making use of SUNTANS, I was able to simulate an internal wave field that is consistent with the observed data, despite the use of nesting and several assumptions such as: same meteorological parameters all over the lake and the neglect of the horizontal velocity field as

the initial condition after nesting. Because the temperature field was consistently simulated, the two low-frequency internal waves were obtained with similar periods and processes. The simulation was able to reproduce greater deepening of hypolimnetic isotherms compared to metalimnic isotherms. Plus it could reproduce hypolimnetic enhanced shear at the same area as observed data, as well as enhanced turbulence in the hypolimnion. However the time span of this turbulent event appeared to be shorter in the simulation, as well as it occured more frequently likely due to the disparity of energy within the low-frequency internal wave field.

The simulation highlights the dynamics of low-frequency internal waves within the bay with a simulayion. It has been shown that the low-frequency internal wave field does not dissipate completely inside Shiozu Bay. Moreover the simulation shows the main internal Kelvin wave (vertical mode 1 horizontal mode 1) with a rotational pattern, going in and out, inside the bay. This study shows that a sudden change of topography in the hypolimnion, here a contraction in Shiozu Bay, in duo with strong diel wind, may generate modification on the velocity and temperature fields associated with the low-frequency internal wave field below the metalimnion.

Because the energized low-frequency internal waves deepens further in the bay, the effects of the bay's contraction were more intense. These effects generated turbulence through two means. First of all the increased velocity portion generated shear above and below this portion, second of all the interior of such enhanced turbulence event is generated by strain induced by the contraction of the bay.

Chapter 5

Conclusion & Outlook

5.1 Conclusion

This thesis has dealt with the dynamic of propagating low-frequency internal waves within Shiozu Bay, a bay standing at the north of Lake Biwa, as well as dissipative events occuring at the same time scale. In addition, this research aimed to understand whether or not low-frequency can play a direct role in the distribution of energy to small scale processes. The core of this thesis is split in two parts: one dealing with 48 hours long observation data that include microstructure measurement during summer time in Lake Biwa, and the second part dealing with a numerical simulation to mimic observed results.

Observation In the first part of this research, the thesis dealt with observation data in Lake Biwa, Shiga Prefecture, more precisely at the mouth of Shiozu Bay. The first objective was reached using a microstructure profiler (TurboMAP) during 48 hours probing the flow at turbulence scale inside the bay, and ADCPs (Acoustic Doppler Current Profiler) measuring the flow speed and direction at the mouth of the bay during 7 days. By analyzing the current data in the frequency space, as well as the TurboMAP data with a modal analysis, the result showed the presence of a two Kelvin waves, one with a period of 45 hours (being in vertical mode 1 and horizontal mode 1) and 22 hours (being in vertical mode 1 and horizontal mode 2) respectively.

After confirming the presence of low-frequency internal waves within the bay, the first

part of this research highlighted the presence of enhanced turbulence below the metalimnion (ε: 10^{-7} W kg^{-1}) where it is thought to be turbulence-free (10^{-10} W kg^{-1}). Furthermore this turbulent event was linked to enhanced velocity shear, that was correlated with with current associated with the two low frequency internal waves being in phase. Moreover such internal waves synchronization provoked sediment resuspension up to 10 meters above the bottom in enhancing bottom stress. In this section, my research shows a direct role that low-frequency internal waves can play in the redistribution of energy to turbulence and mixing.

Simulation The second objective aimed to ask the question: what is the fate of the low-frequency internal waves within the Shiozu Bay? For this purpose, an analysis of results provided by the numerical simulator SUNTANS (Stanford Unstructured Non-hydrostatic Terrain-following Adaptive Navier-stockes Simulator). Because SUNTANS employs an the unstructured grid, Shiozu Bay was well resolved, matching the shoreline almost perfectly (Shorline resolution: 200 m).

The simulation started during winter when the lake was documented by the Lake Biwa Environment Research Institute as being completely mixed. Then based on weather data provided by JMA stations at 5 stations around the lake, the simulation was able to mimic the generation of internal waves by strong wind stress. The consistency of the simulation was confirmed by comparing simulated data and observed data from different sources. The simulated surface temperature from winter to summer shows the same trend as monitored surface temperature by LBERI. Furthermore temperature and current distributions were compared with the observation carried out in Shiozu Bay, showing a consistent pattern. In addition simulated low frequencies were well resolved in comparison with the observed data. Because of the consistency between simulation and observation the dynamic of low-frequency internal waves within Shiozu Bay is described.

This part of the thesis shows that the low-frequency internal wave field loses energy within the bay through localised enhanced turbulence, but does not dissipate entirely within the bay. Moreover, it appeared that the combination of a sudden change of width and an energized internal wave field generates a great deepening of isotherms and a local increase of the velocity field with enhancement of strain effects, both events enhancing turbulence in the

hypolimnion. The cause of the occurrence of such processes has been identified as hydraulic effect from the walls rather than from the bottom, as it was seen in previous studies. This process is consistent with observed data when the hypolimnetic enhanced shear appeared only when the inertial wave was energized by the wind.

Discussion Under the prospect of understanding the internal wave dynamic in Lake Biwa, data exhibit the occurrence of intense turbulence within the hypolimnion, hypothesized to be generated by velocity shear, but the dimensionless Richardson number was not below the unstability threshold all the time. Therefore it was assumed that isotherms being pulled apart and squeezed played a role in the turbulence generation.

Simulation of Lake Biwa, during the same period than the observation, provided an insight of the mechanisms involved in the turbulence process inside the hypolimnion. These processes occured more often in the simulation because of the energy balance between the two low-frequency internal waves was not well reproduced, hence the wave with higher frequency possessed more energy. Nonetheless, the processes appear to be the same as in the observation. It showed the occurence of shear at the mouth of the bay, as well as turbulence with isotherm being squeezed and pulled apart without shear, quite similar with inferences from observation. Under the assumption that the processes observed and simulated are similar, we can infer that the turbulence event within the hypolimnion is strain generated, linked to the isotherms contraction rather than shear at the TurboMAP location.

Based on the results from observational and simulation, this research has extracted a process that is generated by the interaction of low-frequency internal waves upon a contraction within the hypolimnion. Because we could reproduce the turbulence event with a different low-frequency internal wave field, the process of turbulence generation may not be exceptional but would depend on the energy of the low-frequency internal wave field and the topography. Such event would be linked to low-frequency internal waves because of the need of isotherm elevation as well as current; which are dominated by the low-frequency internal waves. Moreover the fact that southward current, from ADCP at the mouth of the bay, within the hypolimnion has a greater amplitude than the northward current, about twice greater, is consistent with the increase of velocity due to the contraction of the bay.

This thesis shows on certain conditions, related to the energy possessed by the low-frequency internal wave field, hydraulic effect may facilitate the direct reditribution of energy from large scale to turbulence scale. In this study this event occurs within the hypolimnion, where the available potential energy of internal waves is weak, this dissipation would be unnoticed in analysing time series of available potential energy or considered as noise level. The reason why the role of low-frequency internal wave field was observed in MacIntyre *et al.* (2009a) and not in Saggio & Imberger (1998) may be the location of the experiment or the distance to the bottom of isotherm used to compute the available potential energy, in using the same method ($PE = N^2\langle d^2\rangle$, with d the isotherm elevation).

5.2 Outlook

The conclusion made in this research is that dynamics in Shiozu Bay differ from those in the main basin. This doctoral research has underlined the direct role that low-frequency internal waves can play in the redistribution of energy from wind to small-scale and mixing, and their impact on redistribution of biological material such as sediment. Even though the impact may be intermittent (depending on the energy distribution in the low-frequency internal wave field), it appears to be quite intense compared to what was previously thought.

The results of this PhD research emphasizes the impact of bay geometry on the energy redistribution process in the lake. Furthermore the conclusion rises the issue about the direct impact of low-frequency internal wave on biological environment that is not located only at the metalimnion level, but also within the hypolimnion, that may ultimately participate in biomaterial vertical fluxes up to the metalimnion.

Within the simulation section of the thesis, results from simulation show discrepancies with observation. For instance the comparison of horizontal velocity spectra underlines the difference. This discrepancy can be explained by the lack of observed wind field above Lake Biwa. The simulated wind field was issued from an interpolation of land-based meteorological stations scattered throughout Lake Biwa. However, a comparison against observed wind in Lake Biwa was possible with only 48-hr worth of data, leaving the rest of the interpolated wind field not compared with reality. Therefore the mooring of wind sensors on the lake

would have provide a wind fied much closer than reality.

However some aspects of this research remain unexplored. Looking at the campaign data during summer time in Lake Biwa, we observed sediment resuspension likely induced by the low-frequency internal wave field. However what happened to this suspended sediment remains unknown. Because minerals, nutrients and also pollutant compose the sediment layer, understanding the dynamic of this sediment suspension requires more attention (Pomara *et al.*, 2012; Shanmugam, 2013).

The requirement of horizontal resolution to properly simulate non-hydrostasy keeps me from using such a grid in a real Lake Biwa case, the computing time would not be tractable. It would be interesting to assess the impact of nonhydrostasy at the region where the sudden narrowing occurs. Such study could be made in generating another grid including Shiozu Bay only respecting the non-hydrostasy requirement, with an open boundary at the mouth and use coarse grid data as boundary condition.

In the case of Shiozu Bay, the enhanced turbulence event occured within the hypolimnion where the contraction was much more pronounced compared to the shallow part of the bay. However the widts sof the bay close to the surface of deep in the water column are still smaller than the wavelength of the basin scale internal waves. Thus a question arises: what type of topography changes is necessary to generate such enhanced turbulence.

References

AKAIKE, H. (1969). Power spectrum estimation through autoregressive model fitting. *Ann. Inst. Stat. Math.*, 407–419. 36

ALFORD, M. & PINKEL, R. (2000). Observations of overturning in the thermocline: The context of ocean mixing. *American Meteorological Society*, 805–832. 44

ANTENUCCI, J. & IMBERGER, J. (2001). Energetics of long internal gravity waves in large lakes. *Limnol. Oceanogr.*, 1760–1773. 19, 81

APPT, J., IMBERGER, J. & KOBUS, H. (2004). Basin-scale motion in stratified Upper Lake Constance. *Limnol. Oceanogr.*, 919–933. 11, 47

AUGER, G., YAMAZAKI, H., NAGAI, T., JIAO, C. & KUMAGAI, M. (2013). Hypolimnetic turbulence generation associated with superposition of large-scale internal waves in a strongly stratified lake: Lake Biwa, Japan. *Limnology*. 48, 49, 73, 91

BERGH, J. & BERNSTEN, J. (2009). Numerical studies of wind forced internal waves with a nonhydrostatic model. *Ocean Dynamics*, 1025–1041. 51, 74

BERLIAND, M. & BERLIAND, T. (1952). Measurements of the effective radiation of the earth with varying cloud amounts. *Izvestiya Akademii Nauk SSSR, Seriya Geofiz 1*. 58, 60

BOEGMAN, L. (2009). Currents in stratified water bodies 2: Internal waves. In G. Lickens, ed., *Encyclopedia of Inland Waters*, vol. 1, 539–558, Oxford: Elsevier. 5, 6, 7, 13, 86, 96

BOEGMAN, L., IVEY, N. & IMBERGER, J. (2005a). The degenration of internal waves in lakes with sloping boundary. *Limno. oceanogr.*, 1620–1637. 5

BOEGMAN, L., IVEY, N. & IMBERGER, J. (2005b). The energetic of large-scale internal wave degeneration in lakes. *J. Fluid Mech.*, 159–180. 5

CASULLI, V. (1999). A semi-implicit finite difference method for non-hydrostatic, free-surface flows. *Int. J. Numer/ Methods Fluid*, 425–440. 53

COLE, J., PRAIRIE, Y., CARACO, N., MCDOWELL, W., TRANVIK, L., STRIEGL, R., DUARTE, G., KORTELAINEN, P., DOWNING, J., MIDDELBURG, J. & MELACK, J. (2007). Plumbing the global carbon cycle: Integrating inland waters into the terrestrial carbon budget. *Ecosystems*, 172–185. 1

CUMMINS, P., ARMI, L. & VAGLE, S. (2006). Upstream internal hydraulic jumps. *Journal of Physical Oceanography*, 753–769. 97

DE LA FUENTE, A., SHIMIZU, K., IMBERGER, J. & NINO, Y. (2008). The evolution of internal waves in a rotating, stratified, circular basin and the influence of weakly nonlinear and nonhydrostatic accelerations. *Limnol. Oceanogr.*, 27382748. 51, 99

DOROSTKAR, A. (2012). *Three-dimensional dynamics of nonlinear internal waves*. Ph.D. thesis, Queen's University, Kingston, Ontario, Canada. 75, 96, 97, 99, 100

ETEMAD, A. & IMBERGER, J. (1998). Anatomy of turbulence in thermally stratified lakes. *Center for Water Research*, ED–952–AE. 5, 7

FARMER, D. & ARMI, L. (1999). Stratified flow over topography: the role of small-scale entrainment and mixing in flow establishment. *Proc. R. Soc. Lond. A*, 3221–3258. 96

FRINGER, O., GERRITSEN, M. & STREET, R. (2006). An unstructured-grid, finite-volumne, non-hydrostatic, parallel coastal ocean simulator. *Ocean Modelling*, 139–173. ii, 48, 49, 52

GANGOPADHYAY, A., CORNILLON, P. & JACKSON, B. (1989). Autoregressive modeling for the spectral analysis of oceanographic data. *Geophys. Res.*, 16,215–16,226. 35

GILL, A. (1982). *Atmosphere-ocean dynamics*. Academic. 12, 18, 19, 60

GOUDSMIT, G., PEETERS, F., GLOOR, M. & WÜEST, A. (1997). Boundary versus internal dispycnal mixing in stratified natural waters. *J. of Geophysical Reasearch*, 27,903–27,914. 5

HODGES, B., IMBERGER, J., SAGGIO, A. & WINTERS, K. (2000). Modeling basin-scale internal waves in a stratified lake. *Limnol. Oceanogr.*, 16031620. 47, 74

HORN, D., IMBERGER, J. & IVEY, G. (2001). The degeneration of large-scale interfacial gravity waves in lakes. *Journal of Fluid Mechanics*, 181–207. 96

IMBERGER, J. (1998). *Physical Processes in Lakes and Oceans. Coastal and Estuarine Studies*. American Geophysical Union. 3, 8

IVEY, G. (2001). Environmental exchange flows. *Proceedings of the 14th Australasian Fluid Mechanics Conference, Adelaide*, 73–78. 100

IVEY, G. & IMBERGER, J. (1991). On the nature of turbulence in a stratified fluid. part i: The energetics of mixing. *J. Phys. Oceanogr.*, 650–658. 41

JERLOV (1968). *Optical Oceanography*. Elsevier. 61, 62

KANARI, S. (1975). The long-period internal waves in Lake Biwa. *Limno. Oceanogr.*, 544–553. 11, 17

KARYPIS, G. & KUMAR, V. (1996). Parallel multilevel graph partitioning. *Proceedings if IPPS*, 314–319. 48

KAWAMURA, Y., KITADE, Y. & MATSUYAMA, M. (2005). Scattering of semidiurnal internal Kelvin wave at step bottom topography. *Journal of Oceanography*, 59–68. 90

KAY, M. (1988). *Modern Spectral Estimation*. Prentice Hall. 36

KNUTSON, T., MCBRIDE, J., CHAN, J., EMANUEL, K., HOLLAND, G., LANDSCA, C., HELD, I., KOSSIN, J., SRIVASTAVA, A. & SUGI, M. (2010). Tropical cyclones and climate change. *Nature Geoscience*, 157–163. 1

KORTEWEG, D. & DE VRIES G (1895). On the change of form of long waves advancing in a rectangular canal, on a new type of long stationary waves. *Philos. Mag.*, 422–443. 75

LEBLOND, P. & MYSAK, L. (1978). *Waves in the Ocean*. Elsevier Oceanography Series. 90

LEE, H., YAMASHITA, T. & KOMAGUCHI, T. (2008). Reanalysis of past major storms in West Kyusyu and study of wind-induced in Ariake Sea. *Journal of International Development and Co-operation*, 19–36. 79

LEWIS, M., HARRISON, W., OAKEY, N., HEBERT, D. & PLATT, T. (1986). Vertical nitrate fluxes in the oligotrophic ocean. *Science*, 870–873. 4

LORKE, A. (2007). Boundary mixing in the metalimnion of a large lake. *J. Geophys. Res.*, **112**, doi:10.1029/2006JC004008. 3, 5, 7

LORKE, A., UMLAUF, L., JONAS, T. & WÜEST, A. (2002). Dynamics of turbulence on low-speed oscillating bottom boundary layers of stratified basins. *Environ. Fluid Mech.*, 291–313. 6

MACINTYRE, S. & JELLISON, R. (2001). Nutrient fluxes from upwelling and enhanced turbulence at the top of the pycnocline in Mono Lake, California. *Hydrobiologia*, 13–29. 4

MACINTYRE, S., FLYNN, K., JELLISON, R. & ROMERO, J. (1999). Boundary mixing and nutrient fluxes in Mono Lake, California. *Limnol. Oceanogr.*, 512–529. 2

MACINTYRE, S., CLARK, F., JELLISON, R. & FRAM, P. (2009a). Turbulent mixing induced by nonlinear internal waves in Mono Lake, California. *Limnol. Oceanogr.*, 2255–2272. 3, 7, 40, 44, 48, 106

MACINTYRE, S., FRAM, J., KUSHNER, P., BETTEZ, N., O'BRIEN, W., HOBBIE, J. & KLING, G. (2009b). Climite-related variations in mixing dynamics in an Alaskan artic lake. *Limnol. Oceanogr.*, 2401–2417. 7, 40

MADERICH, V., BROVCHENKO, I., TERLETSKA, K. & HUTTER, K. (2012). Numerical simulations of the nonhydrostatic transformation of basin-scale internal gravity waves and wave-enhanced meromixis in lakes. In K. Hutter, ed., *Nonlinear Internal Waves in Lakes*, vol. 1, 193–272, Springer. 97

MARSHALL, J., ADCROFT, A., HILL, C., PERELMAN, L. & HEISEY, C. (1997a). A finite-volume, incompressible navier stokes model for studies of the ocean on parallel computers. *J. Geophys. Res.*, 57535766. 53

MARSHALL, J., HILL, C., PERELMAN, L. & ADCROFT, A. (1997b). Hydrostatic, quasi-hydrostatic, and nonhydrostatic ocean modeling. *Journal of Geophysical Research*, 5733–5752. 76, 77

MELLOR, G. & YAMADA, T. (1982). Development of a turbulence closure model for geophysical fluid problems. *Reviews of Geophysics and Space Physics*, 851–875. 53, 85

MONISMITH, S., IMBERGER, J. & MORISON, L. (1990). Convective motions in the sidearm of a small reservoir. *Limnol. Oceanogr.*, 1676–1702. 1

MUNK, W. (1966). Abyssal recipies. *Deep-Sea Res.*, 707–730. 3

MUNK, W. & WUNSCH, C. (1998). Abyssal recipies ii: Energetics of tidal and wind mixing. *Deep-Sea Res.*, 1977–2010. 3

MÜNNICH, M., WÜEST, A. & IMBODEN, M. (1992). Observations of the second vertical mode of seiche in an alpine lake. *Limnol. Oceanogr.*, 1705–1719. 5, 15, 33, 40, 42

OAKEY, N. (1982). Determination of the rate of dissipation of turbulent energy from simultaneous temperature and velocity shear microstructure measurements. *Phys. Oceanogr.*, 256–271. 29

OKAMOTO, I. & ENDOH, S. (1995). Water mass exchange between the main basin and shiozu bay. In M.K. S. Okuda J. Imberger, ed., *Physical Processes in a Large Lake, Japan. Coastal and Estuarine Studies*, vol. 48, 31–42, American Geophysical Union. 21, 38, 48

OKELY, P. & IMBERGER, J. (2007). Horizontal transport induced by upwelling in a canyon-shaped reservoir. *Hydrobiologia*, 343–355. 1

OSBORN, T. (1980). Estimates of the local rate of vertical diffusion from dissipation measurements. *J. Phys. Oceanogr.*, 83–89. 41

PAIN, C., PIGGOTT, M., GODDARG, A., FANG, F., GORMAN, G., MARSHALL, D., EATON, M., POWER, P. & DE OLIVEIRA, C. (2005). Three-dimensional unstructured mesh ocean modeling. *Ocean Modell.*, 5–33. 49

POMARA, L., MORSILLIB, M., HALLOCKC, P. & BÁDENAS, B. (2012). Internal waves, an under-explored source of turbulence events in the sedimentary record. *Earth-Science Reviews*, 56–81. 107

PRATT, L. (1986). Hydraulic control of sill flow with bottom friction. *Journal of Physical Oceanography*, 1970–1980. 100

SAGGIO, A. & IMBERGER, J. (1998). Internal wave weather in stratified lake. *Limnol. Oceanogr.*, 1780–1795. i, 2, 3, 4, 7, 8, 20, 26, 38, 39, 106

SAKAI, T. & REDEKOPP, L. (2010). A parametric study of the generation and degeneration of wind-forced long internal waves in narrow lakes. *J of Fluid Mechanics*, **645**, 315–344. 71, 96

SAKAI, Y., MURASE, J., SUGIMOTO, A., OKUBO, K. & NAKAYAMA, E. (2002). Resuspension of bottom sediment by an internal wave in lake biwa. *Lakes & Reservoirs: Research & Management*, 339–344. 33, 45

SANNINO, G., PRATT, L. & CARILLO, A. (2009). Hydraulic criticality of the exchange flow through the Strait of Gibraltar. *American Meteorological Society*, 2779–2799. 97, 99

SHANMUGAM, G. (2013). Comment on internal waves, an under-explored source of turbulence events in the sedimentary record by l. pomar, m. morsilli, p. hallock, and b. bádenas [earth-science reviews, 111 (2012), 5681]. *Earth-Science Reviews*, 195–205. 107

SHIMIZU, K. & IMBERGER, J. (2008). Energetics and damping of basin-scale internal waves in a strongly stratified lake. *Limnol. Oceanogr.*, 1574–1588. 5

SHIMIZU, K. & IMBERGER, J. (2010). Seasonal differences in the evolution of damped basin-scale internal waves in a shallow stratified lake. *Limnol. Oceanogr.*, 1449–1462. 11

SHIMIZU, K., IMBERGER, J. & KUMAGAI, M. (2007). Horizontal structure and excitation of primary motions in a strongly stratified lake. *Limnol. Oceanogr.*, 2641–2655. 20, 39, 47, 64, 72, 73, 81

SONG, Y. & HAIDVOGEL, D. (1994). A semi-implicit ocean circulation model using a generalized topography-following coordinate system. *Journal of Computational Physics*, 228–244. 52

STACEY, M., MONISMITH, S. & BURAU, J. (1999). Observations of turbulence in a partially stratified estuary. *Journal of Physical Oceanography*, 1950–1970. 91

THORPE, S. (2005). *The turbulent ocean*. Cambridge University Press. 96

UMLAUF, L. & LEMMIN, U. (2005). Interbasin exchange and mixing in the hypolimnion of a large lake: The role of long internal waves. *Limnol. Oceanogr.*, 1601–1611. 48, 100

VITOUSEK, S. & FRINGER, O. (2011). Physical vs. numerical dispersion in nonhydrostatic ocean modeling. *Ocean Modeling*, 72–86. 75, 99

WOLK, F., YAMAZAKI, H., SEURONT, L. & LUECK, R. (2002). A new free-fall profiler for measuring biophysical microstructure. *Atmos.Oceanic Technol.*, 780–793. 22

WÜEST, A. & LORKE, A. (2003). Small-scale hydrodynamics in lakes. *Annu. Rev. Fluid Mech.*, 373–412. 3, 5, 6, 45, 100

WÜEST, A. & LORKE, A. (2005). Validation of microstructure-based diffusivity estimates using tracers in lakes and oceans. In H. Baumert, J. Simpson & J. Sundermann, eds., *Marine Turbulence: Theories, Observations and Models.*, 139–152, UK: Cambridge Univ. Press. 41

WÜEST, A., SENDEN, C.V., IMBERGER, J., PIEPKE, G. & GLOOR, M. (1996). Comparison of diapycnal diffusivity by tracer and microstructure techniques. *Dyn. Atmos. Oceans*, 27–39. 2

WÜEST, A., PIEPKE, G. & SENDEN, C.V. (2000). Turbulence kinetic energy balance as a tool for estimating vertical diffusivity in wind-forced stratified waters. *Limnol. Oceanogr.*, 1388–1440. 5

YAMAZAKI, H., HONMA, H., NAGAI, T., DOUBELL, M., AMAKASU, K. & KUMAGAI, M. (2010). Multilayer biological structure and mixing in the upper water column of Lake Biwa during summer 2008. *Limnology*, 63–70. 4

ZANEVELD, J., KITCHEN, J. & PAK, H. (1981). The influence of optical water type on the heatinf rate of a constant depth mixed layer. *J of Geophys. Res.*, 6426–6428. 61, 62

ZHANG, Z., FRINGER, O. & RAMP, S. (2011). Three-dimensional, nonhydrostatic numerical simulation of nonlinear internal wave generation and propagation in the South China Sea. *J. Geophys. Res.*, **116**, C05022. 48